THESIS

ANALYSIS OF THE DIURNAL CYCLE IN TAIWAN DURING THE TERRAIN-INFLUENCED MONSOON RAINFALL EXPERIMENT

Submitted by

James Howard Ruppert, Jr.

Department of Atmospheric Science

In partial fulfillment of the requirements

For the Degree of Master of Science

Colorado State University

Fort Collins, Colorado

Spring 2012

Master's Committee:

Advisor: Richard H. Johnson

V. Chandrasekar
Steven J. Fletcher
Eric D. Maloney

ABSTRACT

ANALYSIS OF THE DIURNAL CYCLE IN TAIWAN DURING THE TERRAIN-INFLUENCED MONSOON RAINFALL EXPERIMENT

The diurnal cycle is investigated in Taiwan during the summer monsoon ("Mei-yu" or plum rain) season using enhanced observations from the 2008 Terrain-influenced Monsoon Rainfall Experiment (TiMREX). The diurnal cycle of an undisturbed period is compared with that of a disturbed period in an aim to 1) better understand the variability of the diurnal cycle as a function of large-scale forcing, 2) describe the complex relationships between rainfall and orographically modified flow, and 3) determine the governing environmental characteristics that distinguish disturbed and undisturbed periods. The study is performed using a regional reanalysis generated by employing three-dimensional variational data assimilation techniques, 0.5° 6-h forecasts from the NCEP GFS (National Centers for Environmental Prediction Global Forecast System), and multiple observation platforms (from TiMREX datasets and others).

The undisturbed period (UNDIST) was characterized by southwesterly monsoon flow at low levels, zonal flow in the upper troposphere, suppressed daily-mean rainfall, and unimpeded insolation. Accordingly, pronounced diurnal land–sea breeze (LSB) and mountain–valley (MV) circulations strongly controlled rainfall patterns, which exhibited patterns consistent with low-Froude-number (Fr) flow diverting around the mountainous island of Taiwan. Maximum daytime onshore/upslope flows were associated with enhanced rainfall along the coastal plains and foothills of Taiwan (as opposed to the high

peaks), until the nighttime transition brought offshore/downslope flows and development of offshore rainfall where nocturnal density currents converged with the impinging southwesterly monsoon flow.

During the disturbed period (DIST), the positioning of a prominent upper-tropospheric trough put Taiwan in a favorable area for large-scale ascent and convective organization, while a shallow, northerly cold intrusion (the Mei-yu front) provided a low-level triggering mechanism for vigorous deep convection. Although the amplitude of diurnal LSB/MV circulations was suppressed during this period (in association with reduced insolation), rainfall diurnal variability was noteworthy, suggesting heightened sensitivity of rainfall to diurnal flows. Consistent with moist conditions and higher-Fr flow, rainfall during this period was maximized over the high mountain peaks.

Analysis of vertical profiles of vertical motion and apparent heat sources and moisture sinks for UNDIST demonstrates a predominance of shallow vertical circulations and bottom-heavy convection. In contrast, vigorous deep convection was the dominant rainfall mode during DIST. That the environment was more conducive for vigorous deep convection during DIST explains the increased sensitivity of rainfall to diurnal flows.

Common to both periods was an afternoon transition from shallow to deep convection to stratiform rainfall (heating above the freezing level and cooling below; consistent with previous studies). The evolution of rainfall prior to, during, and following DIST exhibited a similar transition. This reflects the “self-similar” nature of tropical convective rainfall systems across spatial and temporal scales.

ACKNOWLEDGEMENTS

First and foremost, I thank my advisor, Dr. Richard H. Johnson, for his unwavering support and enthusiasm in both the work culminating in my Master's thesis as well as my scientific education in general. His enthusiasm has made my pursuit of a Master's degree as well as my overall experience at Colorado State University (CSU) remarkably fulfilling. I thank my MS committee members, Drs. V. Chandrasekar, Steven J. Fletcher, and Eric D. Maloney, for their constructive comments on and critique of this work.

I am indebted to Dr. Lance F. Bosart of the University at Albany, who since my days in undergraduate study has provided me endless mentoring advice, without which I would have surely lost my way. I thank many staff and students of the CSU Johnson Research Group, both past and present, for their valuable support, comments, and advice – Paul Ciesielski, Rick Taft, Brian McNoldy, Mike Toy, Andy Newman, Zack Finch, and Gail Cordova. I thank the many helpful administrative staff of the CSU Department of Atmospheric Science, who have assisted me in numerous ways since I arrived at CSU. I thank John Forsyth of CSU for his helpful comments. I acknowledge the helpful advice of several staff from the National Center for Atmospheric Research – Jenny Sun, Hongli Wang, and Xin Zhang.

Last but certainly not least, I wholeheartedly thank all of my friends and family, many of which I have only known since arriving at CSU in 2009. They have shown me that my success in life rests as much on their camaraderie and support as on my own academic and professional performance.

TABLE OF CONTENTS

1. INTRODUCTION

The tropical and subtropical Asian monsoon region has historically been a fervent target area of study in atmospheric science. This has largely been driven by a need for improved atmospheric predictions in an area of the globe that serves as home to the majority of the world's population. Comprehensive understanding and accurate prediction of monsoon rainfall variability, from diurnal through interannual timescales, are essential for global-societal concerns such as agriculture, water basin control, and flood and drought preparedness.

The analysis of Trenberth et al. (2000) demonstrates that the global divergent circulation is dominated by the seasonally varying global monsoon system, explaining 60% of the total variance. Thus, understanding the global monsoon system and its regional constituents is inherent in description of Earth's atmospheric general circulation, which is responsible for the majority of the poleward transport of energy received from the sun (Oort and Vonder Haar 1976; Trenberth and Caron 2001). Furthermore, since annual rainfall variability in the tropics is dominated by the global monsoon system (Wang and Ding 2008), understanding this major component of the hydrologic cycle involves understanding the local and mesoscale convective processes that, in their cumulative effect, comprise the monsoon.

The important role of diurnal variability in exerting a strong control on the timing of precipitation, particularly moist convection, has been recognized for some time (Wallace 1975; Gray and Jacobson 1977; Dai 2001; Johnson 2011). Yet many details concerning particular aspects of diurnal variability, such as nocturnal rainfall maxima

over open oceans (e.g., Mapes and Houze 1993; Nesbitt and Zipser 2003), subseasonal variability in the diurnal cycle of monsoon convection (as in China; Yu et al. 2007; Chen et al. 2009), and substantial surface diurnal flow anomalies over open oceans (e.g., Dai and Deser 1999), have continued to elude full understanding. Much of the difficulty in studying such aspects of the diurnal cycle relates to a lack of observations over many parts of the world. Thus, many field campaigns have been conducted in recent decades in an effort to fill such gaps in understanding and learn more about, e.g., the relationships between diurnal variability, mesoscale patterns of precipitation, and the broader monsoon system.

1.1 The Asian monsoon

The Tibetan Plateau, with an average elevation exceeding 4.5 km, exerts a major control on the seasonal cycle and general climate in Asia and the surrounding regions. Sensible heating of its elevated surface and diabatic heating from convection cause a positive local buoyancy anomaly throughout the warm season, which is conducive for large-scale ascent locally and sinking motion remotely (largely accounting for the surrounding desert/arid climates; He et al. 1987; Yanai et al. 1992; Rodwell and Hoskins 1996). With northward migration of peak shortwave heating in late spring, the northward-migrating eastern-hemispheric monsoon rainbelt works in concert with intensifying heating on/over the Tibetan Plateau to cause a planetary-scale circulation change and associated intensification of rainfall throughout a significant portion of Asia (He et al. 1987; Yanai et al. 1992). The large-scale circulation changes surrounding onset of the

Asian monsoon, which to a large degree occurs in distinct steps, can be summarized as follows (He et al. 1987; Yanai et al. 1992):

1. Mid-May – the northward-migrating monsoon rainbelt couples with the ascending branch of the vertical circulation associated with Tibetan Plateau heating; associated with this coupling, dramatically enhanced heating (from convection and vertical/horizontal advection) extending from the eastern Plateau to the South China Plain causes northward propagation of the South Asian 200-hPa anticyclone, reversal of the mid–upper-tropospheric meridional temperature gradient over Southeast Asia, and onset of the moist lower-tropospheric (e.g., 850-hPa) Southeast Asian southwesterly flow; in association with the latter is the commencement of heavy Southeast Asian monsoon rainfall.
2. Mid-June – as the primary monsoon rainbelt progresses northward in East Asia, intense heating commences over the western Plateau and westward as a result of adiabatic sinking and warming in the descending branch of the amplifying large-scale coupled monsoon–Plateau vertical circulation; accordingly, the 200-hPa anticyclone builds westward, the meridional temperature gradient reverses west of the Plateau, moist southwesterly flow is established in the Arabian Sea, and heavy monsoon rainfall commences in western India.

Figure 1.1, taken from Johnson 1992 (his Fig. 1b), provides a broad overview of the Asian summer monsoon circulation and rainfall pattern, roughly corresponding to June–September. Note the continuous lower-tropospheric flow connecting from the

southern-hemispheric southeasterly trades, via southerly cross-equatorial flow, to the broad region of west-southwesterly flow spanning the northern Indian Ocean, Bay of Bengal, Arabian Sea, and much of the southern Asian landmass. Heavy rainfall is present in southwestern India, the southern Plateau region, and the Indochina Peninsula. Though omitted from Fig. 1.1, heavy rainfall is also extensive in most of Southeast and East Asia during this period (e.g., Lau et al. 1988).

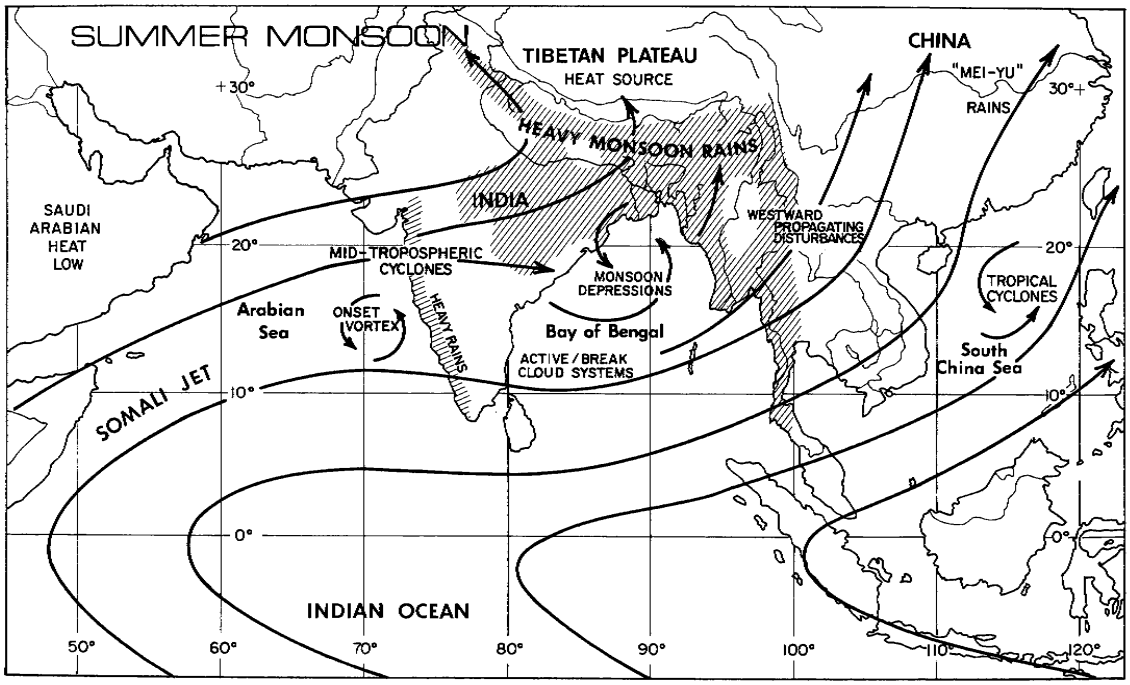

Fig. 1.1. Schematic of lower-tropospheric circulation and rainfall characteristics of the Asian summer monsoon (from Johnson 1992; their Fig. 1b). The hatching denotes areas of rainfall exceeding 100 cm during the June–September period. Areas of rainfall over water and east of 100°E are omitted (note that heavy rainfall is also present throughout Southeast and East Asia during this period; Lau et al. 1988). The Mei-yu region of East China is indicated near the Yangtze River valley, though the Mei-yu region studied here corresponds to that of the northern South China Sea (SCS), southern China, and Taiwan.

Superimposed on the general circulation and rainfall patterns of the Asian summer monsoon pattern discussed above is a prominent diurnal cycle. Mesoscale features such as land–sea contrast and topographic gradients cause myriad complex local diurnal patterns in circulation and rainfall throughout the Asian monsoon basin, though

there is an important diurnal variation of the large-scale monsoonal system. Yanai et al. (1992) describe the diurnal cycle in a very deep, well-mixed boundary layer over the Plateau, which maximizes in the evening hours (coincident with maximum daytime heating). This diurnal cycle in heating over the Plateau drives a continental scale diurnal cycle in divergent circulation (Krishnamurti and Kishtawal 2000).

1.2 The Mei-yu season

Though "Mei-yu" (plum rain) is the nomenclature used for the heavy monsoon rainfall period of East China (e.g., in the Yangtze River valley; Fig. 1.1), the Mei-yu season studied here corresponds to the mid-May–mid-June heavy rainfall period in the northern South China Sea (SCS), southern China, and Taiwan (termed the "pre-summer" rainy period by Chinese meteorologists, and Mei-yu by Taiwanese). The start of the Mei-yu in Southeast Asia represents one of the early onset stages of the broader East Asian summer monsoon and, broader yet, marks the rapid-intensification stage of the entire Asian summer monsoon system (Ding and Chan 2005). Ding and Chan (2005) provide a large-scale overview of this onset period based on a 21-yr climatology generated from global reanalysis data. A synopsis of the sequence of events is as follows (Ding and Chan 2005): weak low-level southwesterly flow is first observed in the eastern Indian Ocean with convection present in the southern Indochina Peninsula and offshore (early–mid-May); around mid-May, marked cross-equatorial moisture transports are rapidly established via the Somali jet in the western Indian Ocean (noted in Fig. 1.1) and another stream just west of the Maritime Continent; low-level westerly flow develops across the

northern Indian Ocean as the southwesterlies extend eastward across the Indochina Peninsula, such that a moisture connection is established between the southern hemisphere, Indian Ocean, and the SCS; this marks the start of summer monsoon rainfall (Mei-yu) for Southeast Asia.

i). Subseasonal variability and monsoon onset

It has been shown that the abrupt circulation changes marking the onset of the Mei-yu season and rapid intensification of the Asian monsoon are connected with subseasonal periodic tropical modes of variability (Chen and Chen 1995; Wang and Xu 1997; Chan et al. 2002; Johnson and Ciesielski 2002; Mao and Chan 2005; Hung and Hsu 2008; Tong et al. 2009; Chen and Sui 2010). Wang and Xu (1997) demonstrate the presence of an annually recurring northward-propagating intraseasonal oscillation (with spectral peaks from 30–60 days) in the Asian monsoon region that is characterized by a first-baroclinic-mode structure (i.e., enhanced convection connected with low-level convergence and upper-level divergence). Wang and Xu (1997) show that this mode, which they denote the climatological intraseasonal oscillation (CISO), exhibits phase locking between the annual cycle (defined as the "smooth base annual cycle" with periods >90 days) and the transient, eastward-propagating Madden–Julian oscillation (MJO; Madden and Julian 1971). Similarly, Hung and Hsu (2008) show that during years when abrupt onset of the Asian monsoon is observed (as defined by a singular sign reversal in the first principal component of 850-hPa flow in the Asian monsoon basin), there is a marked connection between the MJO propagating eastward across the Indian

Ocean and rapid enhancement of the northern Indian Ocean westerlies, northeastward extension of the southwesterly flow across the Indochina Peninsula and into the SCS, and enhanced moisture convergence in the SCS.

Mao and Chan (2005) analyze ~30 yrs of reanalysis data to describe dominant composite modes of intraseasonal wave activity connected with the SCS monsoon, which exhibits peaks in spectral power at 10–20 and 30–60 days. They discuss a composite 30–60-day monsoon mode (hereafter, the 3060-MM) characterized by a northward-propagating trough–ridge seesaw pattern in which the monsoon trough (i.e., the cyclonic shear side of enhanced southwesterly flow) and West Pacific subtropical ridge exist alternatively over the SCS, with anomalous cyclonic (anticyclonic) flow within the trough (ridge) coinciding with enhanced (suppressed) convection. In terms of vertical structure and associated coupling with monsoon activity, this northward-propagating mode closely resembles the CISO that Wang and Xu (1997) and Hung and Hsu (2008) connect with MJO activity. According to Tong et al. (2009), a stationary 40-day heating centered over the equator results in poleward emanation of Rossby gyres (as the heating dissipates) that modify the meridional height gradient in the SCS region and, as a result, cause an alternation of the monsoonal southwesterly flow. The implication of this study is that diabatic heating associated with the MJO, or any other convectively coupled equatorial wave, might be sufficient to spawn the northward propagating 3060-MM.

Mao and Chan (2005) also describe a composite 10–20-day monsoon mode (1020-MM), which is characterized by a low-level westward-propagating cyclone–anticyclone system with upper-level divergence (convergence) coupled to the low-level cyclone (anticyclone). They note that this “biweekly” mode, which has components

originating in both the tropical West Pacific and midlatitudes, resembles a mixed Rossby–gravity wave train. Chen and Sui (2010) demonstrate that diabatic heating in the western tropical Pacific can generate a northwestward-propagating Rossby wave train, and further note that in the presence of westerly flow extending deep into the tropics (e.g., along the northern periphery of the West Pacific subtropical high), a "wave duct" (Webster and Holton 1982) permits Rossby wave trains to propagate southward from midlatitudes. Johnson and Ciesielski (2002) describe the passage of a prominent mixed Rossby–gravity wave over the Maritime Continent during the onset of the 1998 summer monsoon in the SCS, which originated from the east. Johnson and Ciesielski further note the presence of a westerly duct as this mode passed, which opens the possibility that the wave was forced either from the deep tropics or from midlatitudes (e.g., features connected to the subtropical westerly jet). In fact, in their composite analysis of 30–60-day variability in 850-hPa height over the SCS, Tong et al. (2009) note that, aside from poleward-propagating Rossby wave trains from the equatorial region, there is clear equatorward propagation of features. Though they are not able to rectify the latter using their idealized simulations, these northward-originating features add to the possible origins of the 3060-MM.

The studies discussed above demonstrate the importance of subseasonal variability – namely, the 1020-MM and 3060-MM – in the initial onset of moist southwesterly flow and convection in Southeast Asia (Wang and Xu 1997; Johnson and Ciesielski 2002; Mao and Chan 2005; Hung and Hsu 2008). Though there is an apparent tendency for the CISO and associated rapid ramp up of the Asian monsoon to occur at a similar time each year (Wang and Xu 1997; Hung and Hsu 2008), it is not obvious

whether or not one of these mode has a dominant part to play in the process of monsoon onset. The study of Mao and Chan (2005) demonstrates that the relative roles of the 1020-MM and 3060-MM vary from year to year in the SCS monsoon region (in terms of variance explained), so it is plausible that relative roles of the different wave modes in onset processes also vary from year to year. Studies have also shown connection of the above wave modes to the circulation changes observed during transitions between active and break periods in monsoon convection, which are notoriously difficult to predict (Krishnamurti and Ardanuy 1980; Chen and Chen 1995; Chan et al. 2002). Difficulties in understanding and predicting these features relates to a lack of understanding in their generation (which evidently occurs both in the deep tropics and in midlatitudes) and fundamental dynamics.

ii). Mesoscale overview of the Mei-yu season

Onset of the Mei-yu season occurs when the flow pattern exhibits a large-scale adjustment, such that a channel of moisture is established across the northern Indian Ocean, the Indochina Peninsula, and the SCS that results in an environment more conducive for moist convection (e.g., Ding and Chan 2005). Still, the convective activity and character during a given Mei-yu season fluctuates markedly. Studies have demonstrated a connection of these fluctuations with subseasonal modes such as the 1020-MM and 3060-MM, which evidently have both tropical and subtropical origins (e.g., Krishnamurti and Ardanuy 1980; Chen and Chen 1995; Chan et al. 2002; Johnson and Ciesielski 2002; Mao and Chan 2005). These modes are connected with anomalous

patterns in lower- and upper-tropospheric divergence and vorticity, and thus, at the most basic level, are important for controlling the southwesterly stream of moisture and instability that seeds convection in the Mei-yu region (e.g., Mao and Chan 2005).

Johnson and Bresch (1991) describe the evolution of rainfall systems during the 1987 Mei-yu season in Taiwan based on special observations from the May–June 1987 Taiwan Area Mesoscale Experiment (TAMEX). They note that there are periods during the season in which the environment was conditionally unstable and deep convection predominated, while other periods were characterized by surface northerly cold intrusions, stable conditions, and more stratiform- and shallow-type precipitation regimes (consistent with frontal overrunning and/or stable orographic lifting). Such cold intrusions are manifestation of the southward movement of the marked boundary between the northeasterly wintertime flow regime to the north and southwesterly summer monsoon flow to the south (the "Mei-yu front;" Chen 2004). The roughly east–west-oriented Mei-yu front in the northern SCS region is described as a semitropical, equivalent-barotropic warm-core feature, as it is often characterized by a quasi-stationary zone of enhanced convergence and cyclonic vorticity with weak thermal contrast (Chen 2004). It is the southwestward extension of a cold-core baroclinic frontal system (i.e., tilted westward with height) in Japan (the "Baiu front"), which is more in line with the character of the Mei-yu front situated over the Yangtze River valley later in the East Asian summer monsoon season (Fig. 1.1; Chen 2004).

The Mei-yu fronts play a major role in rainfall during the Mei-yu season (e.g., Johnson and Bresch 1991), as mesoscale convective systems (MCSs) routinely spawn, amplify, and propagate downstream along and just south of the frontal convergence line

and result in copious rainfall rates and totals in Taiwan (Chen 2004). There is a frequent amplification observed in the local Mei-yu circulation system – e.g., coincident strengthening of the Mei-yu front with enhancement of convection, moisture flux convergence, cyclonic vorticity, and low-level southwesterly flow in the form of a low-level jet (e.g., at 850 hPa). A barotropic-type feedback process has been attributed to this systematic amplification in several cases (e.g., Chen et al. 2008; Lai et al. 2011). Chen et al. (2008) describe an intense case (6–7 June 2003) in which the different components of this feedback process were particularly robust: a train of mesoscale vortices developed along the Mei-yu frontal vorticity band in the presence of barotropic instability, which subsequently developed into large MCSs; convective heating and associated mesoscale ascent enhanced frontal vorticity though stretching and developed an ageostrophic, thermally-direct transverse circulation south of the front; geostrophic adjustment of the lower-branch of this circulation generated an intense (i.e., >22.5-m s^{-1}) 850-hPa southwesterly low-level jet (which might have then supplied more moisture to the convection; Lai et al. 2011).

Though the shallow Mei-yu front often exhibits density current-like structure (Trier et al. 1990) and is often maintained by barotropic-convective feedbacks once situated over the northern SCS region (Chen et al. 2008; Lai et al. 2011), the study by Chen (1993) suggests that Mei-yu fronts can exhibit tilted baroclinic structure, particularly during the early stages of their development over mainland China. Observed connections of the Mei-yu front with a southward-advancing upper-level trough and low-level jet with a balanced geopotential height field (Chen 1993) suggest that the Mei-yu fronts are (at least in early stages) maintained by baroclinic processes. It is plausible that

southward advancement of the Mei-yu front is initiated by subtropical baroclinic processes, until sensible heating from the warm water surface weakens the thermal contrast and density current- and tropical barotropic-type maintenance processes take over farther south (Trier et al. 1990).

An important factor in the distribution of Mei-yu seasonal rainfall in Taiwan is related to the effects of orography on the flow dynamics. Figure 1.2, a topographic map of Taiwan, reveals the steep terrain on the island, with the coastal plains separating the west coast from the steepest slopes of the Central Mountain Range (CMR). Classical theory demonstrates that the key parameter determining whether a barrier is hydrodynamically steep, such that it will strongly modify the flow, is the Burger number $B = (h/L)(N/f)$, where h is the characteristic mountain height, L the flow-parallel mountain half-width, N the static stability, and f the Coriolis parameter (Overland and Bond 1995).

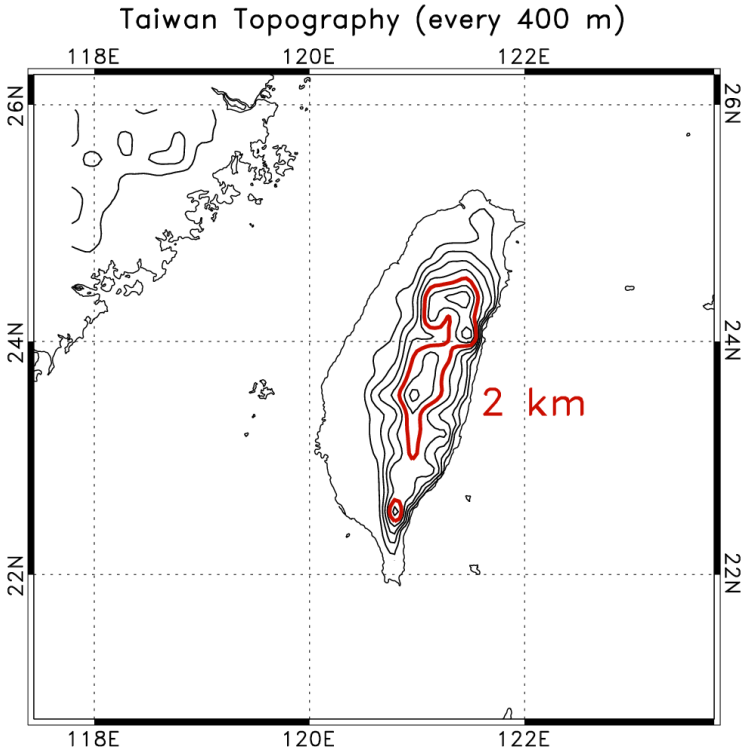

Fig. 1.2. Map of the topography in Taiwan (contours every 400 m). The 2-km level is indicated.

B represents the effective "steepness" of the barrier, such that when $B << 1$, the slope is mild and the flow remains in quasi-geostrophic balance, and for $B >> 1$, the slope is significant and ageostrophic flows divert around the barrier (Pierrehumbert and Wyman 1985; Smolarkiewicz et al. 1988; Overland and Bond 1995). For Taiwan, $h \sim 2$ km, $L \sim 50$ km, $N \sim 10^{-2}$ s^{-1}, and $f \sim 10^{-4}$ s^{-1}, resulting in $B \sim 4$; this suggests that the CMR of Taiwan presents a steep barrier to the flow (Li and Chen 1998). In this case, the Froude number (Fr = U/Nh), whose square represents a ratio of the kinetic energy of the ambient flow to the potential energy required to cross the barrier, can be used to assess the characteristics of flow blocking by the steep barrier (Pierrehumbert and Wyman 1985). For $U \sim 10$ m s^{-1} (and assuming the other scales from above), Fr ~ 0.5, suggesting that the kinetic energy of the flow is small relative to the potential energy needed to cross the barrier, and thus, that the flow will be blocked and divert around the barrier (e.g., Smolarkiewicz et al. 1988; Li and Chen 1998).

Studies from TAMEX demonstrate that, consistent with low-Fr flow and the steep barrier of the CMR, there is a frequent occurrence of lower-tropospheric orographically induced barrier jets under the southwesterly monsoon flow (Li and Chen 1998). Li and Chen (1998) and Yeh and Chen (2003) demonstrate that these barrier jets, which are characterized by locally enhanced ~southerly flow over the northwestern coastal plains, result from parcel acceleration down a pressure gradient associated with an orographically generated pressure couplet across the CMR (high pressure along the upwind slope and low pressure along the leeward slope). Fundamentally, this pressure couplet can be understood as a surplus of mass on the upwind side of the barrier and a mass deficit downwind (Smolarkiewicz et al. 1988; Carbone et al. 1995). It can

alternatively be understood from theory as forced adiabatic cooling (and hydrostatic compression) along the upwind slope, where the momentum of the ambient flow drives stable parcels upwards against gravity, and adiabatic warming (and hydrostatic decompression) along the leeward slope where air descends to fill the mass deficit (Epifanio and Rotunno 2005).

The approach described above for diagnosing the characteristics of flow blocking (via *B* and Fr) is not without limit. As demonstrated by Yeh and Chen (2003), the magnitude of the cross-CMR pressure couplet and resulting southerly barrier jet are proportional to the flow speed. This is consistent with higher momentum causing greater ascent and adiabatic cooling upwind and a greater mass deficit downwind (and associated sinking and adiabatic warming). An increase in *U* results in an increase in Fr, which suggests weaker blocking. Weaker blocking is evident in one sense: with increased *U*, the higher increased momentum enables the flow to traverse the barrier rather than divert around it. On the other hand, the observed increase in cross-CMR pressure couplet and associated barrier jet (i.e., split flow pattern) is indicative of enhanced blocking. This paradox in Fr stems from applying a two-dimensional concept to a three-dimensional problem (e.g., Pierrehumbert and Wyman 1985). Further, there are complications excluded from the above diagnosis that come with the effects of latent heating. Yeh and Chen (2003) analyze the impacts on the Taiwan barrier jet after turning off latent processes. The simulation without latent heating shows a stronger pressure couplet and associated barrier jet, suggesting that effect of the latent heating is to reduce adiabatic temperature changes associated with the orographically forced ascent [either by reducing vertical perturbations from the topography or by reducing *N*; consistent with Chen and

Feng (2001)]. Finally, studies have demonstrated the complicating effects of diabatic cooling-enhanced density currents, which can enhance convergence along the slopes of terrain and generate upstream- and downstream-propagating density currents with attendant convection at the leading edge (Carbone et al. 1995; Chen and Lin 2005; Asencio and Stein 2006; Miglietta and Rotunno 2009).

iii). The diurnal cycle during the Mei-yu season

It is impossible to fully understand the Mei-yu season in Taiwan and the surrounding area without considering local diurnal variability. Under strong daytime solar insolation in summer, the low-heat-capacity land surface of Taiwan heats as the thermally sluggish surface of the adjacent seas remains cool, thus causing a landward-directed horizontal buoyancy gradient that eventually generates a landward-propagating density current with attendant thermally-direct vertical circulation (sea breeze; e.g., Rotunno 1983). Likewise, the strongly sloped terrain of the CMR generates strong horizontal buoyancy gradients through a large depth as the sloped land surface heats up and adjacent air remains relatively cool, causing development of a positively buoyant upslope flow (anabatic wind; e.g., Orville 1964). The opposite patterns occur at night: the land surface cools, generating an offshore-propagating density current (land breeze), and the sloped surface of the CMR cools, causing a negatively buoyant downslope (katabatic) flow. The resulting diurnal cycle in rainfall can be summarized as follows (Johnson and Bresch 1991): as the daytime land–sea breeze (LSB) and anabatic–katabatic (or mountain–valley; MV) circulations spin up in the late morning/early afternoon hours,

increased rainfall develops along the coastal plains and foothills in the form of deep convection (maximizing in the early afternoon); convection evolves into stratiform rain (with heating aloft and cooling below), as likely evaporation-enhanced downslope flows develop coincident with nighttime surface cooling; offshore rainfall maximizes during the overnight/early morning hours, which is coincident with offshore-propagating density currents associated with the LSB/MV circulations.

A major consequence of the geographical layout of Taiwan (Fig. 1.2) is that the LSB/MV circulations work in tandem to exert major diurnal changes in surface flows, and thus, strong modifications to Mei-yu rainfall (Johnson and Bresch 1991; Chen and Li 1995; Kishtawal and Krishnamurti 2001; Kerns et al. 2010). The reversal of the LSB/MV circulations represents a prominent change, at least in magnitude, of the southwesterly monsoon flow impinging on the CMR (i.e., considering the diurnal circulations along western Taiwan). Consequently, the diurnal cycle of rainfall might be understood, at least in part, by considering the diurnal changes in moisture advection by the monsoonal southwesterly flow in connection with the LSB/MV circulations (Johnson and Bresch 1991).

Though the LSB/MV circulations are quite straightforward, the diurnal evolution in rainfall systems is complex, and that evolution evidently exerts its own impacts back on the diurnal circulations. For instance, though the early-afternoon peak in deep convection over Taiwan coincides well with maximum surface convergence associated with the diurnal circulations (as is expected), rainfall peaks slightly later in the afternoon (Chen and Li 1995; Kerns et al. 2010). This later peak in rainfall is related to upscale growth/maturing of convection, such that deep convective cells characterized by deep

heating maximize in the early-afternoon and subsequently evolve into more stratiform-type systems with upper-level heating and low-level cooling (Johnson and Bresch 1991). Further, evaporatively cooled downdrafts from mature convection likely enhance nighttime katabatic flows, which might be responsible for the enhancement of rainfall along the coastal plains and/or offshore overnight (Johnson and Bresch 1991; Kerns et al. 2010). The upscale growth and transition from deep heating-dominated convection to more stratiform convection, with elevated heating and low-level cooling, is consistent with the evolution of convection observed throughout the tropics on numerous time and space scales (Kiladis et al. 2009).

The Terrain-influenced Monsoon Rainfall Experiment (TiMREX; Jou 2011) was conducted in concert with the Southwest Monsoon Experiment (SoWMEX; Jou 2011) in the northern SCS and Taiwan during the 2008 Mei-yu season. The over-arching goals of SoWMEX/TiMREX (hereafter, TiMREX) were to improve understanding and predictability of severe-weather and heavy-rain-producing MCSs that are at times disastrous for local societies in the extremely mountainous island of Taiwan. Involved in accomplishing these goals is developing a better understanding of the relationships between MCSs embedded in the southwesterly Southeast Asian summer monsoon flow, shallow surface frontal boundaries, and complex coastal and mountainous topography and associated diurnal variability. This study addresses these core TiMREX goals – namely, we employ TiMREX datasets to analyze the diurnal cycles of a disturbed and undisturbed period during the Mei-yu season. Through comparison of the diurnal cycle between disturbed and undisturbed periods, we aim to 1) describe the complex relationships between rainfall and orographically modified flow, 2) better understand the

variability of the diurnal cycle as a function of large-scale forcing, and 3) determine the defining mesoscale and large-scale characteristics that distinguish convectively active and inactive periods in the Southeast Asian summer monsoon.

The present study is organized as follows: procedures employed to generate a regional reanalysis based on TiMREX datasets will be described next (Chapter 2); Chapter 3 will provide an overview of the evolution of large-scale circulation and rainfall patterns during TiMREX; Chapter 4 will present results of the diurnal cycle analysis; Chapter 5 will contain discussion; lastly, Chapter 6 will provide a summary, the principal conclusions of the study, and future work.

2. DATA AND METHODS

2.1 Observations from TiMREX and other sources

The 2008 TiMREX (Terrain-influenced Monsoon Rainfall Experiment) field campaign was conducted to better sample the flow fields characterizing the Mei-yu season in the region of Taiwan and the northern SCS (Jou 2011). The time period in which detailed observations were carried out in TiMREX, the special observing period (SOP), spans 15 May–26 June 2008, during which time networks of rawinsondes, dropsondes, and surface stations were deployed around Taiwan. The key scientific objectives of TiMREX were improved understanding of the following (Jou 2011):

1. *The effects of steep terrain and characteristics of upstream flow on the distribution and intensity of rainfall;*
2. *The role of the Mei-yu front and associated maintenance processes in the generation of heavy rain-producing MCSs that effect Taiwan;*
3. *The relationships between diurnal processes such as land–sea breeze and mountain–valley circulations and the timing, intensity, and distribution of rainfall.*

In order to address the above goals, a data assimilation (DA) system was employed to generate a regional reanalysis (hereafter, REANAL) for the TiMREX SOP using special observation datasets from TiMREX. As shown in Fig. 2.1, the domain over which REANAL was generated (with 0.25° grid spacing) includes a large area over southeastern China and the northern SCS west-southwest of Taiwan. This is important for

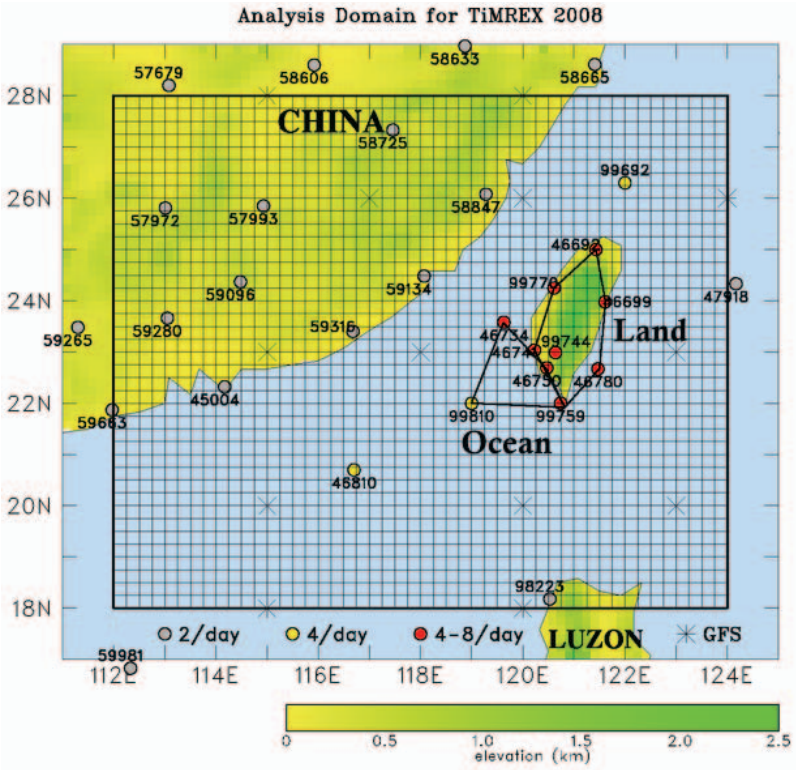

Fig. 2.1. Domain of the reanalysis (REANAL) based on data from the 2008 Terrain-influenced Monsoon Rainfall Experiment (TiMREX). The TiMREX enhanced sounding array (ESA) is indicated by the polygons (which include the Ocean and Land sub-domain ESAs). Color fill of sounding sites corresponds with sounding frequency, as indicated. Terrain is shaded according to the color bar.

capturing key aspects of the southwesterly summer monsoon flow. The most valuable data from TiMREX for this study are the tropospheric vertical profiles from the enhanced sounding array (ESA), which was composed of land sites in Taiwan as well as sites in the northern SCS and Taiwan Strait (Fig. 2.1). As indicated in Fig 2.1, all of the sounding stations in the ESA collected data at 4-day^{-1} frequency during the SOP (at 0000, 0600, 1200, and 1800 UTC). During an enhanced observing period (EOP) from 28 May–6 June, when the Mei-yu front was positioned over Taiwan and associated with heavy rainfall throughout the region, the sounding frequency at most sites was increased to 8 day^{-1}, adding intermediate sampling at 0300, 0900, 1500, and 2100 UTC. Sixteen dropsonde

missions were also carried out during such periods of heightened activity. Along with the TiMREX sounding data, the following datasets were also employed in this study:

- Operational sounding observations from China (shown in Fig. 2.1)
- Satellite soundings from Constellation Observing System for Meteorology Ionosphere and Climate (COSMIC);
- Oceanic surface wind observations from QuikSCAT (Quick Scatterometer);
- Standard surface observations (wind, temperature, pressure, and humidity) from the Central Weather Bureau of Taiwan and Meteorological Assimilation Data Ingest System (MADIS);
- Vertical profiler wind data;
- Global Positioning System (GPS) precipitable water (PW) observations;
- Standard aircraft observations from Aircraft Meteorological Data Reporting (AMDAR) and Aircraft Communication Addressing and Reporting System (ACARS), distributed by MADIS.

Most of these datasets are operational and go through some degree of quality control prior to distribution, so no quality-control procedures were applied prior to running the DA procedures. The sounding data, however, went through extensive correction procedures. As has been the case in previous field experiments such as TOGA COARE (Tropical Ocean Global Atmosphere Coupled Ocean–Atmosphere Response Experiment; Loehrer et al. 1996; Wang et al. 2002; Ciesielski et al. 2003), some of the sounding systems in the TiMREX ESA exhibited data accuracy issues (mostly in

humidity), which was complicated further by the fact that the TiMREX network was composed of four different sounding system types (Vaisala RS80, Vaisala RS92, Meisei, and GRAW; Ciesielski et al. 2010). Thus, issues varied slightly from one sounding site to another. Owing to early detection of these issues, a series of intercomparison launches were conducted with the Vaisala RS92 system (the most reliable instrument), which assisted with bias correction during post-processing. An in-depth discussion of the sounding issues, correction procedures, and the resulting improvements to the dataset is provided by Ciesielski et al. (2010).

2.2 Reanalysis methodology

Numerous studies have invoked interpolation methods for gridding observations from field experiments so that diagnostic quantities such as vertical motion and divergence could be calculated over broad areas in order to analyze targeted phenomena (e.g., Nuss and Titley 1994; Ciesielski et al. 2003; Johnson et al. 2007; Johnson et al. 2010). Issues that come about with this approach are that resulting gridded fields 1) are unrealistically smooth due to the inevitable inadequacies in observation density, 2) contain all the inherent error that is not removed by quality-control procedures, and 3) are not constrained by any sort of mass–wind balance relationship (though some studies apply mass-balance; e.g., Johnson et al. 2010). Formulating one of the key motivations of global and regional reanalysis projects, modern DA techniques can be employed to *re-analyze* previously observed environments by combining forecasts from modern numerical weather models with all available observations, which can include datasets

from field experiments. The use of enhanced observation datasets from field experiments can dramatically improve the representation of atmospheric processes in model analyses and forecasts (Kalnay et al. 1996; Miguex-Macho and Paegle 2000; Mo et al. 2005; Uppala et al. 2005; Mesinger et al. 2006; Mo et al. 2007). For instance, Faccani et al. (2009) demonstrate that the assimilation of sounding observations from AMMA (African Monsoon Multidisciplinary Analysis, 2006) subsequent to quality control procedures (removal of dry biases), results in dramatically improved model representation of the African easterly jet as well as moisture and precipitation fields over most of North Africa. Further, they show that forecasts improve as far as three days out over the European subcontinent when they include these sounding observations. Though this is an encouraging finding, observations from field experiments often do not make it into the operational global analyses and forecasts, or even into the global reanalyses generated *a posteriori*. Further, even if the observations do make it into the reanalyses, computation limitations often mean that the reanalyses are generated on too coarse of domains for analyzing processes at the mesoscale. For instance, the dynamics of flows in Taiwan would be described by a total of about two grid points using the global reanalysis dataset described in Kalnay et al. (1996).

With recent advances in DA, which have resulted in more accurate and computationally efficient procedures (e.g., Wang et al. 2008a, b; Meng and Zhang 2008; Huang et al. 2009; Zhang et al. 2009; Zhang et al. 2011), there is a new ability to invoke DA to create a better description of the phenomena targeted by field experiments. The Weather Research and Forecasting model, maintained by the National Center for Atmospheric Research, features a DA system (WRFDA) with the capability of

performing many of the widely accepted DA methods, such as three- and four-dimensional variational (3DVAR and 4DVAR; Barker et al. 2004; Wang et al. 2008a, b; Huang et al. 2009). These DA methods, which originated from test bed studies, have been effectively worked into WRFDA and tested by WRFDA software architects prior to public distribution (e.g., Barker et al. 2004). Many studies have demonstrated the success of the WRFDA system and similar systems through intercomparison tests in large-scale and mesoscale modeling (e.g., Dirren et al. 2007; Meng and Zhang 2008; Torn and Hakim 2009; Majumdar et al. 2010; Torn 2010; Zhang et al. 2011).

The selected DA method for this study is 3DVAR because of its computational efficiency and long duration of employment within the operational numerical weather prediction community, which lends credence to its abilities [e.g., 3DVAR has been employed by NCEP (National Centers for Environmental Prediction) models since 1991; Derber et al 1991; Kleist et al. 2009]. It is generally understood that more advanced DA techniques (e.g., ensemble-based and 4DVAR methods) outperform 3DVAR in forecast applications (e.g., Whitaker et al. 2009), and most national numerical weather prediction centers have indeed switched to such methods (e.g., Rabier et al. 2000). However, the present study is greatly advantaged by the availability of *a posteriori* model forecasts for the entire time period of analysis, as will be explained below.

Like other variational DA systems, the 3DVAR system in WRFDA is formulated on the grounds that estimates of the true state of the atmosphere, as provided by observations and model forecasts (serving as "background"), have error, and that the best estimate of the true atmospheric state (the "analysis" x) can be determined by minimizing the prescribed cost function $J(x)$:

$$J(x) = J^b + J^o = \frac{1}{2}\left(x - x^b\right)^{\mathrm{T}} \mathbf{B}^{-1}\left(x - x^b\right) + \frac{1}{2}\left(y^o - h(x)\right)^{\mathrm{T}} \mathbf{R}^{-1}\left(y^o - h(x)\right), \quad (1)$$

where J^b (J^o) is the distance of the sum of squares to the background state x^b (observations y^o), **B** is the background error covariance matrix, $h(x)$ is the observation operator used to convert between analysis and observation space, and **R** is the representativeness error covariance matrix (Ide et al. 1997; Barker et al. 2004). While it is obvious that the best estimate, the resulting analysis x^a, should be some "distance" from the background, it is worth noting that x^a should indeed also be some distance away from observations, since they too are imperfect on account of representativeness errors (Ide et al. 1997; e.g., Ide et al. 1997). In our application, we use standard errors given in WRFDA for the different observation platform types, though we generate a new **B**. 3DVAR is disadvantaged by sole dependence on a static estimate for **B**, whereas more advanced DA methods implicitly account for flow-dependent error in the **B** by either running a separate model to predict the error (4DVAR; e.g., Huang et al. 2009) or using an ensemble of prior forecasts to provide a sense of the error or spread between ensemble members (Wang et al. 2008a, b). Since our application of DA is in the generation of a reanalysis, however, and we have at our disposal all forecasts for the time period of interest, we can determine a "climatology" estimate of **B** specific to our time period and region based on these forecasts. We do this by iteratively measuring differences between all 12- and 24-h forecasts valid for the same time [the "National Meteorological Center method;" Parrish and Derber 1992]. We can then employ this new background error to improve the DA procedure over what would result by using a global–annual

climatological background error. In WRFDA–3DVAR, *J* is calculated in terms of the *control variables* streamfunction, velocity potential, unbalanced pressure, and either specific or relative humidity (Barker et al. 2004). Mass–wind balance is achieved by deriving a geostrophically and cyclostrophically balanced pressure from streamfunction. Balanced pressure is then latitudinally weighted to account for the breakdown of geostrophy in the tropics.

2.3 Gridded datasets

For the generation of the TiMREX reanalysis (REANAL), the observations employed include all of the TiMREX and operational datasets described in Section 2.1, while operational 6-h forecasts from the 0.25° NCEP Global Forecasting System (GFS) served as background (which were linearly interpolated to match reanalysis grid spacing). We used 12- and 24-h forecasts from the GFS to generate the domain- and time period-specific background error estimates so that they would account for any model-specific biases. We also use GFS 0-h forecasts for comparison with REANAL, which sheds light on improvements made to the model by the DA procedures we invoke and special observations we employ. Yet another dataset (INTERP) was generated by gridding observations using the multiquadric interpolation scheme of Nuss and Titley (1994). This dataset is generated on the same spatial domain as REANAL (0.25° in latitude and longitude; Fig. 2.1). Generation of INTERP employed all of the observation datasets listed in Section 3.1 with the exception of the ACARS, AMDAR, and GPS PW datasets. Primarily based on observations, INTERP is used for comparison with REANAL to

demonstrate the robust meteorological features that are explained by observations, and also to reveal where the addition of model information in REANAL is beneficial in filling in gaps of data.

One issue found in REANAL was unrealistic moisture over Taiwan throughout the tropospheric column (relative to sounding observations). The unrealistic tropospheric humidity values, stemming from the background GFS datasets, were confined to areas of high terrain, which we suspect might be related to convective parameterization issues in the GFS. The humidity values were similarly unreliable in REANAL, since the background humidity field was too different from moisture from observations. We thus use water vapor mixing ratio *q* from INTERP, since it represents the closest gridded product to observations.

2.4 Diagnostic quantities

Following Yanai et al. (1973), we use the gridded datasets to calculate vertical profiles of *apparent heat source* Q_1 and *apparent moisture sink* Q_2, which permit determination of the vertical structure of precipitating systems. These terms are calculated as follows (Johnson et al. 2010):

$$Q_1 \equiv \frac{\partial \bar{s}}{\partial t} + \bar{\mathbf{v}} \cdot \nabla \bar{s} + \bar{\omega} \frac{\partial \bar{s}}{\partial p} = Q_R + L(\bar{c} - \bar{e}) - \frac{\partial \overline{\omega' s'}}{\partial p}, \quad (2)$$

$$Q_2 \equiv -L\left(\frac{\partial \bar{q}}{\partial t} + \bar{\mathbf{v}} \cdot \nabla \bar{q} + \bar{\omega} \frac{\partial \bar{q}}{\partial p}\right) = L(\bar{c} - \bar{e}) + L \frac{\partial \overline{\omega' q'}}{\partial p}, \quad (3)$$

where s = $c_pT + gz$ is dry static energy, Q_R is the radiative heating rate, L is the latent heat of condensation, c is the condensation rate, e is the evaporation rate, c_p is the specific heat of dry air, T is temperature, g is acceleration due to gravity, z is height, the overbar denotes an area average, and the prime represents a departure from that average. All other variables are standard notation. Vertical motion ω is diagnosed in each of the datasets described in Section 3.2 by vertically integrating the horizontal divergence δ in spherical coordinates. The lower boundary condition for ω is determined by calculating the terrain slope flow following the procedure of Ciesielski and Johnson (2008). The divergence field is mass balanced in the vertical by assuming adiabatic flow at the tropopause and using a constant divergence correction as described by O'Brien (1970). The details on the computation of Q_1 and Q_2 are provided by Johnson and Ciesielski (2000).

3. OVERVIEW OF THE TiMREX FIELD EXPERIMENT

3.1 Overview of the SOP

As shown in Fig. 3.1, a map of TiMREX SOP mean 850-hPa height, wind, and rainfall from the Tropical Rainfall Measuring Mission (TRMM; Kummerow et al. 2000) 3B42v6 algorithm (Huffman et al. 2007), the 2008 Mei-yu season was characterized by extensive regions of rainfall in excess of 10 mm day^{-1} in the southern China and northern

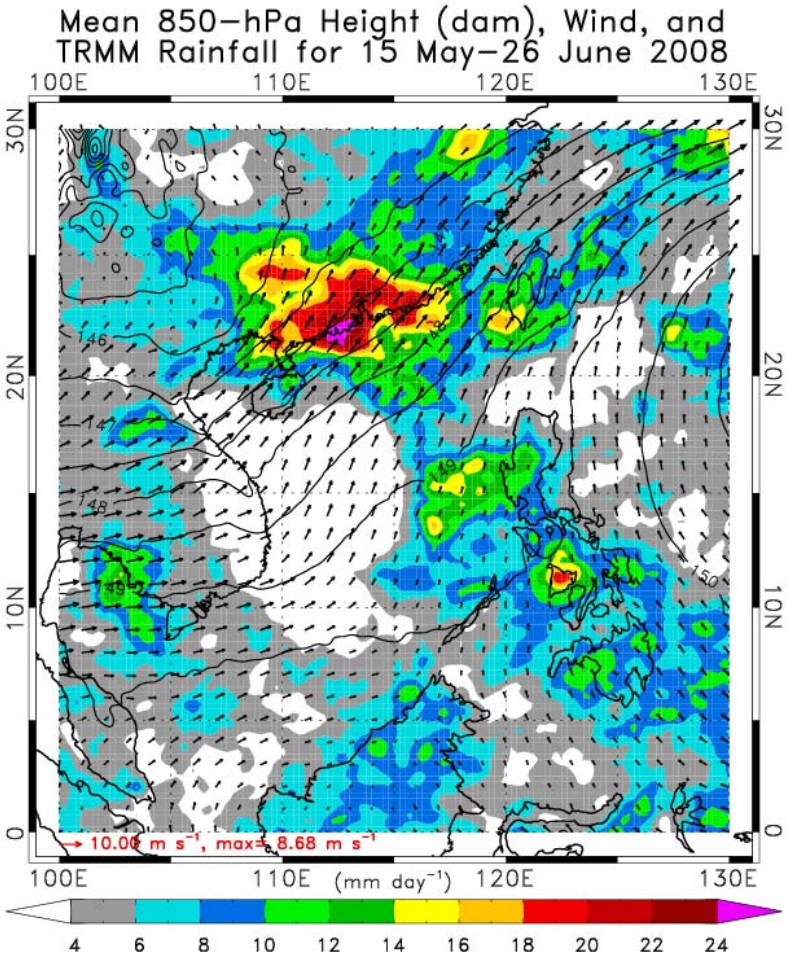

Fig. 3.1. Mean rainfall (mm day^{-1}) from the 3B42v6 algorithm from Tropical Rainfall Measurement Mission (TRMM) for the special observing period (SOP; 15 May–26 June 2008) of TiMREX (shaded according to the color bar; mm day^{-1}). 850-hPa height (contours; dam) and wind (vectors, reference and maximum value at bottom left; m s^{-1}) from GFS are overlaid.

SCS regions, in the presence of predominant southwesterly low-level flow. Though Fig. 3.1 provides a sense of the regional coverage of mean 2008 Mei-yu season rainfall, notable temporal variability was observed. Next provided are comparisons between different rainfall estimates from REANAL, INTERP, 0-h forecasts from GFS, TRMM, and Quantitative Precipitation Estimation and Segregation Using Multiple Sensors (QPESUMS), which is a radar-derived and rain gauge-corrected rainfall product (data only available in a box around Taiwan). Rainfall rate is derived by vertically integrating Q_2 (Eq. (3)) from REANAL, INTERP, and GFS. Surface latent heat flux is neglected from the vertically integrated moisture budget (e.g., Johnson and Ciesielski 2000) since no reliable sources for this quantity were available. Suspended liquid water in clouds is also neglected in this calculation. Nevertheless, the time series trends in rainfall rate can be compared to assess qualitative agreement and disagreement. Figure 3.2 provides SOP time series of daily-mean rainfall rate from the different estimates averaged over the Land and Ocean ESAs (with time-series mean values for $\bar{x}$ and TRMM-correlations r), demonstrating that most of the Mei-yu season rainfall was received during two marked disturbed periods (ACTIVE1: 1–6 June; and ACTIVE2: 13–17 June). These disturbed periods exhibit persistent heavy rainfall (e.g., ~4 days of ~35 mm day^{-1} or greater), separated by roughly 10 days (Fig. 3.2). Also shown in Fig. 3.2 is an asymmetry in rainfall between the Land and Ocean ESAs (particularly during ACTIVE2), which is most strongly captured by differences in TRMM and REANAL between the two ESAs. This asymmetry is also evident in Fig. 3.1, which shows a local maximum in SOP-mean rainfall (exceeding 16 mm day^{-1}) centered just southwest of Taiwan.

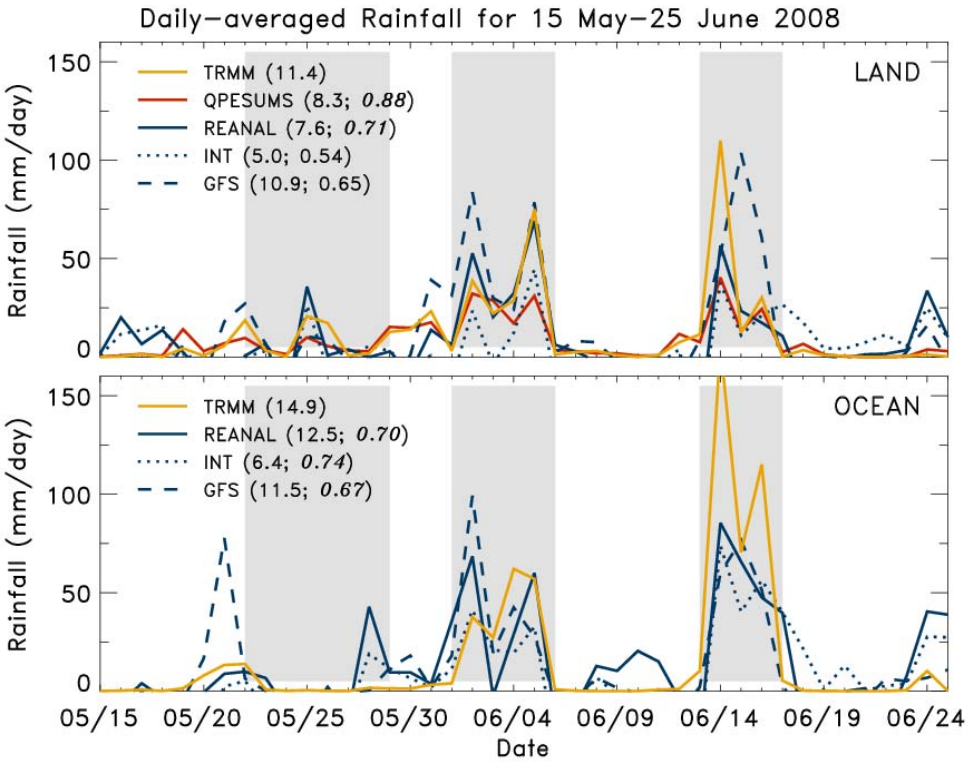

Figure 3.2. Domain-averaged (top: Land ESA; bottom: Ocean ESA) time series of daily-mean rainfall (mm day^{-1}) for the TiMREX SOP from TRMM, QPESUMS (Quantitative Precipitation Estimation and Segregation Using Multiple Sensors), REANAL, the interpolated analysis (INTERP), and 6-h forecasts from the National Centers for Environmental Prediction Global Forecasting System (GFS). All Q_2-derived rainfall estimates are in blue. The first numbers in parentheses are time series mean values $\overline{x}$, and the second are correlation with TRMM *r* (95% confidence was established for the italicized *r* values using a Student's *t*-test, though TRMM–QPESUMS correlation was tested to the 99% confidence level). Gray-shaded areas denote UNDIST (22–29 May), DIST (or ACTIVE1; 1–6 June), and ACTIVE2 (13–17 June).

Notable spread between the different rainfall estimates is demonstrated in Fig. 3.2, with TRMM being the wettest over both domains (i.e., note TRMM $\overline{x}$ in both ESAs compared to the other estimates). Though the causes for the substantial magnitude differences between TRMM and QPESUMS over the Land ESA are unclear, it is encouraging that the temporal variability is very similar between the two datasets, as demonstrated by high TRMM–QPESUMS correlation (r = 0.88, significant to the 99% confidence level). Since TRMM is available over both domains, we use this estimate to compare and evaluate the Q_2-derived rainfall estimates through correlation, and consider

this to be warranted based on close agreement with QPESUMS over the Land ESA (assumed to be a more accurate rainfall estimate over Taiwan). Note that REANAL is the intermediate of the Q_2-derived rainfall estimates in $\bar{x}$, with the highest TRMM correlation ($r = 0.71$) of these estimates. In contrast, $\bar{x}$ from REANAL is higher than the other two Q_2-derived estimates over the Ocean ESA, though all three correlate quite strongly with TRMM there. Neglecting internal TRMM error, agreement with TRMM in both ESAs (in terms of correlation) provides confidence in REANAL.

Figure 3.3 provides TiMREX SOP time–pressure sections from REANAL for the Ocean ESA, including daily-mean zonal wind u, meridional wind v, relative humidity RH (with respect to ice where <0°C), and saturation moist static energy $h_s = s + Lq_s$, where q_s is saturation water vapor mixing ratio. Onset of the monsoonal southwesterly low-level flow occurred on 22 May, and was not coincident with notable rainfall in the Ocean or Land ESAs (Fig. 3.2, disregarding the rainfall suggested solely by GFS in the Ocean ESA). Most of the SOP is characterized by lower-tropospheric conditional instability as suggested by the vertical gradient in h_s. The two disturbed periods were characterized by enhanced southwesterly flow within a deep layer extending from the surface (particularly ACTIVE2), with high RH extending into the upper troposphere. The slight reduction in low-level conditional instability during the two rainy periods is consistent with the vertical mixing of h_s by convection, which has been observed in other regions of the tropics (Thompson et al. 1979). That the period from 18–22 May, which was characterized by deep moisture, did not coincide with heavy rainfall is consistent with a stable winter monsoon regime in the Taiwan vicinity. Evidence of this is provided by northeasterly surface flow and reduced conditional instability during the deep-moisture

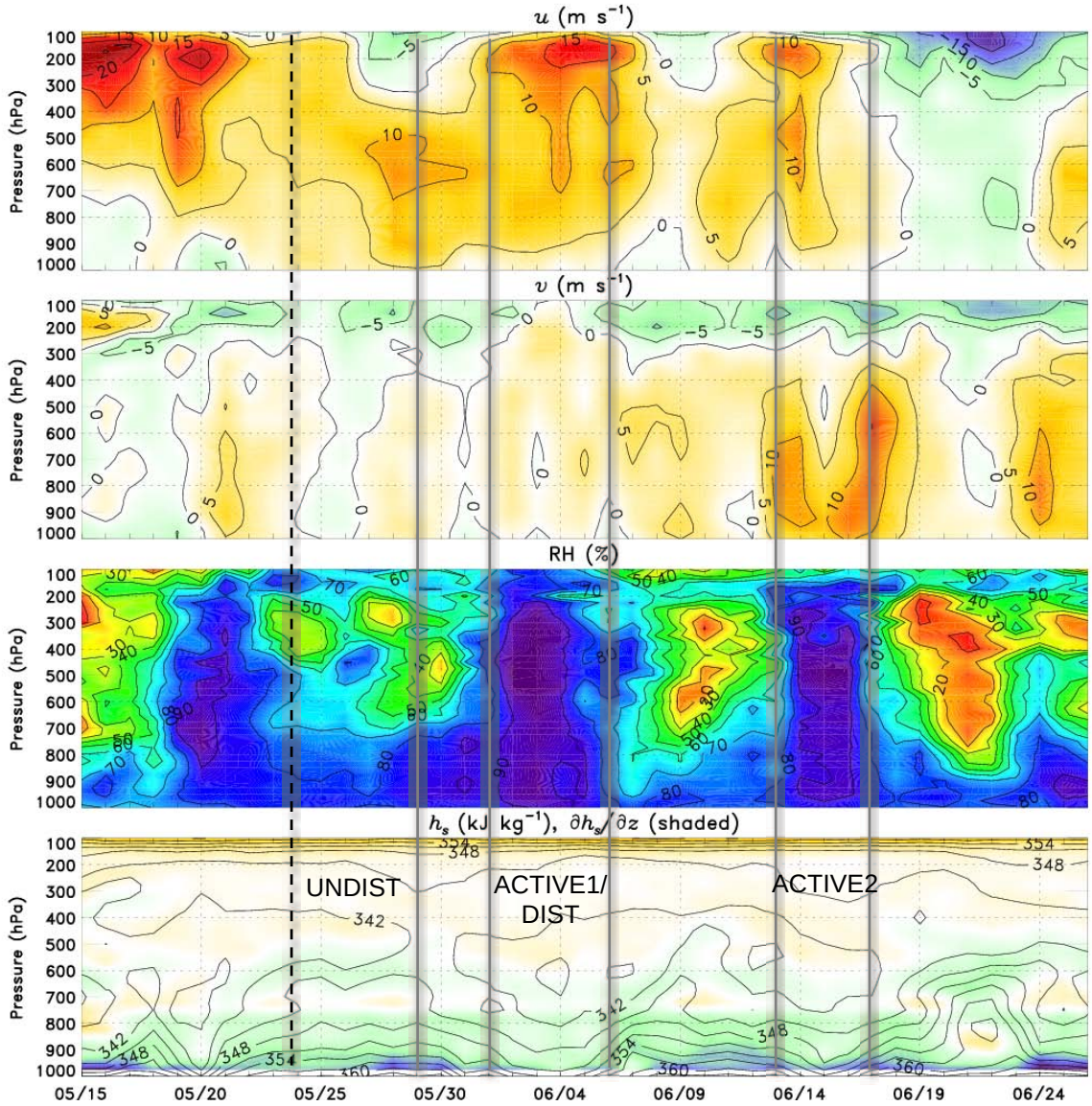

Fig. 3.3. Ocean ESA-averaged time–pressure sections from REANAL during the TiMREX SOP of daily-mean zonal wind u (top; m s^{-1}), meridional wind v (upper-middle; m s^{-1}), relative humidity RH (with respect to ice where <0°C; lower-middle; %), saturated moist static energy h_s (bottom; contours; kJ kg^{-1}), and vertical gradient in h_s (bottom; shaded; kJ kg^{-1} km^{-1}). Vertical dashed line denotes approximate onset of southwesterly low-level flow (22 May 2008). UNDIST, ACTIVE1/DIST, and ACTIVE2 are indicated.

event, which was associated with the passage of a strong, deep trough, as suggested by the transitions in u and v (Fig. 3.3). Note the lowering of strengthened westerly momentum during the period 22~28 May. Shortly following the time at which this flow reaches the surface, a period of gradual moistening (and deepening of moisture) in the

lower troposphere commences. Onset of this moistening also appears to be coincident with a switch to $v > 0$ through a deep layer. This development of deep southwesterly flow, which usually accounts for enhanced moisture flux convergence in the northern SCS region, likely reflects spin-up of the broader Asian summer monsoon system, as it appears to occur independent of a strong upper-level system (Ding and Chan 2005). The observed periodicity during the SOP, most notable in tropospheric RH (Fig. 3.3), is on the order of ~10 days. Mao and Chan (2005) note that summer monsoon variability in the SCS region is dominated in certain years by the 1020-MM (and by the 3060-MM in others). The periodic pattern in RH might be a reflection of predominance of this 1020-MM during the 2008 season.

Figure 3.4 provides TiMREX SOP time–pressure sections of daily-mean δ, ω, Q_1, and Q_2 from REANAL for the Ocean ESA, revealing the marked signatures of deep moist convection during ACTIVE1 and ACTIVE2: vigorous deep-tropospheric ascent (consistent with the vertical profile in δ) coincident with deep apparent heating and drying. Together, Figs. 3.3 and 3.4 demonstrate patterns of convective evolution that resemble the "self-similar" nature of equatorial moist-convective modes, including the MJO (Kiladis et al. 2009). For instance, the moisture and convective evolution for the period 27 May–8 June can be summarized as follows (Figs. 3.3 and 3.4): gradual lower-tropospheric moistening and deepening of moisture coincides with predominantly weak/shallow, though deepening convection (e.g., note a divergence maximum centered near and above 800 hPa, with reduced upward motion above), while lower-tropospheric instability and mid–upper-tropospheric warm anomalies maximize (as inferred from patterns of h_s; 27 May–1 June); tropospheric-deep moisture develops in association with

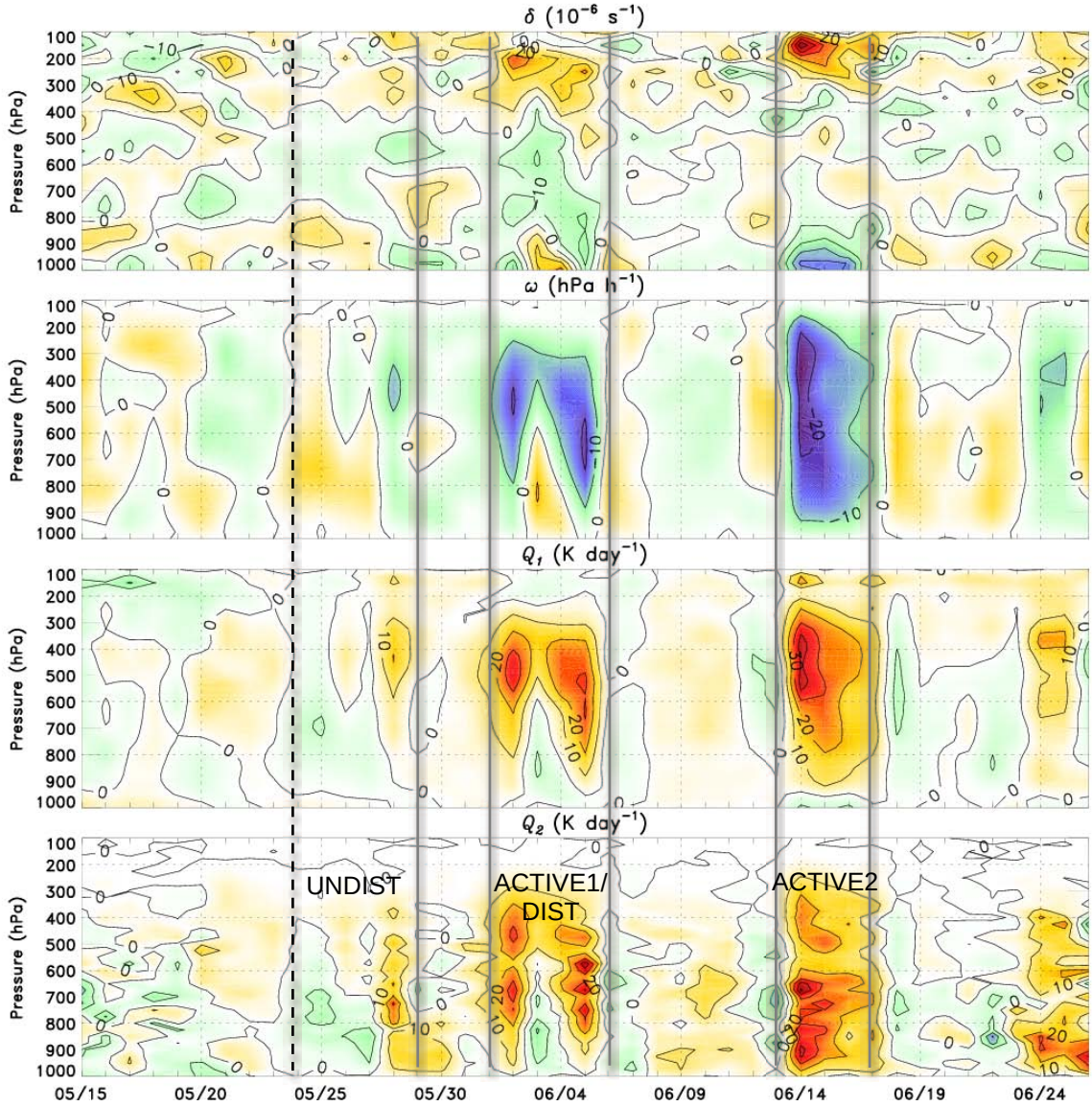

Fig. 3.4. As in Fig. 3.3 except for daily-mean divergence δ (top; 10^{-6} s^{-1}), vertical pressure velocity ω (upper-middle; hPa h^{-1}), apparent heat source Q_1 (lower-middle; K day^{-1}), and apparent moisture sink Q_2 (bottom; K day^{-1}). UNDIST, ACTIVE1/DIST, and ACTIVE2 are indicated.

vigorous deep moist convection, as lower-tropospheric instability and mid–upper-level warm anomalies are substantially mixed out (1–5 June); upper-tropospheric moisture persists with rapid lower-tropospheric drying as deep moist convection subsides and convectively-cooled downdrafts take over (5–8 June). Following this roughly two-week

evolution, the pattern begins again as lower-tropospheric moistening primes the troposphere for deep moist convection during ACTIVE2.

Interestingly, deep moist convection appears to be more vigorous during ACTIVE2 than ACTIVE1: note deeper and more intense ascent and apparent heating and moistening, a higher and stronger upper-tropospheric divergence peak, and stronger lower-tropospheric convergence during the later active period (Fig. 3.4). Figure 3.2 corroborates with this asymmetry in convective vigor, as most estimates exhibit greater rainfall during ACTIVE2 in the Ocean ESA. Note that the deep-tropospheric flow was more southerly and stronger during ACTIVE2 (Fig. 3.3), suggesting a more direct connection of low-level moisture transport from the southern hemisphere by the cross-equatorial flows (e.g., Ding and Chan 2005). Johnson and Ciesielski (2002) noted a similar trend in convective activity in their analysis of the 1998 Mei-yu season (which in fact exhibited similar week-to-ten-day breaks between active convection). They demonstrated that sea surface temperature increased in the northern SCS with the progression of the season. It is possible that warmer sea surface results in increased convective instability during later periods which, combined with stronger southerly flow, might explain the increased convective vigor in the later 2008 active period (Fig. 3.4).

3.2 Comparison between an undisturbed and disturbed period

To demonstrate some of the key features that distinguished undisturbed and disturbed periods (i.e., convectively inactive and active periods) during TiMREX, we next compare some of the synoptic features associated with a characteristically

undisturbed period (UNDIST: 22–29 May 2008) and a characteristically disturbed period (DIST: 1–6 June 2008).

Figure 3.5 provides a map of mean 850-hPa height, wind, and TRMM rainfall for UNDIST. The most obvious difference from Fig. 3.1 is that rainfall is largely confined to land areas in the northern SCS region (with the exception of an area east of Taiwan), despite appreciable low-level conditional instability (Fig. 3.3) and a southwesterly flow pattern extending from the Indochina Peninsula (a favorable characteristic for convective

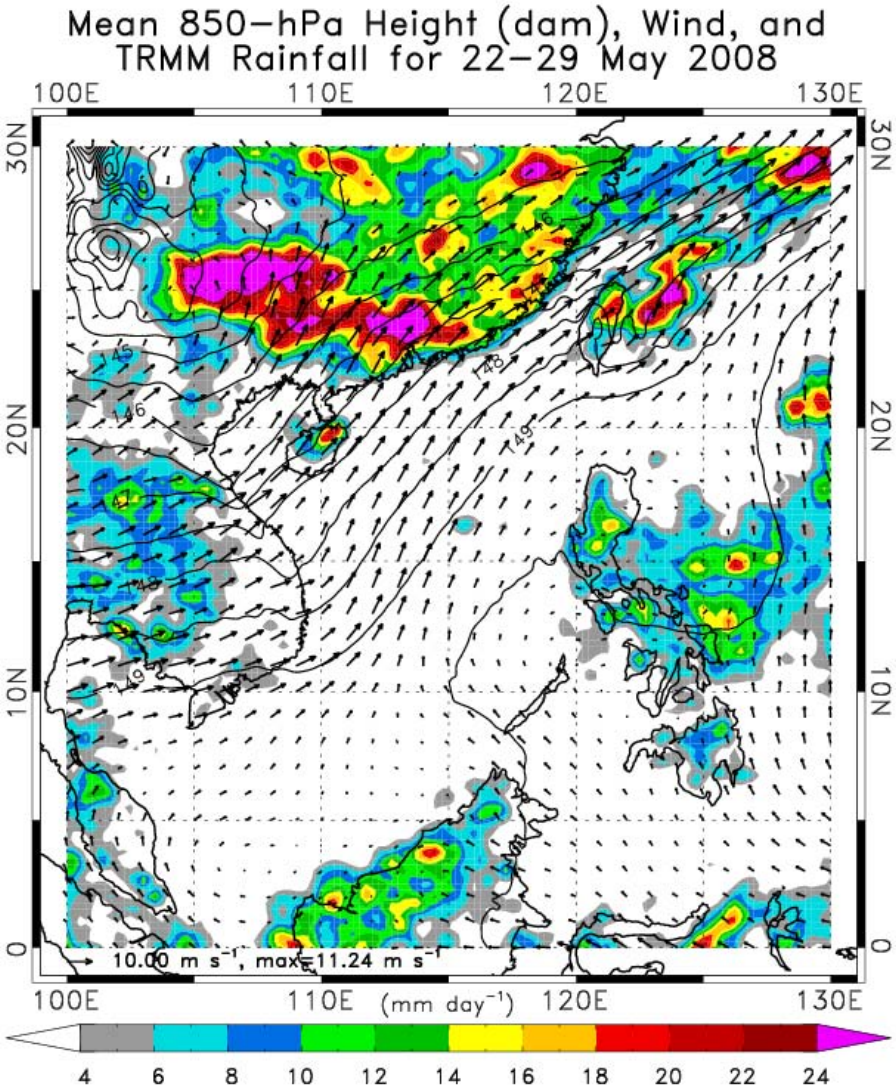

Fig. 3.5. As in Fig. 3.1, except for UNDIST.

activity; e.g., Hung and Hsu 2008). It is possible that reduced tropospheric RH (Fig. 3.3) and a lack of large-scale forcing or triggering mechanism is cause for the lack of vigorous deep convection in the Taiwan vicinity during this period, which would suggest that local, e.g., diurnal variability would account for the observed rainfall. Figure 3.6 provides a map of mean 200-hPa height and wind for UNDIST, demonstrating the dominance of the characteristic 200-hPa Asian monsoon anticyclone (e.g., Ding and Chan 2005). Note that the flow is quite zonal and reaches up to ~25 m s^{-1} around and north of Taiwan.

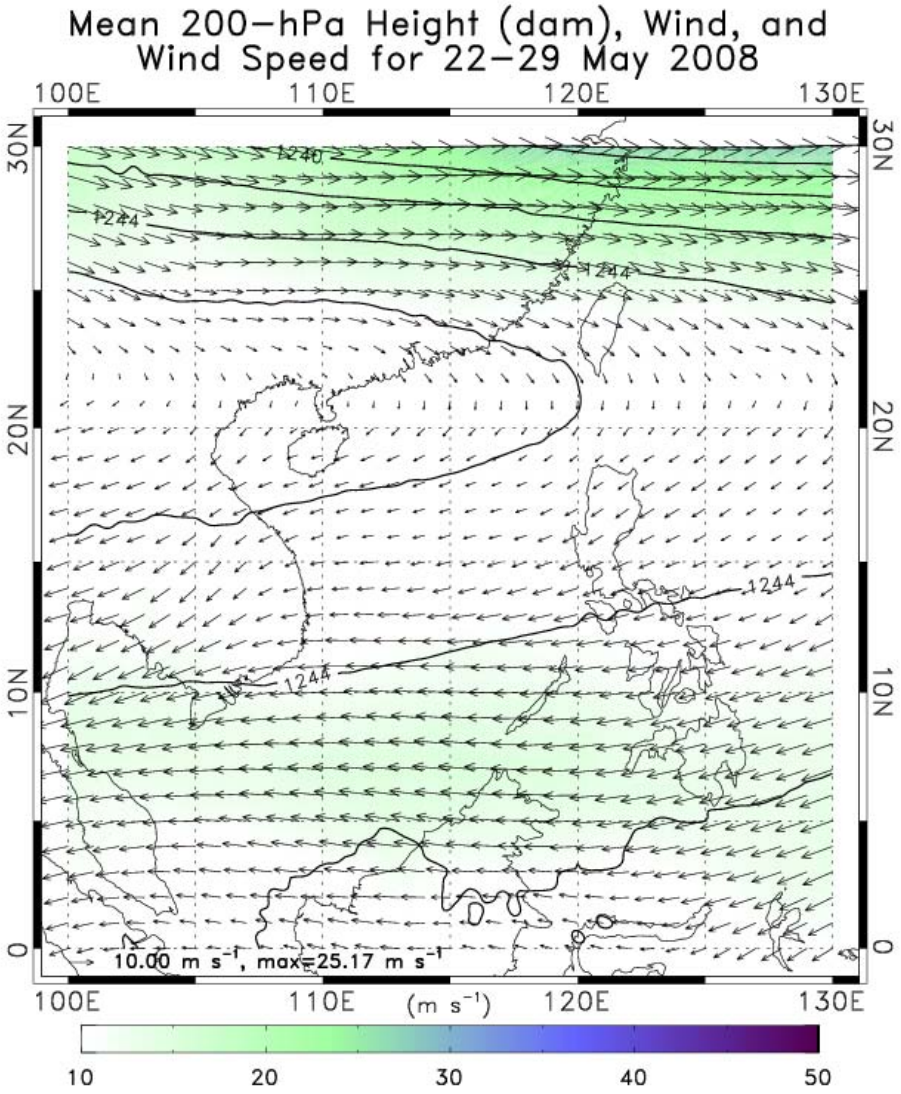

Fig. 3.6. Map of 200-hPa height (dam), wind velocity (vectors; reference and maximum value at bottom-left; m s^{-1}), and wind speed (shaded according to the color bar; m s^{-1}) for UNDIST.

Figure 3.7 provides the mean rainfall and 850-hPa patterns for DIST, and unmistakable is the dominance of an elongated zone of heavy rainfall in the northern SCS and across southern Taiwan. Interestingly, DIST is characterized by significant westward extension of the West Pacific subtropical anticyclone into the SCS (relative to the mean SOP and UNDIST patterns), which is associated with a focused region of enhanced southerly (west-southwesterly) flow along its western (northwestern) flank. In association with this concentrated west-southwesterly flow across the northern SCS is a band of

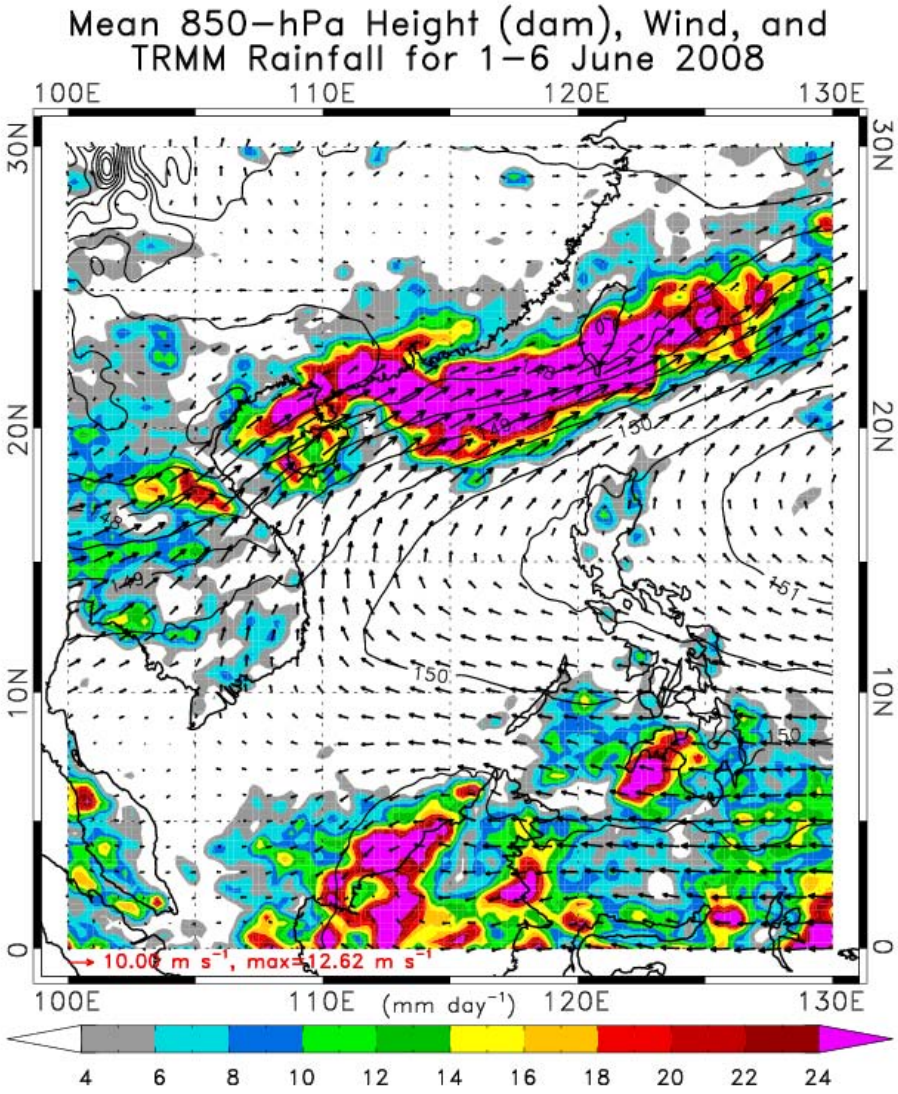

Fig. 3.7. As in Fig. 3.1, except for the period 1–6 June (DIST).

enhanced cyclonic shear (i.e., note the stark reduction in flow speed along the north side of the ~southwesterly stream). This band of enhanced cyclonic shear is the signature of the Mei-yu front, which was associated with northerly cold intrusions down into the Taiwan Strait and east of Taiwan during DIST (periodic near-surface northerly flow during this period in Fig. 3.3 reflects these cold intrusions). Consistent with previous studies of the Mei-yu front (e.g., Chen 2004), MCSs developed and propagated eastward along the concentrated frontal vortex line (not shown), which resulted in concentrated rainfall along and to the south of the line, including southern Taiwan (Fig. 3.7; Lai et al. 2011; Davis and Lee 2012). The 200-hPa flow pattern during DIST (Fig. 3.8) reveals much stronger westerly flow (e.g., ~45 m s^{-1}) along the northern side of the monsoon anticyclone compared to UNDIST. Of particular interest is that the downstream side of an upper-level trough to the north of the anticyclone sits across the northern-SCS region. Through the implication of differential vorticity advection (increasing cyclonic vorticity advection with height), this suggests that large-scale forcing for ascent might have assisted rainfall development during this period. In fact, the evolution of upper-level flow in Fig. 3.3 suggests that passage of the base of the trough (and subsequent positioning of Taiwan within the area of implied large-scale forcing for sinking motion) closely coincides with the end of the period of deep moisture and active convection (Figs. 3.3 and 3.4). The slight lowering of maximum upper-tropospheric divergence during DIST (from 2–5 June) lends evidence to passage of the axis of a cold-core system (Fig. 3.4).

It is possible that, consistent with previous studies (Chen 1993), the Mei-yu front associated with heavy rainfall during DIST was initially (prior to DIST) connected to the upper-level trough (Fig. 3.8) while in subtropical China. Though, upon dropping

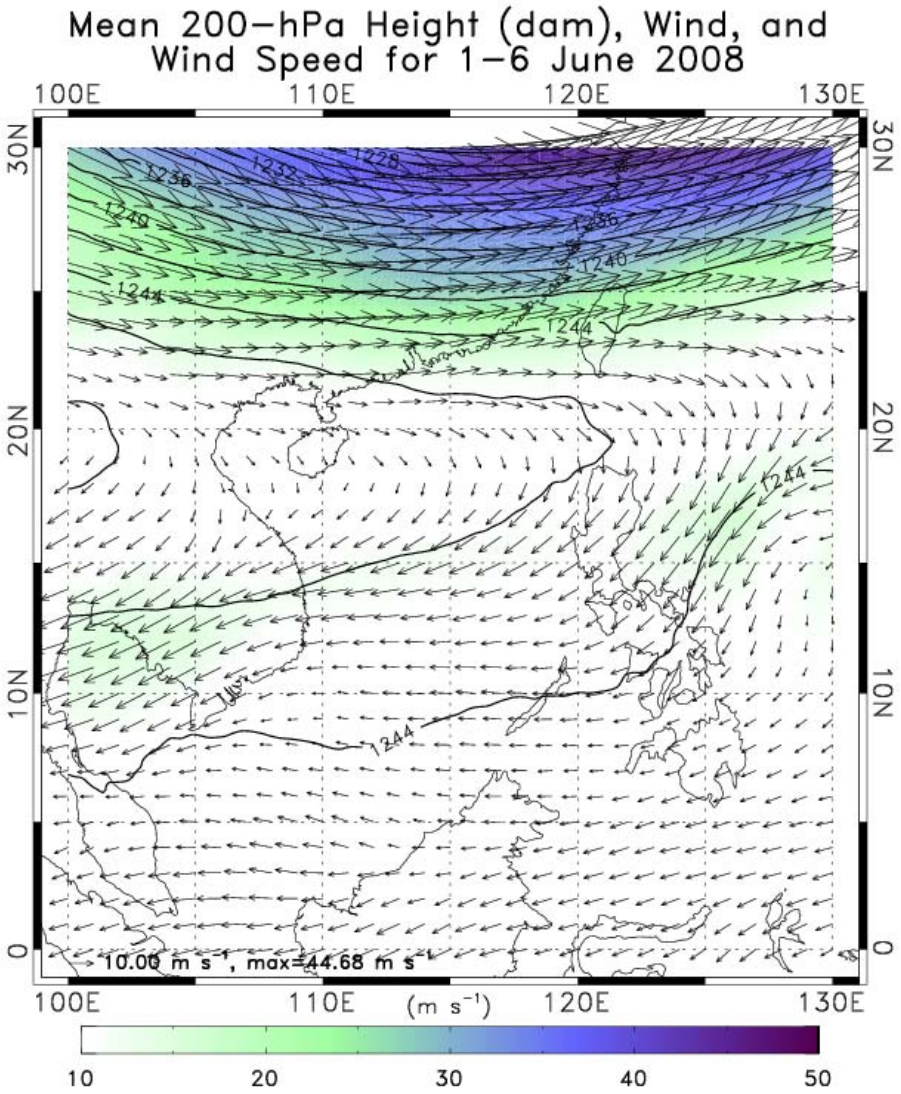

Fig. 3.8. As in Fig. 3.6 except for DIST.

southward and losing much of its baroclinicity (e.g., via sensible heating from a warmer sea surface; Trier et al. 1990), it became more of a shallow, density-current-type structure maintained by feedbacks with the diabatic heating in MCSs (Lai et al. 2011). The positioning of the upper-level trough relative to the Taiwan region during DIST suggests that Taiwan was in a favorable area for synoptic-scale rising motion. Though perhaps not connected with the surface Mei-yu front, this trough could have served to precondition the environment for convection during DIST by enhancing free-tropospheric moistening.

In summary, the 2008 Mei-yu season was characterized by enhanced rainfall in southeastern China, Taiwan, and the northern SCS in the presence of predominant southwesterly flow (Fig. 3.1), as is typical of this stage of the East Asian summer monsoon (Ding and Chan 2005). Rainfall came mostly during two convectively active periods – ACTIVE1 (1–6 June) and ACTIVE2 (13–17 June) – which were separated by roughly 10 days (Figs. 3.2, 3.3, and 3,4). The evolution of tropospheric moisture associated with ACTIVE1 can be summarized as follows: deepening of lower-tropospheric moisture precedes ACTIVE1 deep convection; moisture is established throughout the troposphere during ACTIVE1 deep convection; and a transition to lower-tropospheric drying is established with the end of ACTIVE1 deep convection and switch to deep sinking motion. This moisture evolution and its relationship with convection resembles the "self-similar" nature of equatorial moist-convective modes, including the MJO (Kiladis et al. 2009).

During a characteristic inactive period of the Mei-yu season (UNDIST: 22–29 May 2008), during which time mean rainfall in Taiwan was generally suppressed (Fig. 3.2), the rainfall that did occur was focused mainly over and near land areas under predominant southwesterly 850-hPa flow and a weak, zonal 200-hPa pattern (Figs. 3.5 and 3.6). During a convectively active period (DIST: 1–6 June 2008), in contrast, heavy rainfall in Taiwan (Fig. 3.2) was associated with a roughly west–east-oriented zone of enhanced convergence and vorticity at 850 hPa (Fig. 3.7), which marked the position of the Mei-yu front. During DIST, the 200-hPa flow was stronger and the Taiwan region was positioned slightly east of a 200-hPa trough (Fig. 3.8), suggesting a favorable environment for large-scale ascending motion.

4. ANALYSIS OF THE DIURNAL CYCLE DURING TiMREX

A spectral time series of rainfall during TiMREX demonstrates the dominance of diurnal variability in Taiwan during the summer monsoon season (Fig. 4.1). This is consistent with the mountainous topography and abundance of coastline in Taiwan (Fig. 1.2), permitting development of land–sea breeze (LSB) and mountain–valley (MV) circulations in the presence of daytime solar heating and nighttime cooling. As discussed by Davis and Lee (2012), the diurnal cycle in Taiwan is not uniform throughout TiMREX. It varies as a result of large-scale variability and associated impacts on, e.g., cloudiness, convective instability, and triggering mechanisms. Davis and Lee (2012) use the QPESUMS dataset to describe the TiMREX SOP rainfall characteristics in Taiwan. They demonstrate that afternoon convection over the terrain was commonplace during the early period of TiMREX (15 May–2 June), accounting for most May rainfall. In contrast, they note that much of the June rainfall was received in the form of intense, long-lasting events, during which time the diurnal cycle of rainfall was at times obscured.

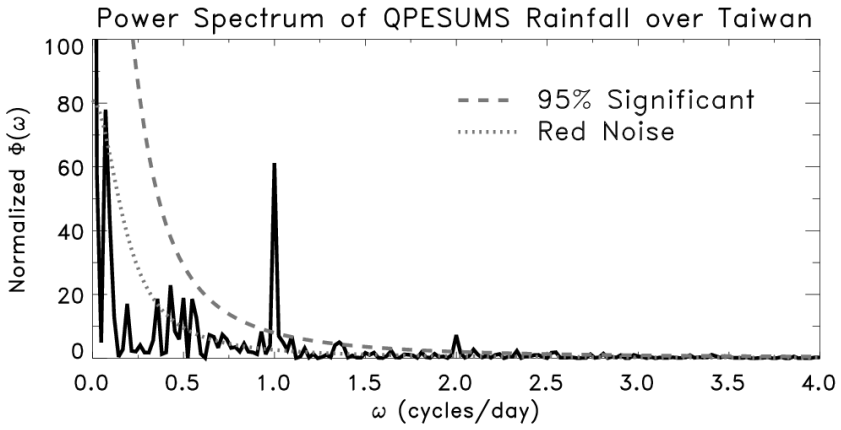

Fig. 4.1. Spectral time series of QPESUMS rainfall averaged over Taiwan. 95% significance and red noise curves are overlaid for reference. 95% significance was calculated using the F statistic and two degrees of freedom.

To attain a quantitative measure of diurnal variability and its variation throughout the TiMREX SOP, a time series of diurnal variance in T and U_{NORM} is provided (Fig. 4.2). U_{NORM} is the surface flow normal to the Taiwan coastline, which is calculated using a subjectively selected coast-normal angle (convention is such that onshore flow is positive). Diurnal variance, denoted by $(\ )_D$, is calculated for T and U_{NORM} as follows: each field is first standardized via removal of the SOP mean and dividing by the SOP standard deviation; 24-h variance is then calculated by squaring the 24-h standard deviation for each day. SOP time series of daily-mean QPESUMS rainfall and RH are also plotted for comparison. The former is averaged over Taiwan, while the latter is horizontally averaged over the northern SCS upstream of Taiwan (18–22°N, 112–120°E) and vertically averaged using mass weighting. All time series in Fig. 4.2 are smoothed using a three-day running mean. Important to consider is that diurnal variance, as calculated in Fig. 4.2, does not equate to diurnal periodicity; rather, it quantifies the measure of variability throughout the 24-h period each day. Characteristics of diurnal periodicity in rainfall and flow patterns will be assessed later.

Following rapid SCS moistening during the period leading up to monsoon onset, RH was observed to gradually increase up to the first heavy rainfall period (ACTIVE1), rapidly drop during and immediately following ACTIVE1, and slightly recover prior to ACTIVE2 (Fig. 4.2). This is consistent with an earlier discussion (cf. Chapter 3), in which the temporal relationships between heavy rainfall and tropospheric RH were suggested to resemble the “self-similar” nature of equatorial moist convective modes (Figs. 3.3 and 3.4; Kiladis et al. 2009). Figure 4.2 indicates that $(U_{NORM})_D$ and $(T)_D$ are reduced during the heavy rain events of ACTIVE1 and ACTIVE2, and are higher when

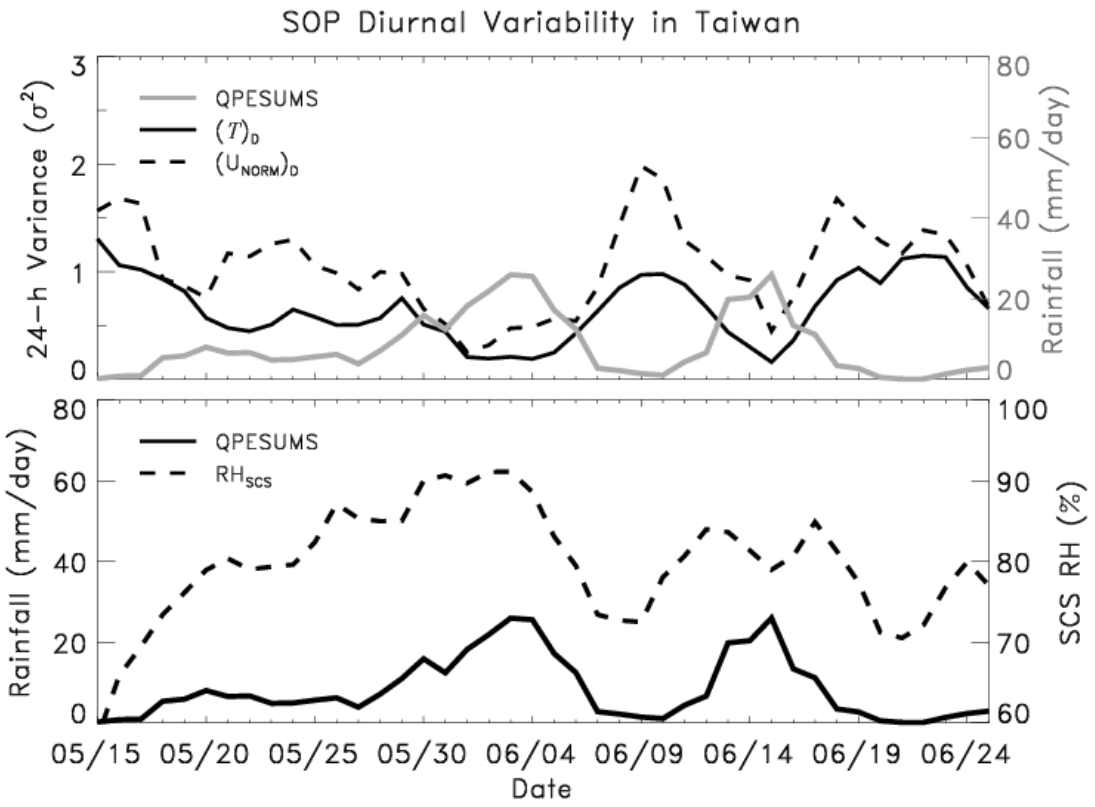

Fig. 4.2. Top: SOP time series of daily variance (black; left axis; σ^2) of coast-normal wind (U_{NORM}) and *T* and daily-mean QPESUMS rainfall averaged over Taiwan (gray; right axis; mm day^{-1}). Bottom: daily-mean QPESUMS rainfall averaged over Taiwan (gray; left axis; mm day^{-1}), and daily-mean RH (with respect to ice where <0°C) averaged over the northern SCS and from 1000–100 hPa using mass-weighting (gray; right axis; %). Variance of each field, denoted by $(\ )_D$, is calculated as follows: the time series is first standardized via removal of the SOP mean and dividing by the SOP standard deviation; 24-h variance is then calculated by squaring the 24-h standard deviation for each day. Each time series is smoothed using a three-day running mean.

rainfall is suppressed or completely absent (e.g., prior to and following ACTIVE2). The apparent correlation between $(U_{NORM})_D$ and $(T)_D$ is consistent with diurnal thermal forcing of the LSB and MV circulations, measurement of which are implicitly included in $(U_{NORM})_D$. Figure 4.3 provides time series of surface sensible and latent heat flux (LH) along with *T* and *q* from Pingdong, located in the coastal plains of southwestern Taiwan. The diurnal swing in sensible heat flux and *T* is large during most of May, while it is markedly reduced from approximately May 30–7 June. Together with Fig. 4.2, this

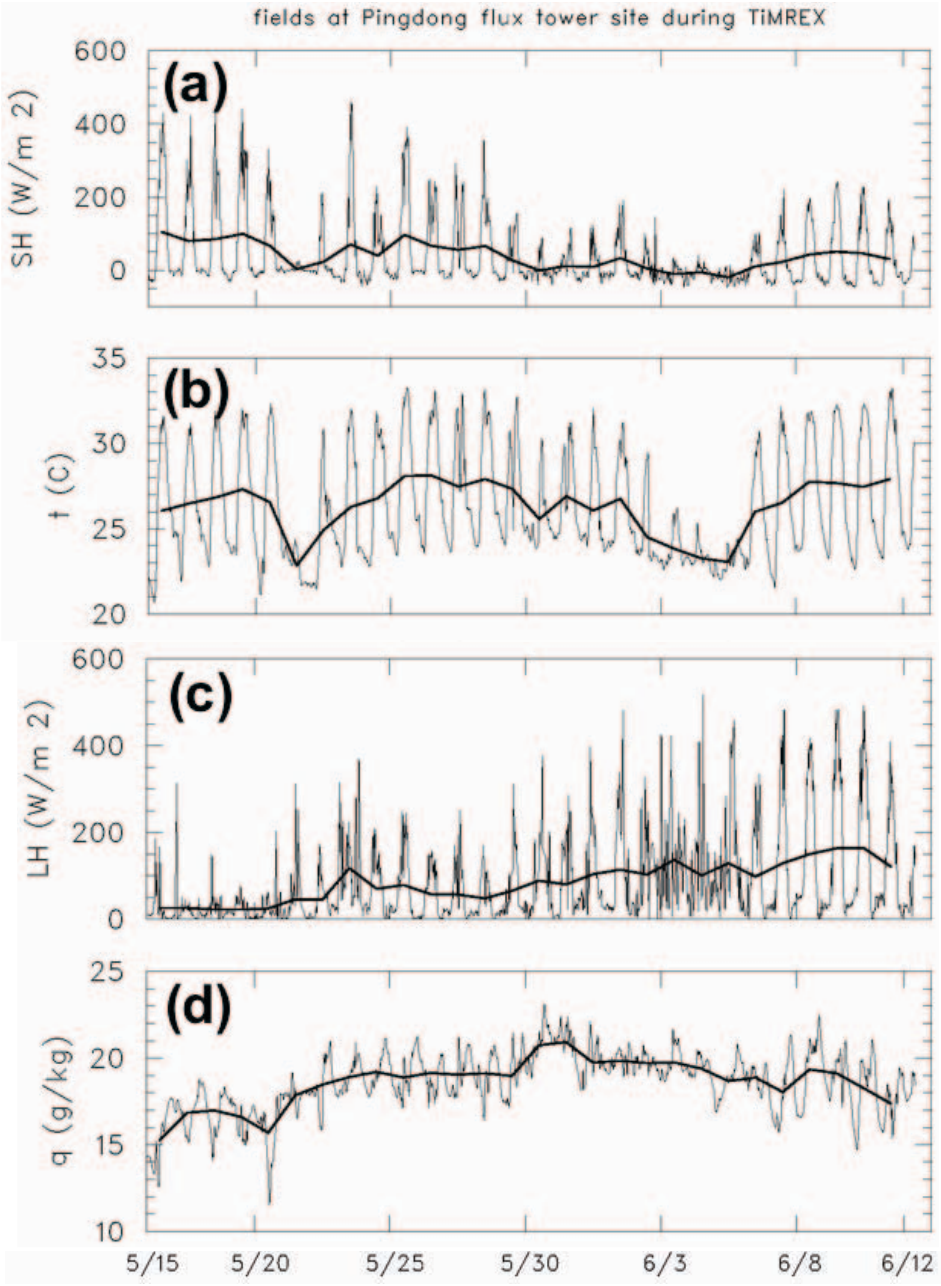

Fig. 4.3. Time series (date is along the x-axis) of sensible heat flux (a; W m^{-2}), *T* (b; °C), latent heat flux (c; W m^{-2}), and *q* (d; g kg^{-1}) from the Pingdong flux tower, located in the coastal plains of southwestern Taiwan. The jagged lines are raw data and the smooth lines are daily-averaged data. Data is unavailable following mid June.

suggests that reduction in $(T)_D$ and $(U_{NORM})_D$ during the heavy rain events is a consequence of the damping of insolation over the island by clouds and precipitation. Also demonstrated in Fig. 4.3 is a steady ramp-up of sensible heat flux with the

progression of the summer monsoon. This is a reflection of the increase in soil moisture during the monsoon in accordance with sequential heavy rainfall events. Note that, though there is increased noise in LH (Fig. 4.3c) in early June, diurnal variability in latent heat flux persists through this active rainfall period. This suggests that rainfall diurnal variance also persists through this period.

Considering that rainfall in the Taiwan region is strongly diurnally varying during the Mei-yu season (Fig. 4.1), progression towards improved understanding of rainfall processes in this part of the world comes from improved understanding of the diurnal cycle. Thus, herein we employ REANAL, the TiMREX reanalysis described previously (cf. Chapter 2), to describe the complex interactions between local, thermodynamically driven diurnal circulations and rainfall systems in Taiwan. We first examine the undisturbed early-summer period discussed in Section 3.2 (UNDIST: 22–29 May 2008), which offers a clear picture of these interactions during a period of enhanced diurnal variance in T and U_{NORM} (Fig. 4.2) and reduced cloudiness (Fig. 4.3). We then examine the disturbed period discussed in Section 3.2 (DIST: 1–6 June 2008), which demonstrates how the Mei-yu front and associated MCSs modify the local diurnal cycle (in the presence of suppressed diurnal T and U_{NORM} variance and enhanced cloudiness).

4.1 Diurnal cycle during UNDIST (22–29 May 2008)

i). Surface flows and rainfall

The period 22–29 May is chosen for discussion of relationships between rainfall and diurnal circulations under the conditions of persistent southwesterly monsoon flow and reduced daily-mean rainfall (relative to the disturbed periods; Fig. 3.2). Under weak flow conditions and with little daily-mean rainfall during UNDIST, strong diurnal variance in *T* and U_{NORM} was observed (Fig. 4.2), suggesting that the thermally forced diurnal LSB and MV circulations were prominent during this period. It is likely that strong connections existed between rainfall and local diurnal circulations (Johnson and Bresch 1991), and this will be investigated below.

According to Fig. 4.4, a map of UNDIST mean surface flow and rainfall, the flow during UNDIST was southwesterly, and mean rainfall was focused in land areas in China and Taiwan, though also with some areas extending offshore. The monsoon southwesterly flow is strongly modified by the island, which is consistent with Fr~0.3, as calculated from a mean upstream sounding for UNDIST (not shown). In particular, note accelerated ~southerly flow near northwestern Taiwan (a barrier jet), deflected westerly flow south of Taiwan, and enhanced easterly flow along the northeastern Taiwan coast in association with a lee-vortex/island wake pattern. These flow features are likely related to the development of a cross-barrier pressure couplet (Epifanio and Rotunno 2005; Li and Chen 1998; Yeh and Chen 2003). In association with conditionally unstable (Fig. 3.3), low-Fr flow, rainfall in Taiwan is maximized along the upwind slopes of the terrain and

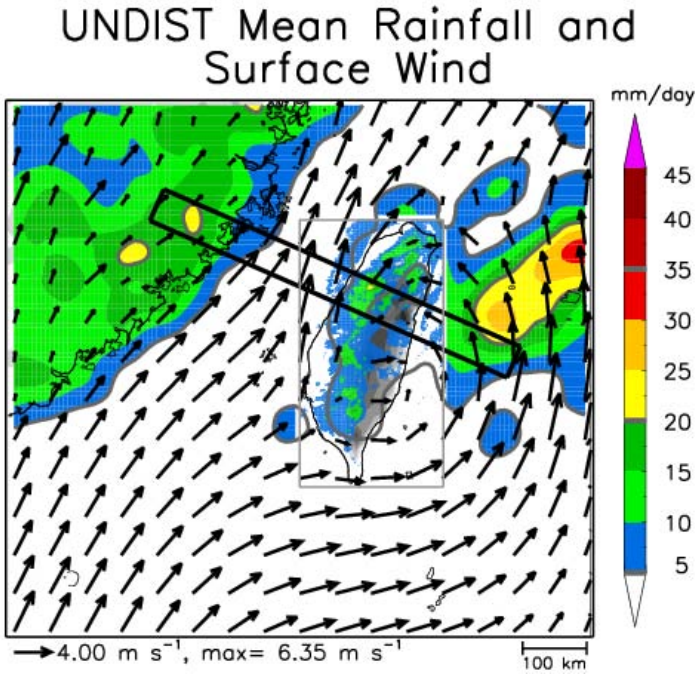

Fig. 4.4. Mean surface winds (reference vector and maximum value displayed at bottom; m s^{-1}), TRMM rainfall (shaded according to color bar surrounding QPESUMS domain, contoured according to gray ticks in color bar within QPESUMS domain; mm day^{-1}), and QPESUMS rainfall (shaded according to color bar; mm day^{-1}) for the period 22–29 May 2008 (hereafter, denoted UNDIST). Black box extending from eastern China into the western Pacific denotes a cross section discussed later (transect is the major axis, which is averaged over the minor axis). Gray box outlines the QPESUMS domain. Terrain is gray-shaded in ~440-m increments. Horizontal distance scale is provided at bottom-right.

in a small region in the lee of the northeastern peaks where the return-flow in the island wake meets the CMR (Chen and Lin 2005). There is also an area of rainfall just offshore from northwestern Taiwan in association with the deflected southerly flow (Yeh and Chen 2002), which resembles the rainband upstream of the Big Island of Hawaii. Similar to this feature (Fig. 4.4), the Hawaiian rainband is generated in low-Fr flow as a result of orographically enhanced offshore convergence (Smolarkiewicz et al. 1988; Carbone et al. 1995). Though the main cause for this enhanced convergence in Hawaii is evaporatively cooled density currents that develop along the upwind slope of the Big Island (Carbone et al. 1995), the dry dynamics of blocked flow can also contribute to this (Pierrehumbert and Wyman 1985; Smolarkiewicz et al. 1988). The extended area of heavier rainfall east

of Taiwan is located in the wake of the island where the deflected southerly flow meets with the southwesterly flow rounding northern Taiwan.

Figure 4.5 presents maps of diurnal rainfall (every 3 h) and surface flow patterns (every 6 h) during UNDIST. To get these diurnal patterns, rainfall and flow fields are composited by averaging the time series of data as a function of time of day (local time; LT) over the extent of UNDIST (i.e., yielding 8 distinct patterns for a time series with 8 samples per day). Surface flow is displayed in diurnal-anomaly form by subtracting the time series mean (i.e., the pattern in Fig. 4.4) from the diurnally composited (or diurnal-average) flow patterns. Though this method for deriving diurnal-anomaly patterns is effective with flow fields, the non-Gaussian nature of rainfall (in space) results in sporadic anomaly patterns. A much longer time series of rainfall might alleviate this issue. Still, comparisons between diurnal-anomaly flows (and other fields) and diurnal-average rainfall patterns reveal physically coherent relationships, as will be demonstrated below.

At 02LT the flow around eastern China and western Taiwan is downslope and offshore, with a region of marked convergence in the Taiwan Strait. Note that offshore flows from western Taiwan are stronger than those from China. A small region of rainfall is indicated in the northwestern corner of the QPESUMS domain (i.e., the central Taiwan Strait), which is coincident with enhanced convergence. There is also convergence associated with locally enhanced rainfall where predominant easterly flow meets downslope/offshore flow and diverts around eastern Taiwan. This split flow pattern is associated with a northerly barrier jet near southeastern Taiwan, which has been observed in other years during the Mei-yu season (though the timing is slightly different in other

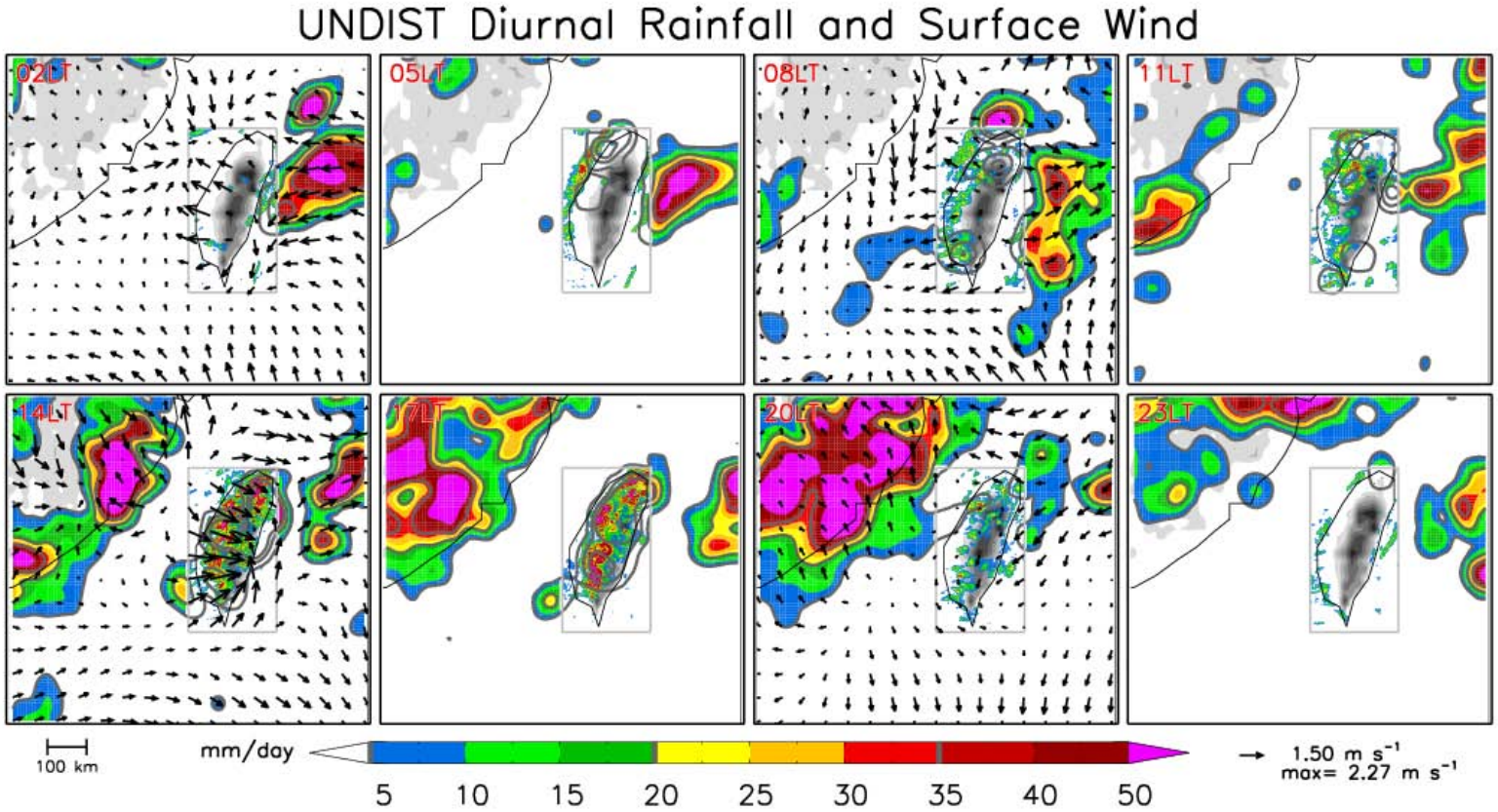

Fig. 4.5. Diurnal-anomaly surface winds (reference vector and maximum value displayed at bottom-right; m s^{-1}) and diurnal-averaged rainfall patterns during UNDIST from TRMM (shaded according to color bar surrounding QPESUMS domain, contoured according to gray ticks in color bar within QPESUMS domain; mm day^{-1}) and QPESUMS rainfall (shaded according to color bar; mm day^{-1}). Local time (LT) is indicated in the upper-left of each panel. Gray boxes outline QPESUMS domain. Terrain is gray-shaded in ~440-m increments. Horizontal distance scale is provided at bottom-left. Rainfall products are available every 3 h, though REANAL is only available every 6 h during UNDIST.

years; Kerns et al. 2010). Since surface radiative cooling should be in full force at 02LT, it is likely that the offshore flows are gravity currents generated by nighttime cooling of the land adjacent to the thermally sluggish water bodies of the Taiwan Strait and Pacific Ocean (i.e., land breezes). Further, radiative cooling in the elevated terrain regions is likely causing acceleration of drainage flows (or mountain breezes).

Note the presence of a well-defined coastal rainband along the northwestern Taiwan coast by 05LT (approximate time of sunrise). The area of rainfall east of Taiwan has persisted, though it is shifted slightly farther offshore. By 08LT, showers extend from the coastal feature in the Taiwan Strait into the coastal plains in Taiwan, though downslope/offshore flows persist. The area of rainfall east of Taiwan has weakened slightly and become more linear, and the flow there has switched to west-southwesterly. A similar offshore-propagating area of convection from southern China has been documented (Aves and Johnson 2008), which has similar timing (i.e., initiation/offshore propagation around sunrise), though the underlying mechanisms have yet to be established. The offshore extent of the area of westerly flow and rainfall east of Taiwan at 08LT suggests that the local LSB/MV circulation is not responsible for its maintenance. The north–south length of the area of westerly flow appears to match the length of the major axis of Taiwan (and the CMR), suggesting that it may be related to dynamics of the orographically modified flow.

By 11LT, rainfall has extended farther into the coastal plains and mountains in Taiwan from the Taiwan Strait, while the area of rainfall east of Taiwan has dissipated further and moved eastward (though with an area of rain extending back to the coast). Coastal rainfall has begun to develop along the coast of southeastern China. By 14LT,

upslope flows are apparent in both Taiwan and eastern China (though stronger in the former) in association with appreciable convergence in the high peaks in both countries (with divergence now predominating in the offshore areas). Accordingly, rainfall has dramatically intensified along the sloping terrain in Taiwan and China. Rainfall in Taiwan appears to be maximized along the upwind slopes as opposed to over the high peaks (consistent with Johnson and Bresch 1991 and Fig. 4.4).

Rainfall coverage maximizes in Taiwan at 17LT [consistent with Johnson and Bresch (1991) and Kerns et al. (2010)]. Though it is tempting to assume that the daytime-regime LSB/MV circulation are at their strongest at this time, Kerns et al. (2010) demonstrate that convergence averaged over Taiwan (a reflection of the strength of LSB/MV circulations) maximizes slightly earlier (12~14LT). This is likely a result of transition from convective rainfall (characterized by intense, showery rainfall) to a stratiform rainfall regime (characterized by greater rainfall coverage). This transition was noted during TAMEX (Johnson and Bresch 1991). Surface flows in Taiwan and eastern China substantially weaken by 20LT, reflecting initiation of land-surface cooling (sunset is at ~18:30LT). Consistent with the slope flow reversal, inland rainfall in Taiwan is severely reduced in coverage and intensity. Interestingly, rainfall in eastern China maximizes later (20LT) than in Taiwan. This delayed rainfall maximum is likely related to daytime eastward-propagation of rainfall systems from the eastern Tibetan Plateau region (Wang et al. 2004; Bao et al. 2011). Another possibility, however, is that rainfall is enhanced at 20LT in eastern China in association with the ascending branch of the planetary-scale LSB-type circulation between eastern China and the northern West Pacific (Huang et al. 2010). This planetary-scale circulation, which is most pronounced in

the summer months, results from the coupling between the LSB in eastern China forced by local, non-migrating thermodynamics and the global, migrating diurnal pressure tide (Huang et al. 2010). Easterly flow can in fact be noted north and east of Taiwan at 20LT (Fig. 4.5), consistent with a transverse circulation in which the ascending branch is to the west. In association with enhanced easterly flow east of Taiwan, the easterly blocked pattern evident at 02LT has begun to develop. By 23LT, rainfall has finally subsided completely over most of Taiwan (and eastern China), and coastal features in rainfall have appeared surrounding Taiwan, suggesting the initiation of downslope/offshore flows.

Another interesting feature depicted in Fig. 4.5 is the apparent surface flow reversal south of Taiwan over the course of the day. Though the planetary-scale LSB-type circulation might explain some of the zonal diurnal wind change north and east of Taiwan (Huang et al. 2010), it does not explain the variation farther south in the SCS, which exhibits notable changes in v (southerly in the morning, northerly in the evening). Another possible explanation for the observed wind reversal is the diurnally varying global Hadley circulation (Dai and Deser 1999; Gille et al. 2003). Gille et al. (2003) show using QuikSCAT data that in the subtropics of both hemispheres there is day-to-night reversal in the surface wind anomalies in response to diurnal pulsing of convection in the Intertropical Convergence Zone. Overall, diurnal rainfall patterns (Fig. 4.5) closely match the mean rainfall patterns during UNDIST (Fig. 4.4), suggesting that diurnal variability is an important controller on rainfall during undisturbed periods. Though there is evidence of surface flow rotation away from land areas (e.g., south, east, and north of Taiwan) that may be related to remote forcing, this signal is substantially weaker than the local surface

LSB/MV flows in Taiwan and coastal China (Fig. 4.5), suggesting that the latter are more important when daytime heating is strong (Fig. 4.3).

ii). Vertical circulations and heating

In order to better understand the structure of rainfall systems and their relation to the diurnal cycle during UNDIST, we next analyze fields along a cross section that cuts through the previously discussed areas of rainfall in eastern China, the Taiwan Strait, the western slopes in Taiwan, and the west Pacific east of Taiwan (Figs. 4.4 and 4.5). To attain an accurate sample of features along this cross section, the main transect, which corresponds with the major axis of the box in Fig. 4.4, is averaged across the minor axis of the box. First provided are UNDIST mean fields along this cross section (Fig. 4.6). Displayed are UNDIST mean Q_1, h_s, and flow component in the plane of the cross section. UNDIST mean QPESUMS and TRMM rainfall along the transect are also displayed.

According to Fig. 4.6, the prevailing flow is westerly (we will denote the left side of the cross section west and the right east for simplicity), and the middle troposphere is conditionally neutral. The lower troposphere is conditionally unstable everywhere, and while the upper troposphere/lower stratosphere is markedly stable (above 200 hPa). Free-tropospheric h_s slightly increases eastward (implying that tropospheric T also increases eastward), which is likely related to the warmer sea surface in the Pacific east of Taiwan (e.g., Fig. 1 from Johnson and Ciesielski 2002). Ascent and apparent heating are present over the central Taiwan Strait throughout most of the troposphere. This area appears to

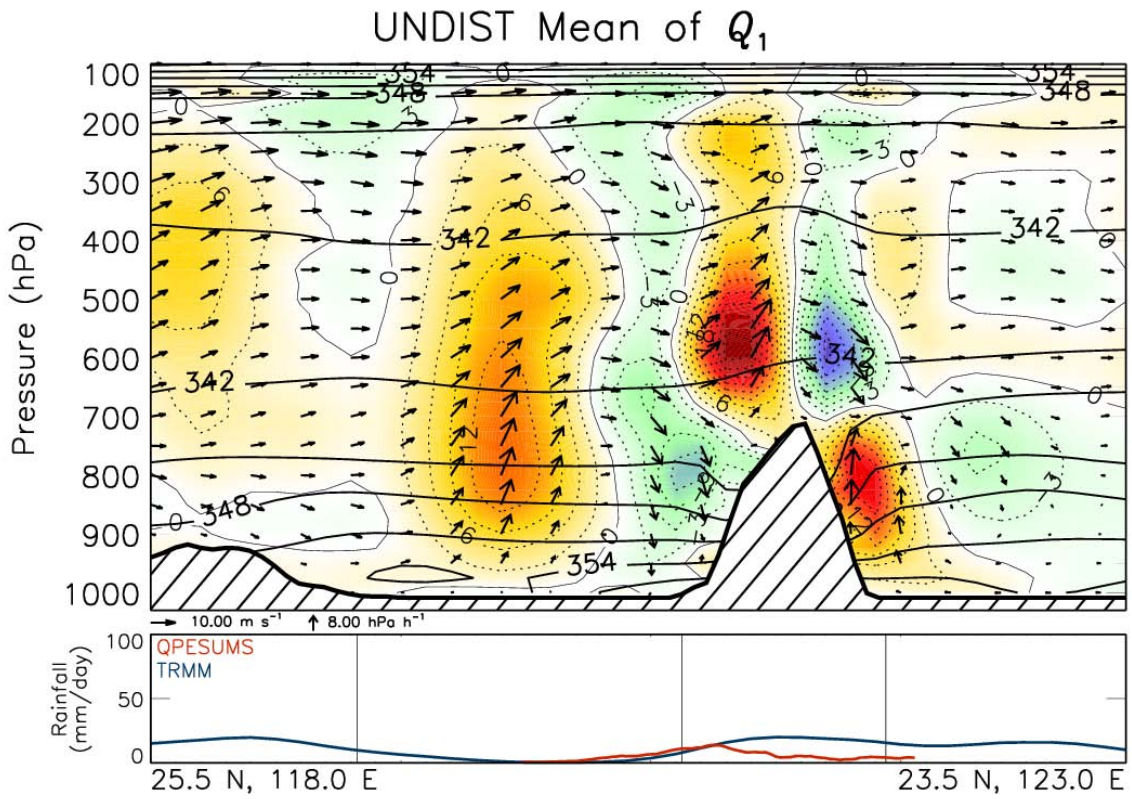

Fig. 4.6. Cross section from 25.5°N 118°E to 23.5°N 123°E (cf. Fig. 4.4). Top: Q_1 is shaded and contoured (thin-solid for zero contour and thin-dotted for other contours; K day^{-1}), flow component in the plane of the cross section (references at bottom-left; m s^{-1}, hPa day^{-1}), saturated moist static energy h_s is contoured (thick-solid contours; kJ kg^{-1}), and topography is hatched. Bottom: rainfall from TRMM (blue) and QPESUMS (red) (mm day^{-1}). Locations of coastlines are marked by vertical bars in bottom panel.

match well with surface confluence northwest of Taiwan where the accelerated and deflected southerly flow meets west-southwesterly flow in the Taiwan Strait (Fig. 4.4). Though the placement is slightly off, it may be related to the enhanced coastal rainfall near northwestern Taiwan (which is most intense around 05LT; Figs. 4.4 and 4.5).

There is a deep couplet in ω and Q_1 above Taiwan from the upper troposphere down to nearly 700 hPa, which matches well with the sloped terrain in Taiwan (Fig. 4.6). This couplet is characterized by pronounced rising motion and heating on the upwind side of the high terrain (accompanied by enhanced rainfall), with sinking motion and cooling on the downwind side (accompanied by reduced rainfall according to

QPESUMS). That the rising motion and heating on the upwind side of the terrain is more vigorous than the sinking and cooling on the downwind side is consistent with net removal of tropospheric water vapor via precipitation (i.e., a pseudo moist-adiabatic process). Cooling and sinking motion in the lower troposphere along the upwind slope is likely related to lower-tropospheric divergence associated with the split flow pattern and northward acceleration in the barrier jet at the surface (Fig. 4.4), whereas shallow heating and rising motion on the eastern side is related to convergence where return-flow in the island wake is forced upslope (there is rainfall on the leeward slope located slightly north relative to this transect; Fig. 4.4).

Figure 4.7 provides cross sections of diurnal Q_1, h_s, (U_{cross},ω) vectors, and rainfall during UNDIST at 02 (a), 08 (b), 14 (c), and 20LT (d). Q_1 and flow fields are in diurnal-anomaly form, while h_s and rainfall are in diurnal-average form. At 02LT (Fig, 4.7a), areas of rising and sinking motion are generally consistent with nighttime LSB/MV circulations, with deep sinking motion and suppressed rainfall over Taiwan and eastern China. The deep column of sinking (rising) motion and cooling (heating) over Taiwan (the western Pacific) is consistent with a thermally direct circulation coupled with moist convection (with attendant rainfall), which is related to low-level convergence of offshore flow from Taiwan and enhanced easterly flow over the western Pacific (Fig. 4.5). Similarly, the vertical column of rising motion and heating in the eastern Taiwan Strait is consistent with convection associated with enhanced convergence at the leading edge of the pronounced nighttime density current extending from western Taiwan (Fig. 4.5). The vertical circulations extending between eastern China and the Taiwan Strait feature upper-level westerly flow and sinking motion in the central Taiwan Strait and very

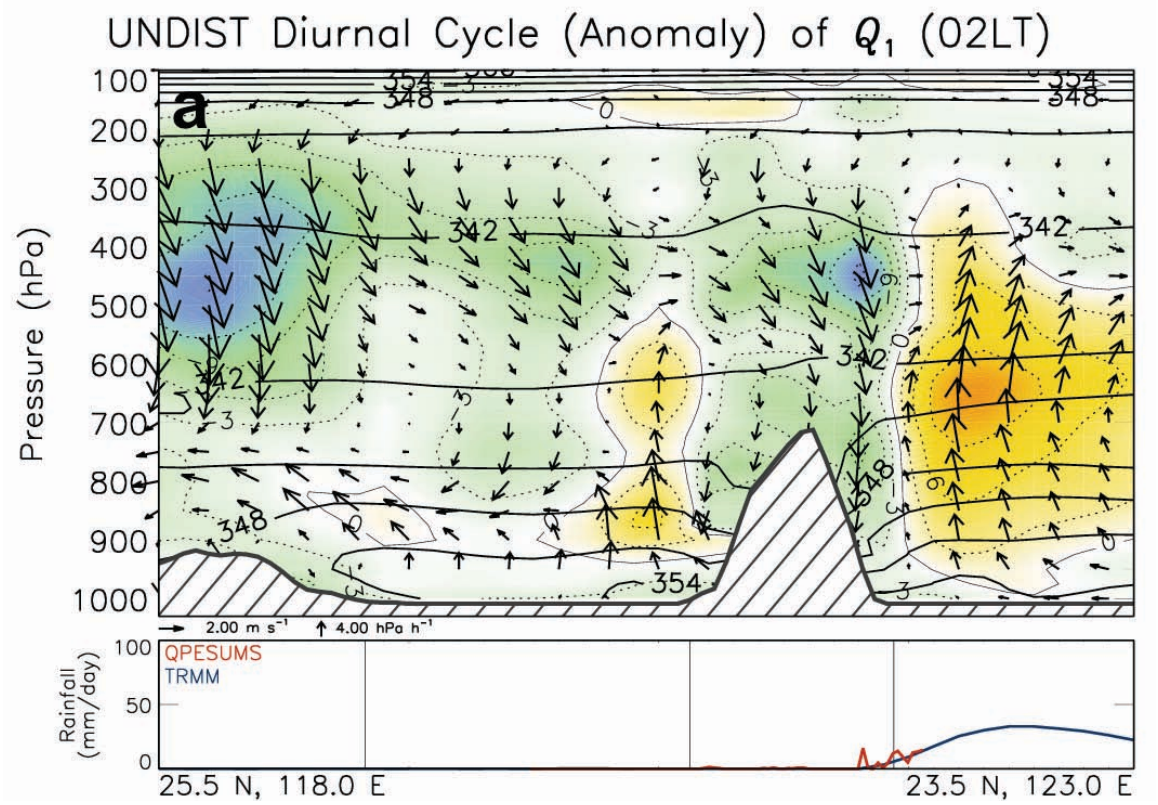

Fig. 4.7(a). As in Fig. 4.6 except in diurnal form for 2 (a), 8 (b), 14 (c), and 20 LT (d). Q_1 and flow fields are in diurnal-anomaly form, while h_s and rainfall are in diurnal-average form. Vector scaling is changed.

shallow rising motion below a layer of easterly flow near 900~800 hPa. It is possible that the deep sinking motion over the Taiwan Strait is related to both the previous day's convection and the column of rising motion and heating in the eastern Taiwan Strait, whereas the shallow easterly flow is return flow above the nighttime land-breeze extending from China.

By 08LT (Fig. 4.7b), sinking motion and cooling above the land areas have weakened, and evidence of low-level daytime heating is present along the east-facing slopes of Taiwan and China (consistent with sunrise around 05LT). In contrast to 3 h earlier, deep rising motion and heating predominate over the Taiwan Strait. The patterns in rainfall suggest that the offshore extent of this area of ascending motion and heating is

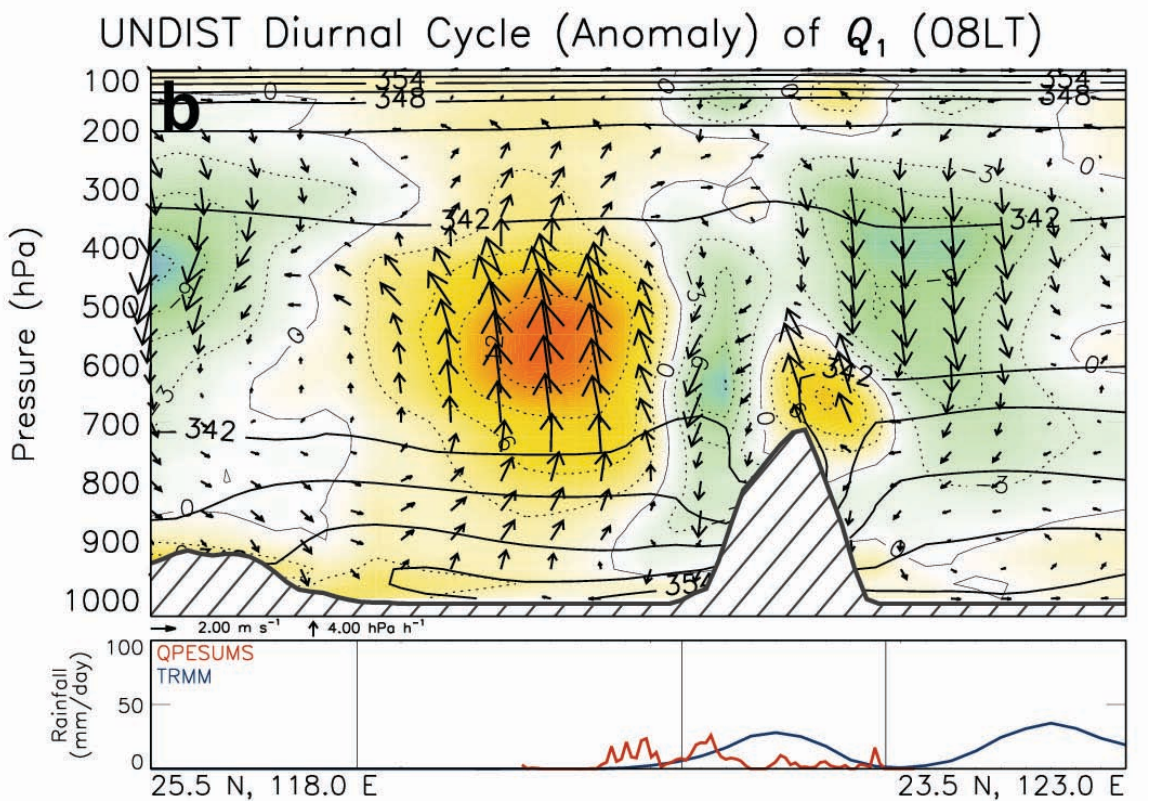

Fig. 4.7(b).

overestimated, which is related to a lack of sounding observations there (Fig. 2.1). The development of the coastal rain feature, which appeared by 05LT (Fig. 4.5), is associated with nighttime surface density currents that have deepened and extended farther offshore along western Taiwan by 08LT (Fig. 4.7b). The development of enhanced rainfall along the lower-western Taiwan slopes and coastal plains suggests that upslope flow and associated heating should be present at some level by this time (in contrast to what is shown). Note that upper-level sinking motion and cooling now predominate immediately east of Taiwan, with suggestion of rising motion, heating, and rainfall farther east (suggesting eastward propagation, as mentioned earlier).

By 14LT (Fig. 4.7c), the daytime-regime LSB/MV circulations are in full swing, with convection evidenced by deep rising motion and heating coincident with heavy rainfall in eastern China and Taiwan. According to QPESUMS, rainfall in Taiwan is focused along the western coastal plains and foothills, which is consistent with the asymmetric pattern in vertical motion and heating across the CMR. That rainfall in TRMM is shifted east in Taiwan relative to QPESUMS is likely a bias introduced by infrared satellite data (i.e., extensive cirrus advected eastward by the westerly flow aloft), which is part of the 3B42 TRMM product employed here (Huffman et al. 2007). Consistent with daytime surface heating, h_s and conditional instability are dramatically increased at low-levels, particularly over land. Convective outflows are evident near the tops of the convective heating columns in China and Taiwan, which are connected to

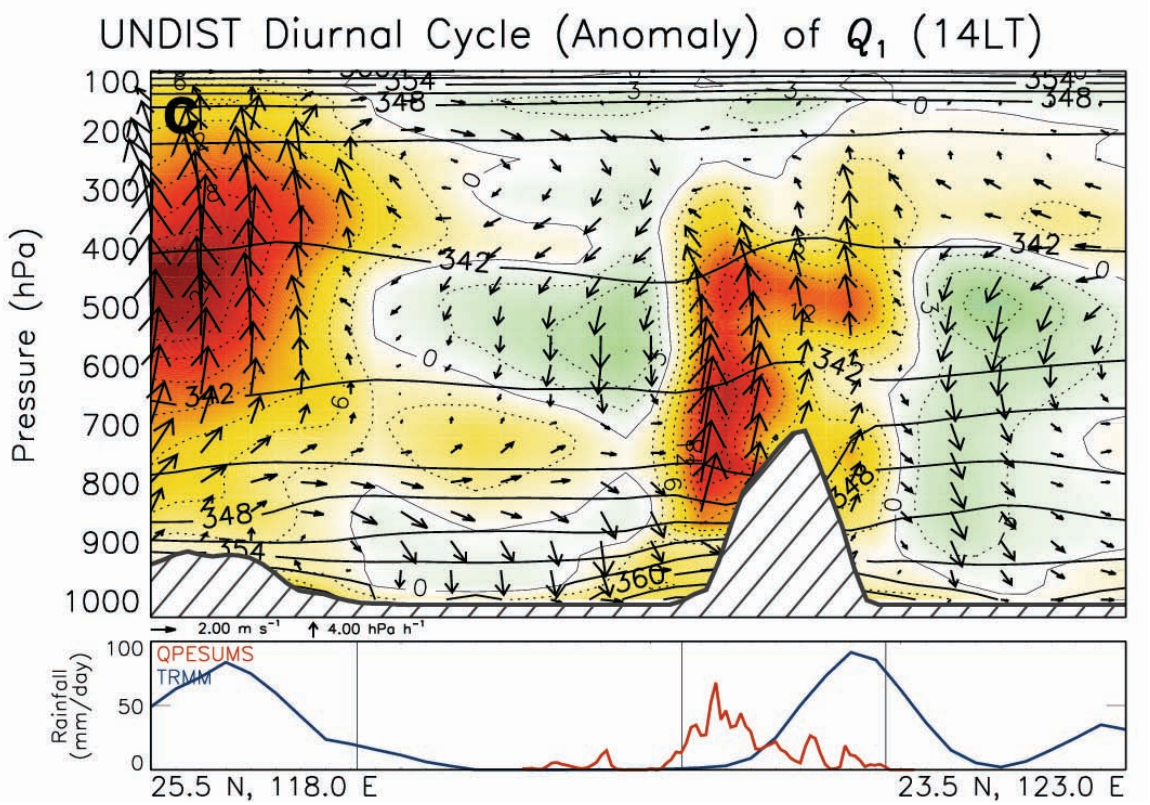

Fig. 4.7(c).

thermally direct vertical circulations. Convective heating and rising motion is maximized in the upper-troposphere in China (e.g., near 450 hPa), which reflects deep convection there, whereas the bottom-heavy convective heating in Taiwan suggests that deep convection is resisted there. Still, some convection extends to greater depths, as suggested by a small maximum in heating over Taiwan near 450 hPa. The shallow overturning circulation extending from eastern China into the Taiwan Strait (similar but opposite to the pattern at 02LT; Fig. 4.7a) might be related to a shallow heating maximum associated with sensible heating from the surface in China, though this is not well resolved in REANAL (Fig. 4.7c). It might also suggest that at certain times deep convection is resisted (e.g., by dry air aloft), though this should also be associated with a shallow maximum in heating and rising motion, which does not appear in Fig. 4.7c. That said, the bottom-heavy heating in Taiwan suggests resistance to deep convection, as mentioned above. In the presence of a dry free-troposphere (as was the case during UNDIST; Fig. 3.3), deep buoyant updrafts are hindered by entrainment of dry air, resulting in shallow- or congestus-type convection (e.g., Johnson et al. 1999). Confirmation of this behavior using TRMM and/or CloudSat radar data (Stephens et al. 2002) would be an interesting exercise.

The pattern at 20LT (Fig. 4.7d) is dramatically different from that at 14LT. Sinking motion and cooling have developed over eastern China, the Taiwan Strait, and Taiwan, with rising motion and warming at upper levels over the Taiwan Strait, Taiwan, and the western Pacific. This pattern, with rainfall persisting along the western Taiwan slopes, reflects an evening transition to stratiform rainfall over a large part of the region (consistent with the findings of Johnson and Bresch 1991). The development of sinking

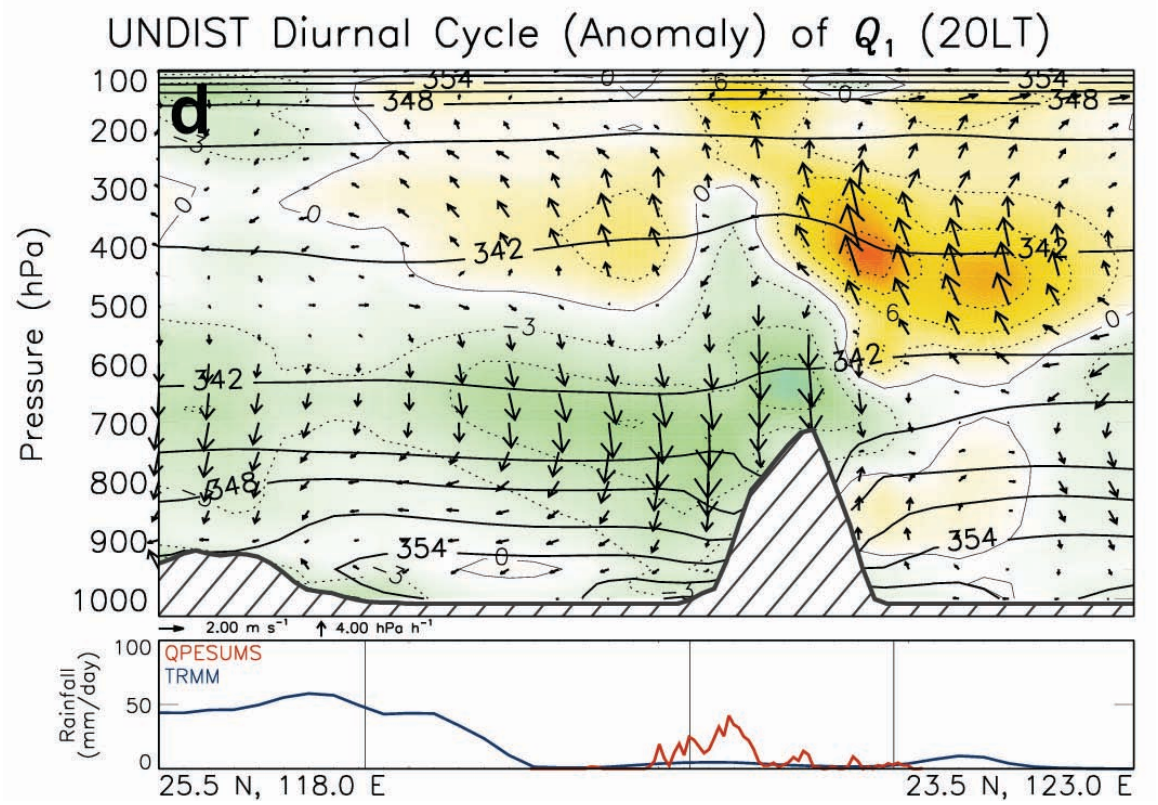

Fig. 4.7(d).

motion and cooling over all land areas is consistent with transition into the nighttime LSB/MV circulation regime, including over the China mainland. The shallow rising motion that has developed in the western Pacific is consistent with the flow reversal (to easterly) far offshore and development of associated convergence along eastern-coastal Taiwan (Fig. 4.5). This pattern corresponds with initiation of the offshore rain feature east of Taiwan, which later begins to propagate eastward.

iii). Vertical profiles from the TiMREX Land Enhanced Sounding Array (ESA)

To provide an enhanced perspective of the diurnal cycle in the Taiwan region, next provided are diurnal profiles of various fields averaged over the TiMREX Land ESA (Fig. 2.1) for UNDIST. First, Fig. 4.8 provides UNDIST mean profiles of *u*, *v*, RH, *h*, *T*, and *q* averaged over the Land ESA, where $h = s + Lq$ is moist static energy. The features at low levels in these profiles are biased by a lack of data (because the pressure surfaces are below ground in the areas of high elevation), and thus mostly reflect data near the

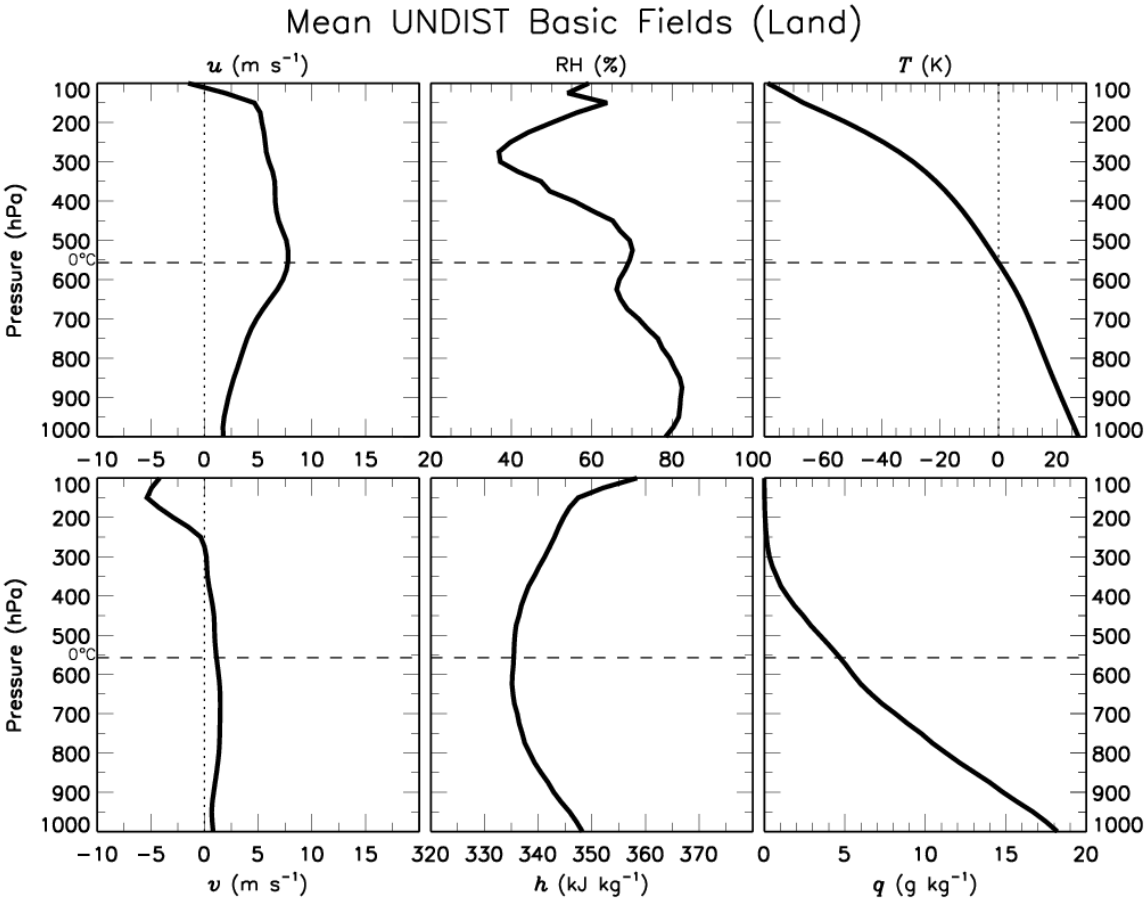

Fig. 4.8. Mean vertical profiles of the basic fields for UNDIST averaged over the TiMREX Land ESA. Top (left–right): *u* (m s^{-1}), RH (with respect to ice where below 0°C; %), and *T* (K). Bottom (left–right): *v* (m s^{-1}), moist static energy *h* (kJ kg^{-1}), and specific humidity *q* (g kg^{-1}). Vertical dotted lines denote zero *x*-values. The horizontal dashed lines denotes the 0°C level.

coastal regions at these levels. As discussed earlier (Figs. 3.3 and 4.6), the flow aloft in Taiwan during UNDIST was predominantly westerly (Fig. 4.8). This is consistent with the 200-hPa pattern displayed in Fig. 3.6. RH is near 80% from 1000~800 hPa, and steadily decreases to below 50 % in the upper troposphere. T and q decrease into the upper troposphere, as expected. The pattern of h reveals that, on average, the environment over Taiwan is convectively unstable at low levels (up to ~700 hPa), relatively neutral from 700~500 hPa, and stable in the upper troposphere and lower stratosphere.

Figure 4.9 is the same as Fig. 4.8 except with δ, ω, h_s, Q_1, Q_2, and vertical gradient of h_s plotted versus pressure. In Fig. 4.9, the layer of marked convergence peaking around 600 hPa is likely related to negative buoyancy production by melting beneath the freezing level, as has been documented for other regions of the tropics (Mapes and Houze 1995; Johnson et al. 1996). The relative minimum in vertical gradient of h_s near 600 hPa is consistent with this notion (Johnson et al. 1996). Consistent with Figs. 3.3 and 4.6, the troposphere is conditionally unstable from 1000~700 hPa, roughly neutral from 700~200 hPa, and markedly stable in the upper troposphere/lower stratosphere.

Figure 4.9 mostly reflects the patterns displayed over western Taiwan in Fig. 4.6: strong rising motion, heating, and drying in the upper troposphere and sinking motion, cooling, and moistening at lower levels. As described earlier, the latter is likely related to flow blocking by the topography in western Taiwan (Fig. 4.6). The confinement of rainfall along the downwind slopes to the northern areas of Taiwan (Fig. 4.4) suggests that enhanced shallow rising motion is also confined to this area, while the topographic

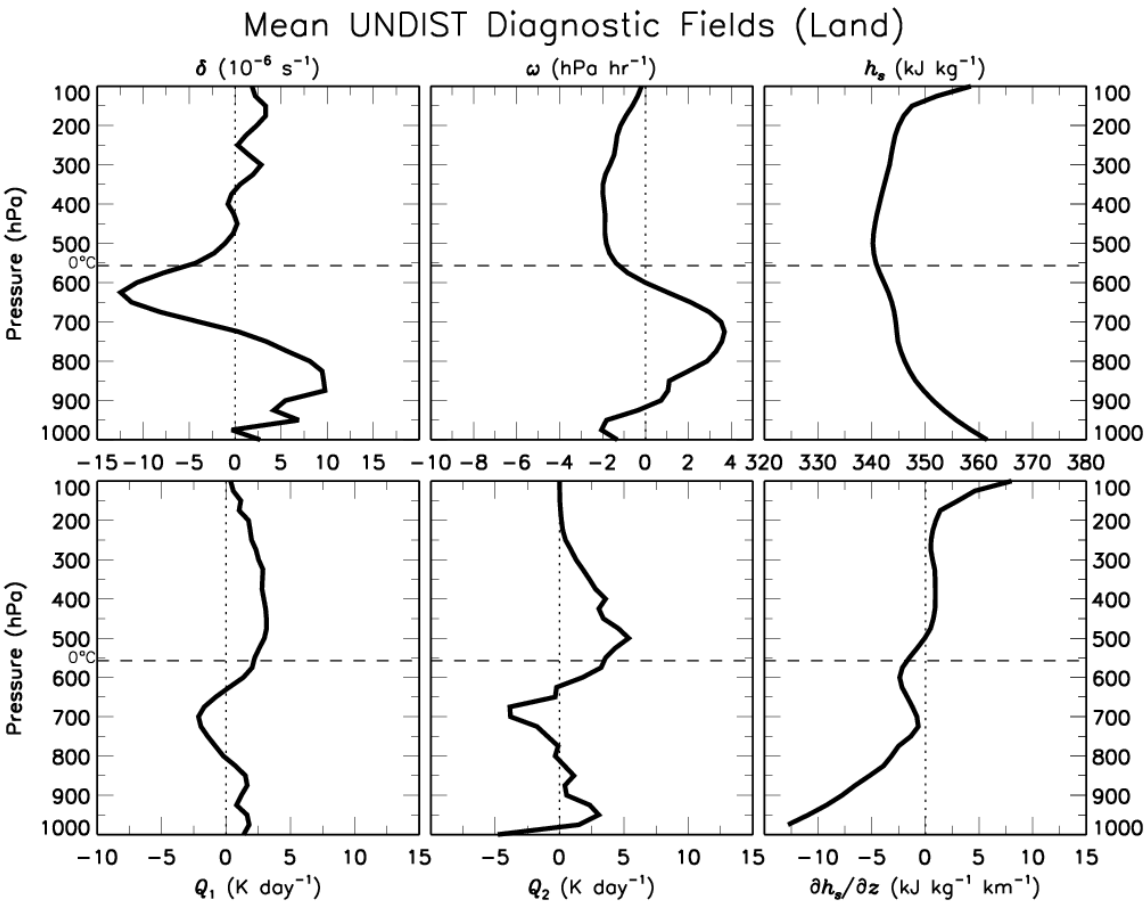

Fig. 4.9. As in Fig. 4.8 except for the diagnostic fields. Top (left–right): δ (10^{-6} s^{-1}), ω (hPa hr^{-1}), and h_s (kJ kg^{-1}). Bottom: Q_1 (K day^{-1}), Q_2 (K day^{-1}), and vertical gradient of h_s (kJ kg^{-1} km^{-1}).

blocking in western Taiwan and associated low-level divergence likely extends over a larger area (Fig. 4.4). This would explain why there is some discrepancy between Figs. 4.6 and 4.9. Still, the patterns in the mean (i.e., Figs. 4.6 and 4.9) also include the total effects of the diurnal cycle, which are discussed next.

Figure 4.10 presents diurnal time series (generated with 4 day^{-1} data) of *u*, *v*, RH, *T*, and *q* versus pressure for UNDIST, averaged over the Land ESA. RH is displayed in both diurnal-anomaly and diurnal-average form, while the other fields are all in diurnal-anomaly form. The diurnal oscillations in low-level (800~1000-hPa) *u´* are consistent

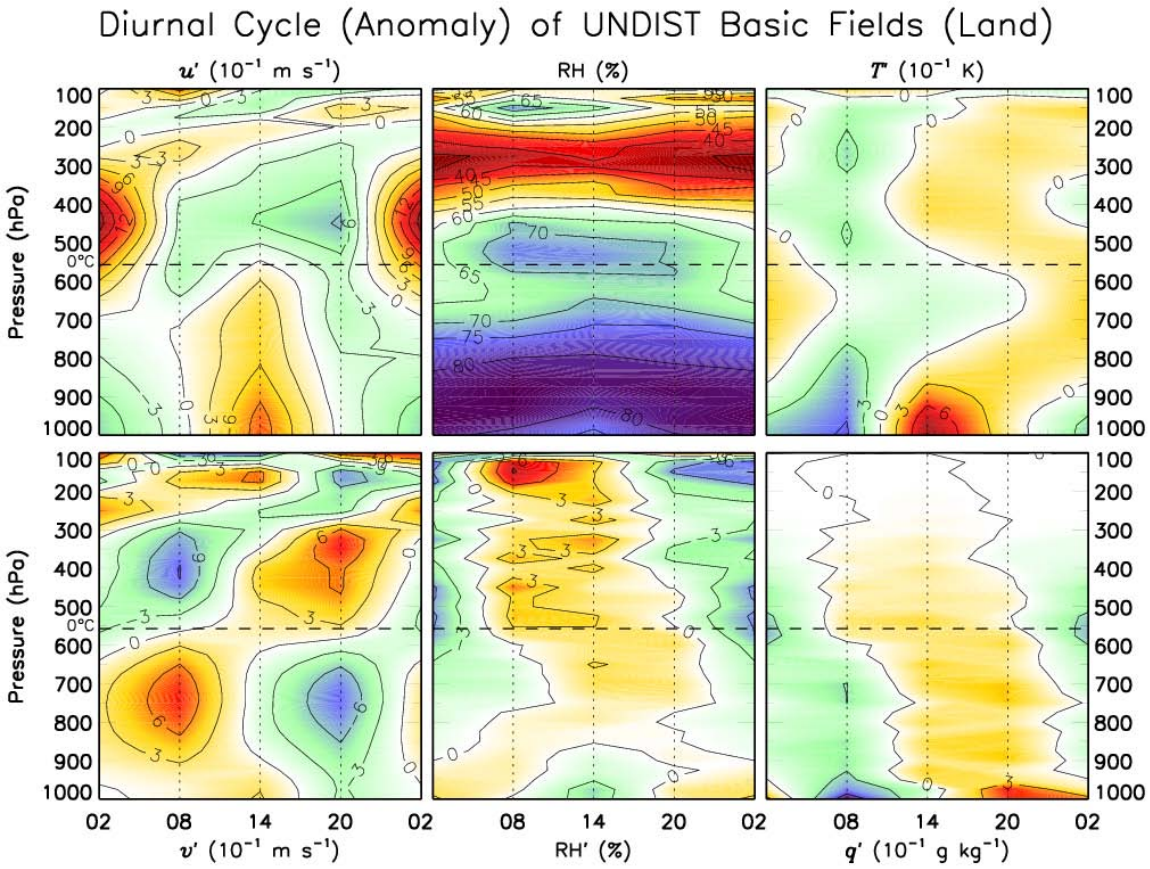

Fig. 4.10. As in Fig. 4.8 except fields are in diurnal form, and *x*-axis is LT (from 2–20LT, with the 2LT pattern repeated at the end). *u*, *v*, *T*, and *q* are in diurnal-anomaly form. RH is displayed in both diurnal-average (top-middle) and diurnal-anomaly (bottom-middle) form, the latter of which replaces *h* from Fig 4.8.

with the LSB/MV circulation, with onshore/upslope flow ($u'>0$) maximizing at 14LT. That the low-level wind reversal in Taiwan is related to the buoyancy-driven LSB/MV circulation is consistent with the marked correlation between low-level T' and u'. Low-level RH′ appears to be coupled to the diurnal evolution of T', which, during the afternoon, is likely related to both downward mixing of dry air from aloft and increased saturation vapor pressure with daytime heating. RH′ in the middle and upper troposphere, however, correlates well with q'. The increase in low- to mid-level q' around 14LT is

related to positive u' (i.e., moisture advection by the sea breeze), which extends all the way up to the freezing level at 14LT.

Figure 4.11 is the same as Fig. 4.9, except in diurnal form (as in Fig. 4.10), with δ, ω, Q_1, Q_2, and vertical gradient of h_s expressed in diurnal-anomaly form. h_s is also displayed in diurnal-average form with diurnal-average vertical gradient of h_s overlaid. The coincidence of lower-tropospheric upward motion, apparent heating and drying, and maximized low-level conditional instability clearly demonstrates the peak in moist convection at 14LT over Taiwan (consistent with Figs. 4.5 and 4.7c). Similar to Fig. 4.7c, the primary 14LT convection maximizes in the lower-troposphere, while upper-level

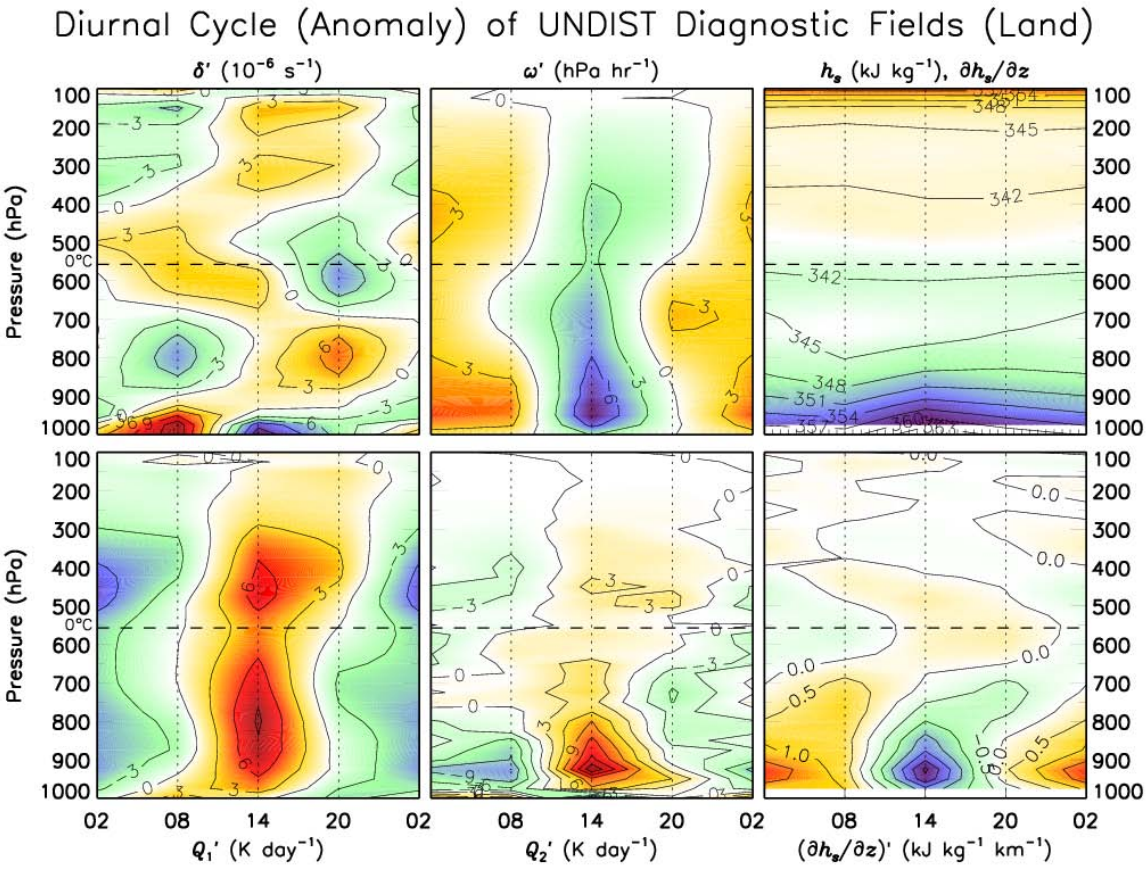

Fig. 4.11. As in Fig. 4.9 except fields are in diurnal form, and x-axis is LT (as in Fig. 4.10). δ, ω, Q_1, Q_2, and vertical gradient of h_s are in diurnal-anomaly form, while h_s is left in diurnal-average form (with diurnal-average vertical gradient of h_s shaded; top-right).

peaks in divergence, upward motion, and heating demonstrate that some deep convection is also present. Important to note, however, is that lower-tropospheric maxima in Q_1 heating and Q_2 drying around the time of peak T' (14LT) are in part related to the vertical eddy heat/moisture flux divergence terms (Eqs. (2) and (3)), which might be significant up to ~850 hPa where the boundary layer deepens to (according to lower-tropospheric T'). The predominance of vertical patterns in divergence near and below the freezing level demonstrates the prevalence of shallow circulations, consistent with bottom-heavy convection. In contrast to 14LT, the pattern at 20LT exhibits upper-tropospheric ascent, warming, and drying above lower–middle-tropospheric sinking, cooling, and moistening, demonstrating the transition to a stratiform-rainfall regime in which downdrafts enhanced by evaporation and melting predominate in the lower–middle-troposphere. Following 20LT, the pattern becomes downdraft-dominated as low-level cooling and stabilization (in h_s) set in. This diurnal evolution is encouragingly consistent with Figs. 4.5 and 4.7a–d, as well as the diurnal cycle described for an undisturbed period during TAMEX (Johnson and Bresch 1991).

An interesting feature in the above plots is the relationship between inferred convection (Fig. 4.11) and T' (Fig. 4.10). Low-level T' peaks at 14LT in relation to the cumulative effect of daytime insolation. At the same time, there is positive T' throughout the upper troposphere, which likely relates to the upper-level diabatic convective heating. Note the lowering (raising) of the upper- (lower-) tropospheric positive anomaly with time into the late afternoon, creating an “elbow” shape. This evolution in tropospheric T, as well as the evolution from deep convection (albeit hindered) to stratiform rain later in

the day, is a reflection of the "self-similar" nature of tropical rainfall systems across spatial and temporal scales (Kiladis et al. 2009).

4.2 Diurnal cycle during DIST (1–6 June 2008)

As demonstrated by Figs. 4.2 and 4.3, diurnal variance in *T* and U_{NORM} was substantially reduced during the active rainfall period of DIST (or ACTIVE1) in association with reduced insolation (from increased cloudiness). This suggests that the prominent connections between rainfall and the LSB/MV circulations, as those described earlier for UNDIST, should be less pronounced.

i). Surface flows and rainfall

As discussed in Chapter 3, DIST was characterized by heavy rainfall concentrated along a roughly west–east-oriented Mei-yu front marked by significant cyclonic shear (Fig. 3.7). Figure 4.12 provides a map of DIST mean rainfall and surface flow, focused on Taiwan as in Fig. 4.4. (Note that the radar in southern Taiwan has an area of beam-blockage that causes a negative QPESUMS rainfall bias along the southeastern Taiwan coast, which is readily visible in Fig. 4.12.) From this perspective, the cyclonic shear is remarkably clear across the Mei-yu front, which marks the boundary between the northerly surface cold intrusion to the north and summer monsoonal southwesterly flow to the south. As noted by previous studies (Lai et al. 2011; Davis and Lee 2012), DIST rainfall came largely in the form of intense MCSs propagating eastward along the Mei-yu

front, which explains the concentration of heavy rainfall close to the frontal shear line in the northern SCS and southern Taiwan.

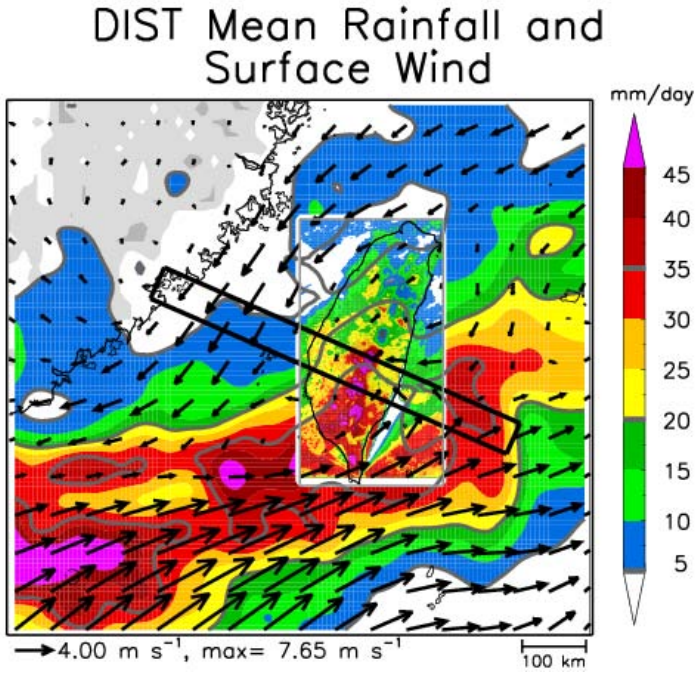

Fig. 4.12. As in Fig. 4.4 except for the period 1–6 June 2008 (hereafter, denoted DIST).

It is apparent from Fig. 4.12 that rainfall during DIST was maximized along the high peaks of the southern CMR (Fig. 1.2), as opposed to the coastal plains and foothills in western Taiwan as during UNDIST (Fig. 4.4). In association with slightly stronger southwesterly monsoon flow during DIST, there was a larger value Fr (~0.5) (as calculated from a DIST mean sounding from south of the Mei-yu frontal rainfall; not shown). Though Fr~0.5 is characteristic of blocked flow (e.g., Li and Chen 1998), this value is not representative of the environments within the Mei-yu frontal MCSs that account for much of the rainfall during this period (Lai et al. 2011; Davis and Lee 2012). In these large MCSs, the environment is generally moist-neutral, suggesting that air parcels are easily perturbed upward by topography (Houze 2011); this suggests that,

during DIST, rainfall intensity is roughly correlated with topography height (Houze 2011). This explains the rainfall maximum over the high peaks of the CMR during DIST (Fig. 4.12).

Figure 4.13 provides maps of diurnal rainfall and flow patterns, as in Fig. 4.5 except for DIST (note the significant change in the rainfall color bar). REANAL is available eight times per day during DIST, which was during the EOP. As in Fig. 4.5, surface flow is in diurnal-anomaly form, with the mean DIST pattern (Fig. 4.12) removed. Considering the measure of mesoscale variability during active periods in the Mei-yu season (associated with MCSs; Chen 2004; Lai et al. 2011; Davis and Lee 2012), the level of day-to-day persistence is greatly reduced. As a result, the diurnal patterns in Fig. 4.13 (and all subsequent figures) must be considered with scrutiny, as they do not represent the mean diurnal cycle with statistical significance (this would require a much larger sample size than one active period). This is in contrast to the undisturbed periods (e.g., UNDIST; Fig. 4.5), which exhibit much more persistence since they are predominately characterized by the very periodic response of the flow to diurnal heating/cooling of the land surface.

Though nighttime/morning offshore and downslope flows and midday/afternoon onshore and upslope flows can still be noted within Taiwan (Fig. 4.13), these patterns (particularly the nighttime patterns) are significantly weaker than those observed during UNDIST (Fig. 4.5). This is consistent with Figs. 4.2 and 4.3. In contrast, the diurnal flows appear to be strong in southeastern China. The lack of rainfall there (which implies decreased cloudiness) suggests that stronger LSB/MV circulations can develop. Further, diurnal variability in China has a component that is remotely forced by eastward

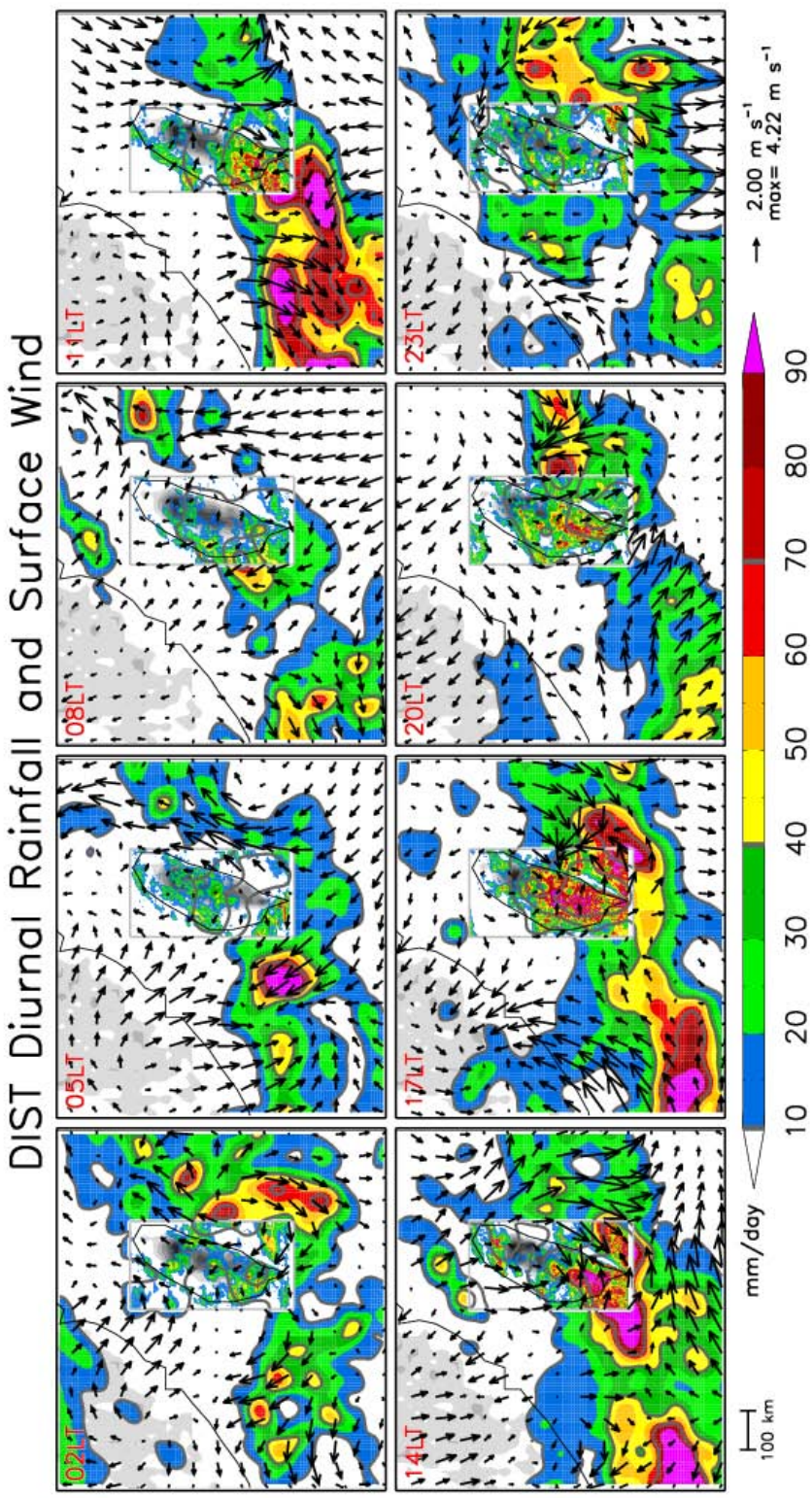

Fig. 4.13. As in Fig. 4.5 except for DIST.

propagating systems from the eastern Tibetan Plateau region (Wang et al. 2004; Bao et al. 2011). Despite reduced diurnal surface flows, diurnal rainfall variability in southern Taiwan is unmistakable: scattered rain showers exist throughout Taiwan during most of the nighttime/morning hours, which give way to widespread heavy rainfall (>50 mm day^{-1}) in the late morning and afternoon hours (Fig. 4.13). The maximum in upslope flow (14LT) slightly precedes coverage of maximum heavy rainfall (17LT) in southern Taiwan. Previous studies have documented this delay of the most intense rainfall over Taiwan (e.g., Kerns et al. 2010), which is likely related to a weakening of the diurnal surface flows as a result of increased cloudiness and development of cold outflows. Eastward propagation of rainfall systems can be noted in Fig. 4.13, though it is unclear whether this related to the diurnal cycle or simply aliasing by the eastward propagation of several strong MCS events during the EOP in the prevailing westerly flow (Fig. 3.3).

ii). Vertical circulations and heating

Figure 4.14 provides a mean cross section of flow, Q_1, rainfall, and h_s for DIST, as in Fig. 4.6 except along the cross section shown in Fig. 4.12. Qualitatively, Figs. 4.6 and 4.14 are similar: with shallow sinking motion and cooling along the western slope (weaker in Fig. 4.14); shallow rising motion and heating along the eastern slope (stronger in Fig. 4.14); strong middle-tropospheric rising motion and heating (stronger in Fig. 4.14); and middle-tropospheric sinking motion and cooling slightly downstream of the latter (much weaker and smaller region in Fig. 4.14). Also similar to Fig. 4.6, rainfall is reduced along the eastern slope in Fig. 4.14 (according to QPESUMS), consistent with

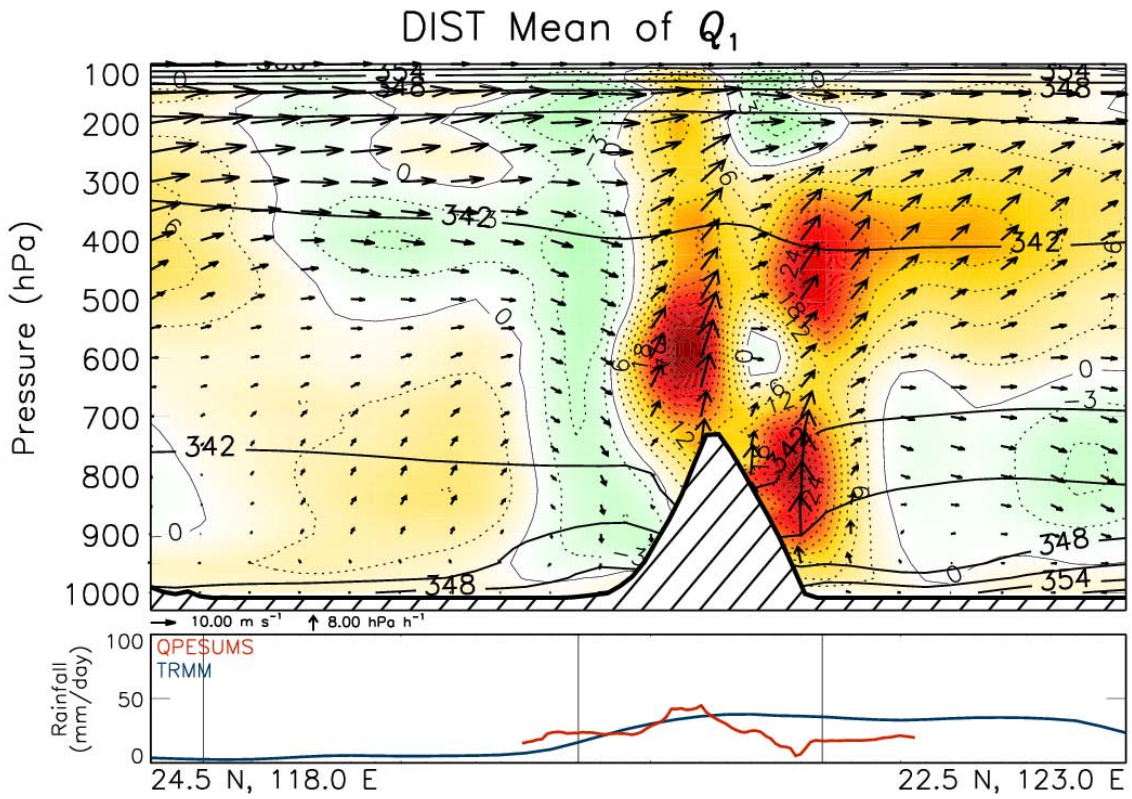

Fig. 4.14. As in Fig. 4.6 except for DIST and along the cross section shown in Fig. 4.12.

the expulsion of water vapor through precipitation upstream of the downwind slope. That rising motion generally predominates over Taiwan in Fig. 4.14 is consistent with a more convective, updraft-dominated environment during DIST (Fig. 3.4). Different from Fig. 4.6, a strong upper-tropospheric maximum in rising motion and heating exists (centered near 450 hPa), which extends eastward into the western Pacific. With weak sinking motion and cooling in the lower tropospheric below this region of warming (east of Taiwan), this resembles a stratiform rainfall pattern. This pattern is likely related to a transition of rainfall systems to stratiform rain as they propagate eastward off of Taiwan along the Mei-yu front.

Figure 4.15 provides diurnal cross sections of the fields shown in Fig. 4.14, as in Fig. 4.7 (at 02, 08, 14, and 20LT). Recall from earlier that there is a narrow band along the east coast of Taiwan where, due to radar beam-blockage, QPESUMS rainfall is negatively biased (this bias is readily visible in Fig. 4.12). In general, some of the diurnal signatures present during UNDIST (Fig. 4.7) are present during DIST (Fig. 4.15). For instance, sinking motion and cooling generally predominate over Taiwan during the nighttime/morning hours (e.g., at 02, 08, and 20LT). Rising motion and heating are unmistakable at 14LT (Fig. 4.15c) over Taiwan, and even over the Taiwan Strait, suggesting vigorous deep convection (particularly over eastern Taiwan, where heating and upward motion are deep). Rainfall, according to QPESUMS, is highest over Taiwan at 14 and 20LT.

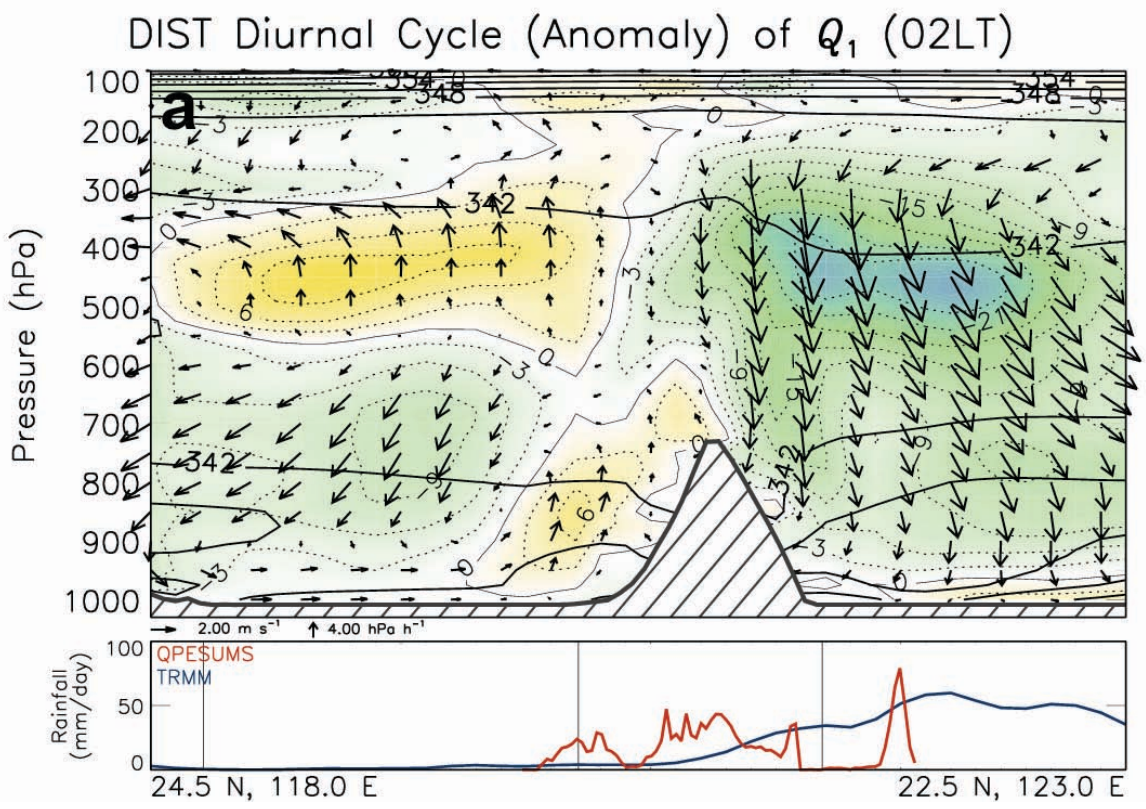

Fig. 4.15(a).

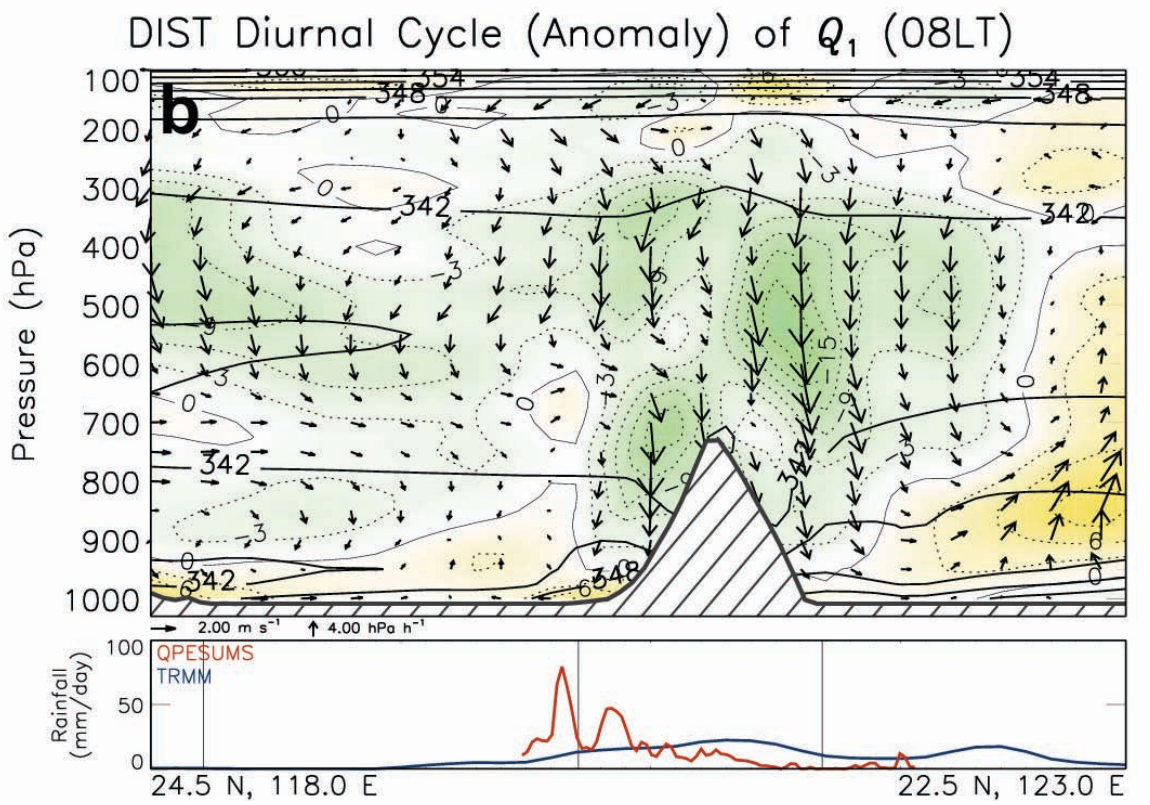

Fig. 4.15(b).

Caution is necessary when examining Fig. 4.15. Though not shown, DIST was characterized by several eastward-propagating MCSs focused along the Mei-yu front (similar to other Mei-yu front cases; e.g., Chen et al. 2008). Such mesoscale variability has impacts on the representativeness of these diurnal-composite figures that must be considered: 1) since the GFS used as background for REANAL likely struggles to accurately forecast MCSs (both in placement and intensity), these inaccuracies are inevitably included in REANAL; 2) forecast inaccuracies aside, the timing of propagating MCSs across the region sampled in Fig. 4.15 might be aliasing onto the diurnal cycle. In the future, the forecast skill of the GFS during this period will be assessed. Further, the impact of removing intense MCS events from the DIST time series will be determined.

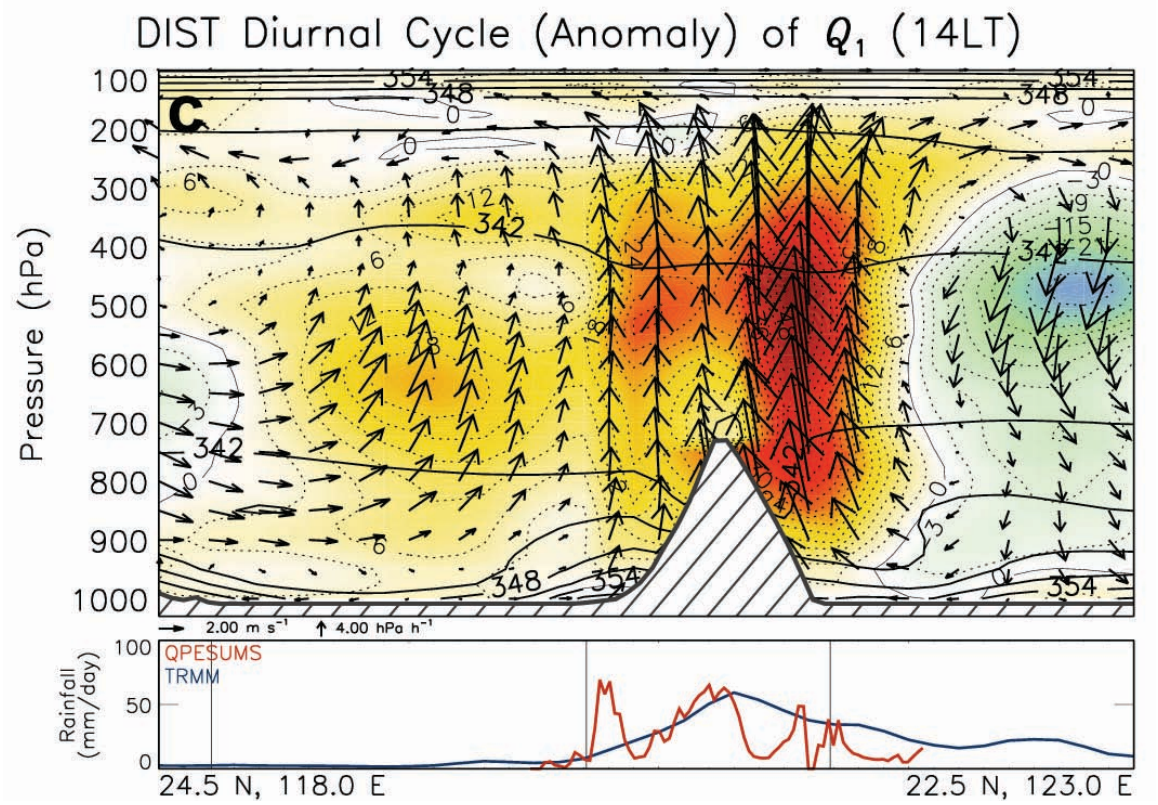
DIST Diurnal Cycle (Anomaly) of Q_1 (14LT)
Pressure (hPa)
100
200
300
400
500
600
700
800
900
1000
C
354
348
342
2.00 m s^{-1}
4.00 hPa h^{-1}
Rainfall (mm/day)
QPESUMS
TRMM
24.5 N, 118.0 E
22.5 N, 123.0 E

Fig. 4.15(c).

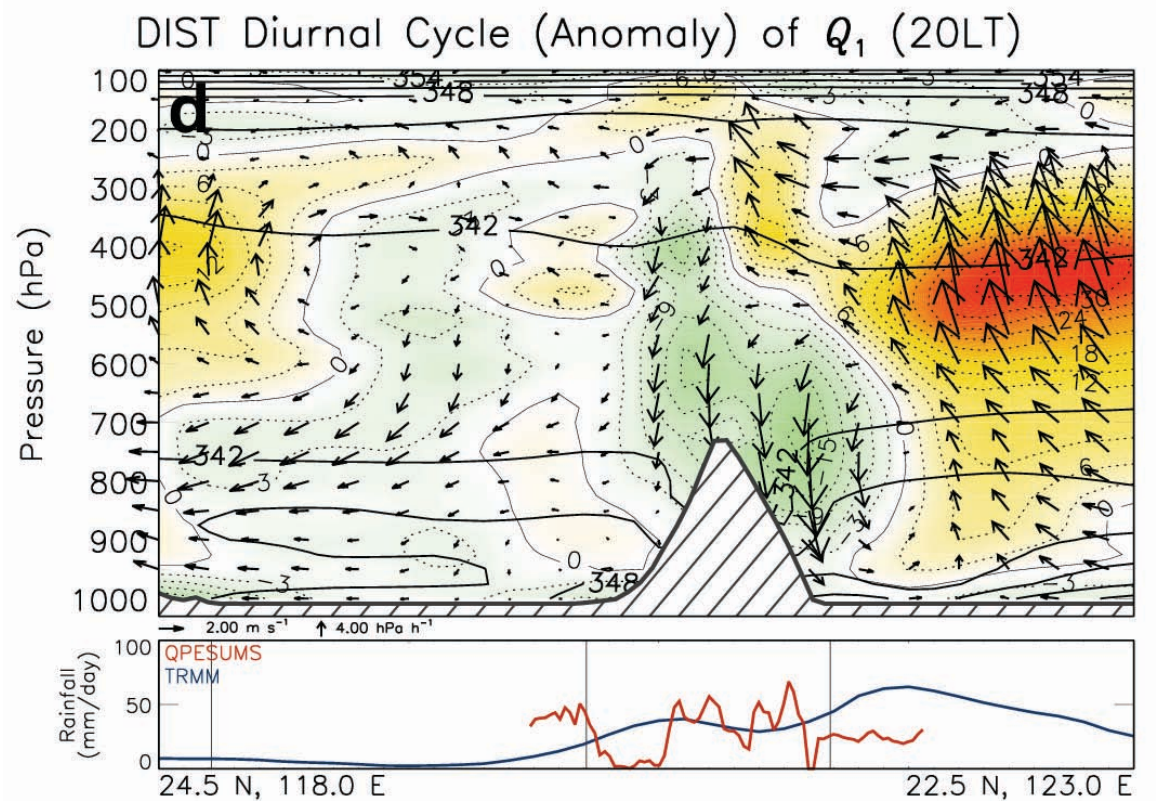

Fig. 4.15(d).

iii). Vertical profiles from the TiMREX Land Enhanced Sounding Array (ESA)

Figure 4.16 presents DIST mean profiles of *u*, *v*, RH, *h*, *T*, and *q* averaged over the Land ESA (as in Fig. 4.8). Upper-level zonal flow is ~three times that of UNDIST (Fig. 4.8), and slightly stronger deep southerly flow can also be noted. This is consistent with the presence of a 200-hPa trough with axis positioned slightly west of Taiwan (Fig. 3.8). RH throughout the column is substantially greater than that during UNDIST, with values >80% extending into the upper troposphere (consistent with Fig. 3.3). Close comparison of Figs. 4.8 and 4.16 demonstrates that the lower tropospheric convective instability is shallower during DIST, and middle-tropospheric convective stability is

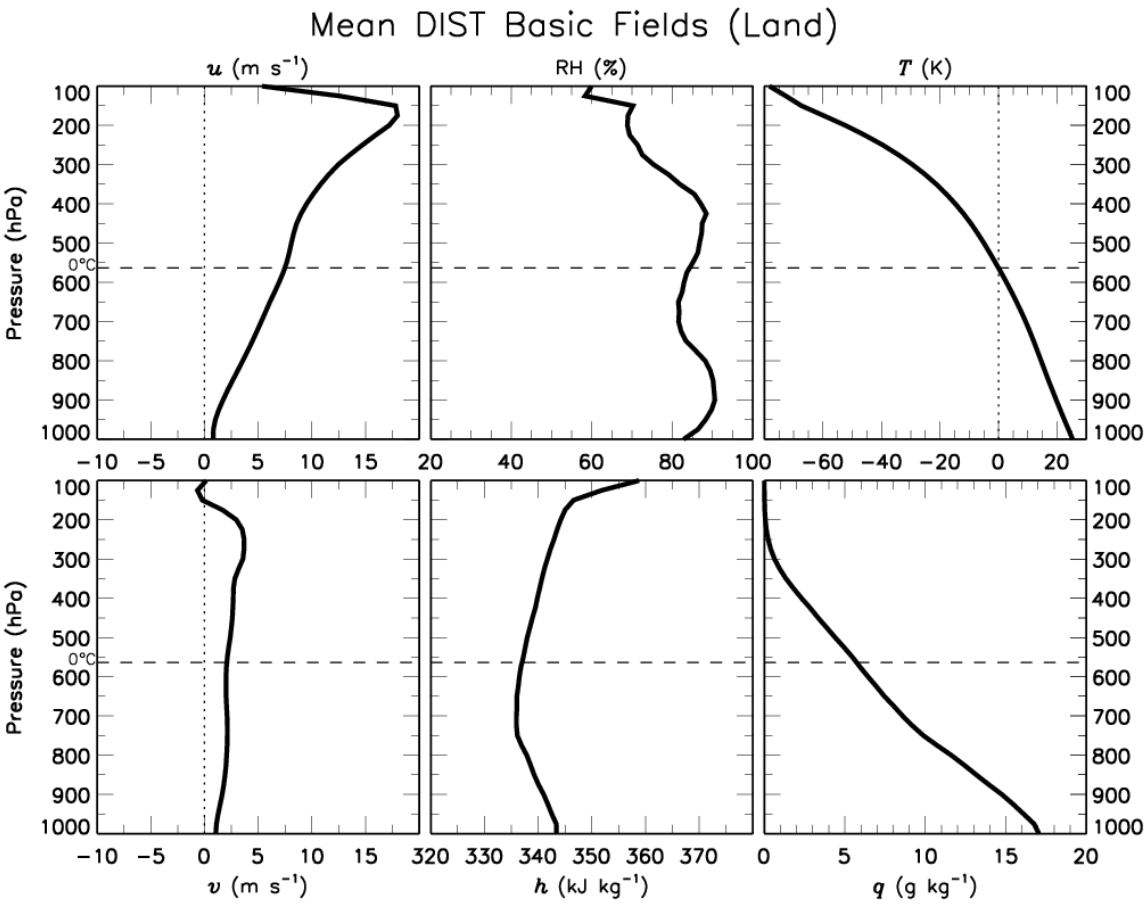

Fig. 4.16. As in Fig. 4.8 except for DIST.

stronger. Figure 4.17 provides DIST mean profiles of δ, ω, h_s, Q_1, Q_2, and vertical gradient of h_s averaged over the Land ESA (as in Fig. 4.9). There is unmistakable deep convection in Fig. 4.17, with deep-tropospheric rising motion (consistent with the profile of δ), apparent heating, and apparent drying. Divergence peaks at 200 hPa, with rising motion peaking near 550~350 hPa. Q_1 peaks near 450 hPa, while Q_2 exhibits two peaks; one around 550~450 hPa and another near 750 hPa. Similar double-peaked structure to Q_2 is commonly observed (Yanai et al. 1973; Johnson and Bresch 1991), and has been attributed by Johnson et al. (1996) to indirect effects of melting.

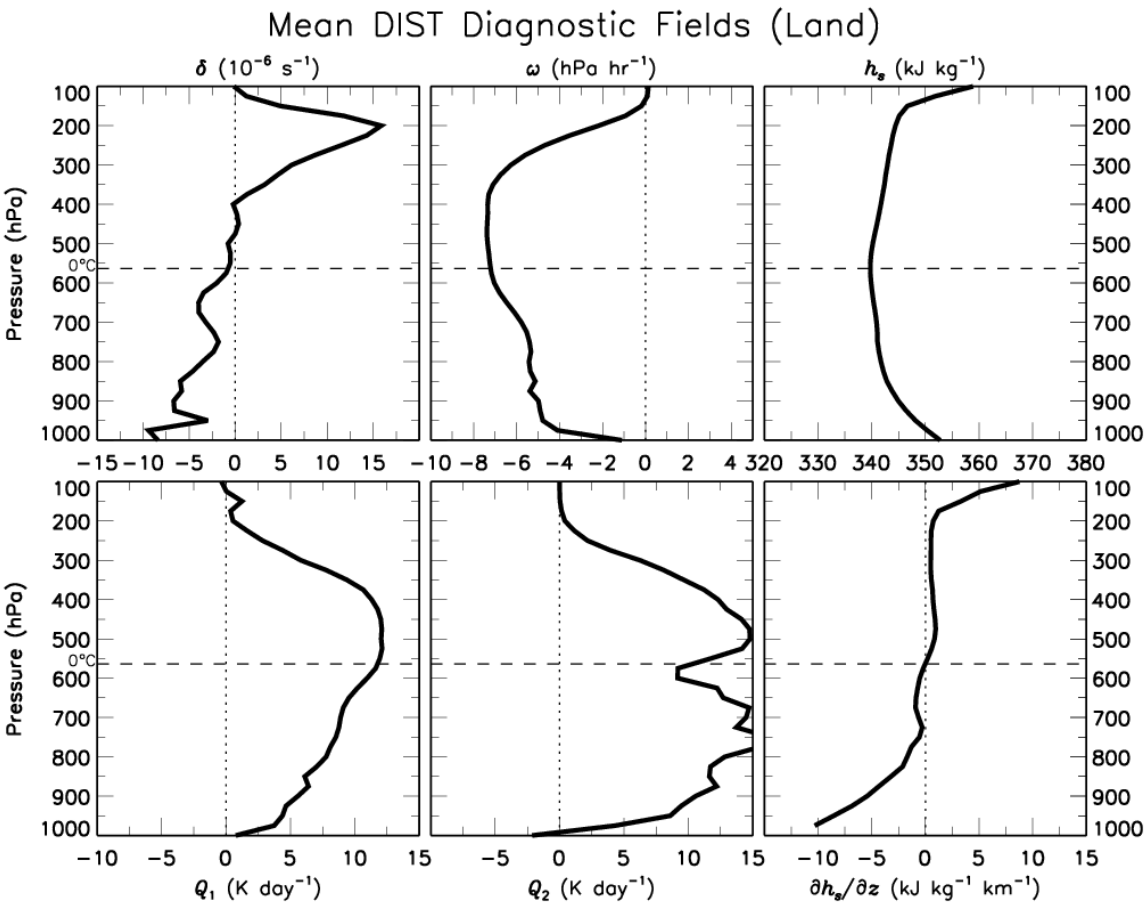

Fig. 4.17. As in Fig. 4.9 except for DIST.

Figure 4.18 provides the diurnal time–pressure plots of the fields displayed in Fig. 4.16 (as in Fig. 4.10), which are all in diurnal-anomaly form except for RH (which is also displayed in diurnal-average form). Consistent with Fig. 4.13, much less of a diurnal cycle in the low-level flow (i.e., related to the LSB/MV circulations) is shown than during UNDIST (Fig. 4.10). Similarly, diurnal variation in low-level T' is weak, though still present. The "elbow" pattern in T' described earlier for UNDIST (Fig. 4.10), which was consistent with a diurnal transition from deep convection to stratiform rain, is also present for DIST (Fig. 4.18). Another interesting feature is the marked diurnal evolution in q': note the maximum in q' up to ~500 hPa at 14LT, which corresponds with

maximum middle-tropospheric RH′ (e.g., from 700~500 hPa). Diurnal evolution in q' was not as pronounced during UNDIST (Fig. 4.10).

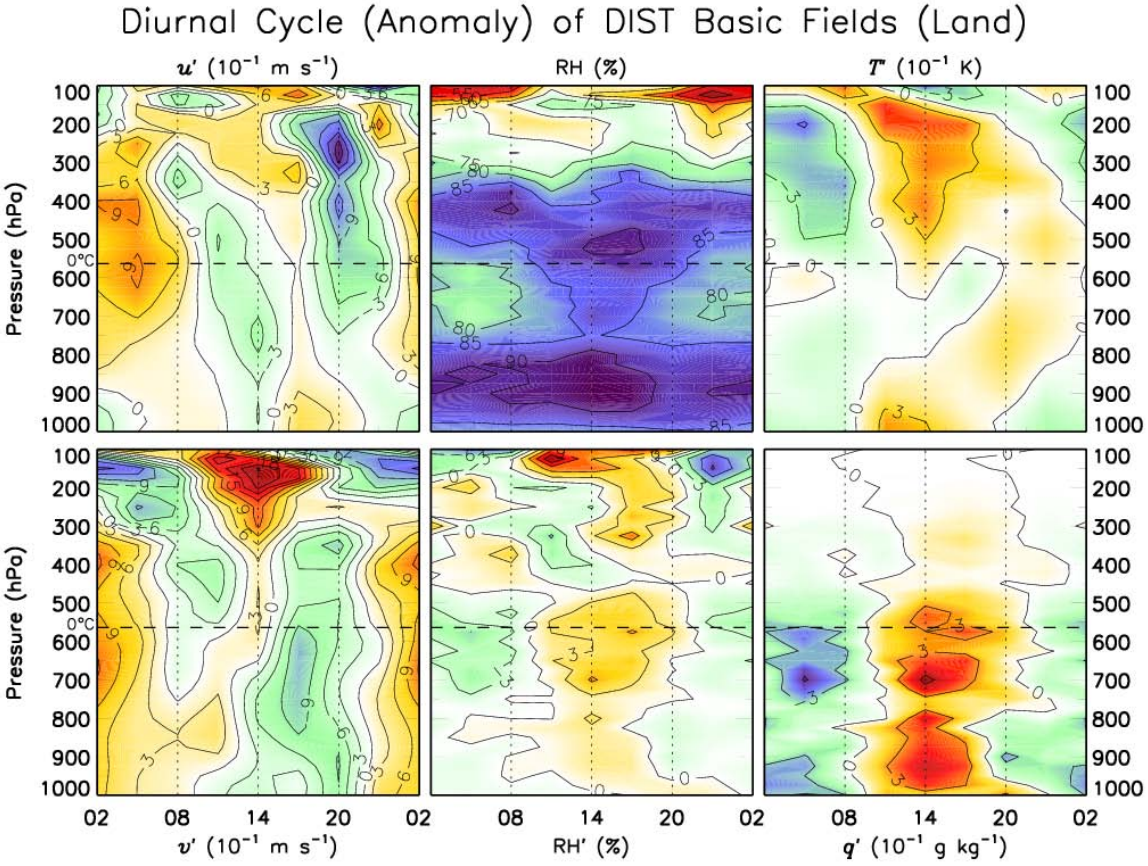

Fig. 4.18. As in Fig. 4.10 except for DIST.

Figure 4.19 provides the diurnal time–pressure plots for the diagnostic quantities displayed in Fig. 4.17 (as in Fig. 4.11). Deep convection maximizes at 14LT, with deep-tropospheric ascent (consistent with the profile of divergence), heating, and drying, which is coincident with maximum convergence of upslope flow in Taiwan (Fig. 4.13). Similar to T', the diurnal cycle in low-level conditional instability is reduced compared to UNDIST (Fig. 4.11). The diurnal evolution of convection, which is better sampled during DIST with 8 day^{-1} soundings than during UNDIST, can be summarized as follows: lower-

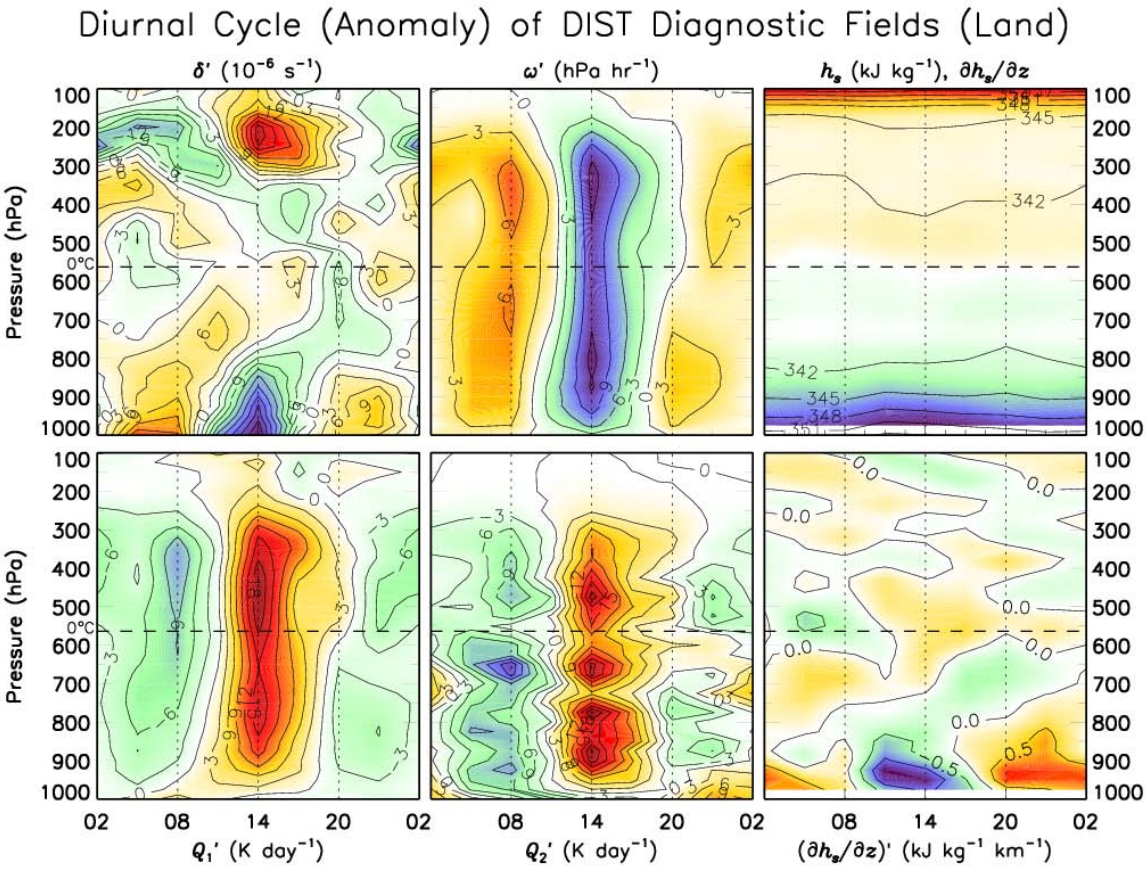

Fig. 4.19. As in Fig. 4.11 except for DIST.

(and upper-) tropospheric positive q' (T') develop in association with shallow convection between 08 and 11LT; rapid transition to deep convection occurs between 11 and 14LT in association with intensification of lower–middle- (upper-) tropospheric positive q' (T'); deep convection transitions into stratiform rainfall between 17 and 20LT (indicated by rising motion, warming, and drying above the freezing level and sinking, cooling, and moistening below it), as positive q' and T' begin to weaken and concentrate in the middle troposphere; sinking motion, cooling, moistening, and $q'<0$ are established throughout the depth of the troposphere by 23LT; sinking motion, cooling, and moistening intensify into the morning hours (02–08LT), exhibiting a tilted structure (most evident in Q_1) of

increasing intensity with time and height (similar to the daytime convective pattern); the pattern repeats shortly after 08LT.

As mentioned earlier, the pronounced relative minimum in apparent drying near the freezing level (Fig. 4.17) has been attributed to stratiform rainfall in past studies (e.g., Johnson et al. 1996), whereby melting and evaporation of falling hydrometeors in areas of stratiform rain reduce net drying at this level. This structure can also be seen quite clearly in the diurnal cycle (Fig. 4.19): note, e.g., the relative minimum in Q_2 at the freezing level around 14LT associated with deep convection, which persists through 20LT as deep convection transitions to stratiform rain and enhanced convergence develops just below the freezing level.

Note the relationship between deep u' and v' (Fig. 4.18) and the pattern of deep convection throughout the day (Fig. 4.19): enhanced southwesterly flow is present through a deep layer during the overnight/early morning hours, while the flows are reduced or negative during the daytime hours. This pattern is likely related to reestablishment of the background southwesterly tropospheric flow (Fig. 4.16) after intense daytime convection has mixed reduced momentum upward.

As stated earlier, the evolution of convection documented here (Figs. 4.18 and 4.19) closely matches with the "self-similar" nature of tropical convection on varying temporal and spatial scales (Kiladis et al. 2009). The enhanced sounding frequency during the EOP has enabled more detailed documentation of features such as the shallow convection around 11LT. It is likely that such features were also present during UNDIST, though that 4 day^{-1} sounding frequency was insufficient to capture them.

5. DISCUSSION

In this study we have described aspects of flow variability during the TiMREX field campaign, which sampled the environment in the Taiwan vicinity during the 2008 East Asian summer monsoon season. Particular focus has been on description of the diurnal cycle and differences in diurnal variability between a disturbed (DIST) and undisturbed (UNDIST) period during the Taiwan Mei-yu season, which were characterized by intense and suppressed convective activity, respectively.

5.1 Characteristics of the diurnal cycle and relationships with rainfall

Section 4.1 documents the diurnal cycle of the 22–29 May undisturbed period (UNDIST) in the 2008 Taiwan Mei-yu season, which was characterized by prominent diurnal surface flows (Fig. 4.2 and 4.5) in the presence of strong diurnal insolation (Fig. 4.3). Most important for controlling rainfall in Taiwan during UNDIST were the flows associated with the local diurnal LSB/MV circulations, which were associated with pronounced offshore-propagating density currents during the nighttime/morning hours and strong upslope flows in daytime hours (Figs. 4.5, 4.7a–d, and 4.10). These flows drove enhanced offshore rainfall near northwestern Taiwan in the early morning and heavy rainfall along the western coastal plains and foothills during the afternoon (Figs. 4.5, 4.7a–d, 4.10, and 4.11). Though much weaker, diurnal surface flows were still evident during the 1–6 June disturbed period (DIST; Section 4.2; Figs. 4.2 and 4.13), with LSB/MV induced upslope flows maximizing at 14LT (as in UNDIST). Furthermore,

the observed diurnal cycle in rainfall intensity/coverage (maximizing at 17LT) was more pronounced during DIST (Fig. 4.13). This suggests that the sensitivity of rainfall to forcing such as the local diurnal LSB/MV circulations might have been higher during DIST.

Though some deep convection existed in the afternoons during UNDIST, the prominence of shallow vertical circulations and bottom-heavy moist convection in the Taiwan vicinity was evident (Figs. 4.7a–d and 4.11). Observations indicate that large-scale forcing was absent or weak during UNDIST (Figs. 3.3, 3.5, and 3.6), and free-tropospheric humidity was low (Figs. 3.3 and 4.8). During DIST, in contrast, the troposphere was very moist and Taiwan was situated slightly east of a 200-hPa trough associated with stronger deep-tropospheric flow (compared to UNDIST; Figs. 3.3, 3.8, and 4.16). The deep-layer (850–200-hPa) shear magnitude during DIST was 15 m s^{-1} – three times that of UNDIST – which might suggest a more favorable environment for convective organization (e.g., increased MCS activity). Also important was the presence of a Mei-yu frontal boundary situated across the northern SCS and southern Taiwan, which was characterized by enhanced low-level cyclonic shear and convergence (Figs. 3.7 and 4.12) and associated with intense eastward-propagating MCSs (Lai et al. 2011; Davis and Lee 2012). The above characterizing features of DIST, which were tied to deeper and more vigorous convection (Figs. 4.17 and 4.19), might explain the increased sensitivity of daily rainfall to forcing by the diurnal cycle.

The diurnal cycle reported in Chapter 4 is consistent with that reported for the same region by Johnson and Bresch (1991). In particular, there is an observed afternoon/evening transition from deep convection to stratiform rain (most apparent

during DIST, when higher frequency data are available). The outflows from these systems could serve to amplify the nighttime surface density currents associated with the LSB/MV circulations (Figs. 4.7a–d and 4.11; Johnson and Bresch 1991). The diurnal cycle documented here is also similar to that of other parts of the world, including the North American monsoon region (Johnson et al. 2007, 2010), where LSB/MV circulations control the timing, intensity, and location of rainfall in the mountainous coastal regions of Mexico and the Gulf of California. Similar to the Taiwan region, offshore-propagating density currents are responsible for enhancing offshore nighttime rainfall in the Gulf region (Johnson et al. 2010). Further, this region exhibits a similar transition from deep convection to stratiform rainfall through the course of the diurnal cycle (Johnson et al. 2010). These consistencies demonstrate the general importance of local thermodynamic circulations on diurnal rainfall variability, particularly in mountainous tropical and subtropical regions where diurnal insolation is strong and synoptic forcing is weak. Further, the observed transitions from deep convection to stratiform-type rainfall with the progression of the diurnal cycle in these different regions reflects the generality of rainfall characteristics, or the “self-similar” nature of convection across spatial and temporal scales (Kiladis et al. 2009).

An interesting feature observed during UNDIST was the area of rainfall downstream of Taiwan that initiated around 20LT in the presence of convergence between nighttime offshore flow in eastern Taiwan and enhanced easterly flow farther offshore (Figs. 4.5 and 4.7d). Neither the enhanced offshore easterly flow (which was associated with a northerly barrier jet near southeastern Taiwan) nor the subsequently eastward-propagating rainfall feature is well understood, and it is thus far unclear if it is a

commonly observed phenomenon. Upon further analysis of this feature, comparisons with a diurnal offshore-propagating area of rainfall from southern China should be conducted (Aves and Johnson 2008).

5.2 Impacts of topography

In the mean (Figs. 4.4 and 4.6), rainfall during UNDIST was maximized over the coastal plains and lower foothills of western Taiwan as opposed to the high peaks of the CMR (similar to the findings of Johnson and Bresch 1991), though there are also features just offshore from northwestern Taiwan and along the lee slopes in northeastern Taiwan. These rainfall characteristics are tied to the interaction of low-Fr southwesterly flow (Fr~0.3) with the complex topography of Taiwan, which includes the impacts of the rainfall itself, such as evaporatively generated downdrafts and convectively enhanced circulations (Figs. 4.7a–d and 4.11; Chen and Lin 2005). One concept alluded to by Johnson and Bresch (1991), though not investigated herein, is the diurnal cycle in characteristic Fr. For instance, Johnson and Bresch (1991) note that, with daytime surface heating and low-level condensation, Fr can increase as a result of local destabilization (reduction of N). Further, the LSB/MV flows can drive a locally stronger characteristic U (e.g., in western Taiwan during the afternoon; Fig. 4.5), which is also associated with an increase in Fr. Higher Fr represents a more *flow-over* as opposed to *flow-around* regime (e.g., Smolarkiewicz et al. 1988), so this might explain some component of the diurnal changes in rainfall in Fig. 4.5. This would be an interesting concept to investigate in more detail with a modeling study.

During DIST, mean rainfall was maximized over the high peaks of the CMR (Fig. 4.12), in stark contrast to UNDIST (Fig. 4.4). This could be understood by considering the nature of rainfall during this period, which came mainly in the form of large MCSs (Lai et al. 2011; Davis and Lee 2012). The environment is generally moist-neutral within MCSs, suggesting that air is more freely perturbed by topography (Houze 2011). This suggests that there should be a positive correlation between topographic height and rainfall during DIST, which is indeed demonstrated in Fig. 4.12 (compare with topographic map; Fig. 1.2). Furthermore, stronger tropospheric flows during DIST (Figs. 3.3 and 4.16) also resulted in slightly larger Fr (~0.5).

The deadliest typhoon to hit Taiwan in history, Typhoon Morakot (2009), caused >3000 mm of rainfall in the high peaks of southern Taiwan (Wu et al. 2011). Though many factors went into causing the extreme rainfall values associated with Morakot (such as greatly reduced translation speed upon making landfall), similar correlation between terrain height and rainfall was observed (Wu et al. 2011). It is likely that this was (at least in part) related to the nature of forcing by the terrain, which was to lift parcels vertically in a moist-neutral environment instead of causing the flow to split around the terrain, as would occur in a more stable environment (e.g., Fig. 4.4).

6. SUMMARY AND CONCLUSIONS

In this study we compare the diurnal cycle during an undisturbed period (UNDIST) with that of a disturbed period (DIST) during the Mei-yu season in Taiwan and the surrounding area using data from the May-June 2008 Terrain-influenced Monsoon Rainfall Experiment (TiMREX). TiMREX offers a valuable opportunity to study the complex interactions between orographically modified flows and convection during the East Asian summer monsoon season in this part of the world.

A unique method has been employed for analyzing the special TiMREX datasets that involves 3DVAR DA techniques. Benefits of this approach include gap filling by model (background) data where observations are sparse and balance constraints in the resulting analysis fields. Further, grid spacing is not sacrificed in the reanalysis generated here (REANAL), which is in contrast to the global reanalysis datasets that are more subject to computational limitations (e.g., Kalnay et al. 1996). Though some issues were found (e.g., in the moisture fields), REANAL demonstrates physically coherent relationships between convection (i.e., the apparent heat source Q_1 and the apparent moisture sink Q_2) and the three-dimensional flow fields, which agree well with observations of rainfall (e.g., Figs. 3.2–3.4).

The period during which enhanced observations were collected in TiMREX (the SOP) spanned 15 May–26 June 2008. The TiMREX SOP exhibited marked fluctuations in rainfall activity, which were associated with fluctuations in free-tropospheric RH, middle- and upper-tropospheric flows, and convective activity (Figs. 3.2–2.4). Northerly cold intrusions in the form of a shallow Mei-yu front were also important (during the first

active period, ACTIVE1) in focusing heavy rainfall along a roughly west–east oriented line across the northern SCS and southern Taiwan. Following onset of monsoon southwesterly flow at the surface (22 May), which was not met with enhanced convective activity around Taiwan, convection, low-level instability, and tropospheric RH exhibited relationships characteristic of propagating tropical convective modes (Figs. 3.3 and 3.4; Kiladis et al. 2009). In particular, shallow/gradual moistening preceded vigorous deep convection, deep moisture was established throughout the troposphere in concert with deep convection, and lower-tropospheric drying followed with the transition to a downdraft-dominated troposphere (Figs. 3.3 and 3.4).

The diurnal cycle was strong during a characteristic undisturbed period (22–29 May: UNDIST; Fig. 4.2), which was consistent with strong diurnal insolation under reduced cloudiness (Fig. 4.3) and weak large-scale forcing (Figs. 3.3 and 3.6). Enhanced land–sea breeze (LSB) and mountain–valley (MV) circulations exhibited strong control over the patterns and intensity of rainfall, which was otherwise controlled by interaction of low-Fr southwesterly monsoon flow with mountainous topography (Fig. 4.4). Though some deep convection was present over Taiwan (at 14LT) during this period, there was a prominence of shallow circulations associated with bottom-heavy convective profiles (Figs. 4.7a–d, 4.10, and 4.11).

During a later active period (1–6 June: DIST), a Mei-yu front characterized by enhanced cyclonic shear and convergence and increased MCS activity was situated across the northern SCS and southern Taiwan, resulting in heavy rainfall there (Fig. 4.12). Though diurnal surface flows were weaker during DIST in association with increased cloudiness and rainfall (Figs. 4.2, 4.3, and 4.13), significant diurnal rainfall

variability was observed (Figs. 4.13 and 4.19). Daytime convection exhibited a deeper and more vigorous profile (Figs. 4.17 and 4.19), which is consistent with large-scale forcing for ascent (Fig. 3.8), a moist troposphere, and enhanced surface triggering associated with the Mei-yu front.

During both the disturbed and undisturbed periods, rainfall exhibited a similar diurnal evolution characterized by a transition from deep convection to stratiform rain (Figs. 4.11 and 4.19), which is consistent with the diurnal cycle documented in other parts of the world (e.g., Johnson et al. 2010). That a similar evolution was observed during the broader evolution of the active period (Fig. 3.4) reflects the "self-similar" character of rainfall systems across spatial and temporal scales in the tropics (Kiladis et al. 2009).

The principal results of this study are as follows:

- The application of 3DVAR data assimilation techniques to TiMREX sounding data has yielded a detailed analysis field from which a range of diagnostic studies and modeling validation efforts can be carried out.
- The diurnal cycle of local circulations and heating and moistening of the atmosphere over Taiwan and its vicinity have been documented on spatial and temporal scales heretofore not possible as a result of the special TiMREX sounding and surface network.
- Although the amplitude of land–sea and mountain–valley breezes is reduced during highly disturbed periods, several environmental factors (including deep abundant moisture, a low-level triggering mechanism, and an upper-level pattern

that is more conducive for large-scale ascent and convective organization) can make the environment particularly sensitive to diurnally driven local circulations such that the diurnal variability in rainfall during those periods is large.

- Moist conditions and stronger southwesterly flow during the disturbed period of the Mei-yu season led to a shifting of heaviest precipitation from lower to higher elevations along the slopes of Taiwan's Central Mountain Range.

Though the present study has shed light on the governing factors that control the character of mean and diurnal rainfall in Taiwan during the Mei-yu season (e.g., tropospheric humidity, large-scale forcing, and surface triggering mechanisms), further study is necessary to determine exactly which (if not all) of these factors are most important. Future modeling studies might clarify such questions, as well as further our understanding of how exactly these controlling factors govern rainfall characteristics such as convective vigor, the nature of orographic rain enhancement, and the sensitivity of rainfall to diurnal flows.

BIBLIOGRAPHY

Asencio N., and Stein J., 2006: Origins of the reverse flow over the windward Alpine foothills of the MAP IOP 3 and IOP 8. *Quart. J. Roy. Meteor. Soc.*, **132**, 297–316.

Aves, S. L., and R. H. Johnson, 2008: The diurnal cycle of convection over the northern South China Sea during the South China Sea Monsoon Experiment. *J. Meteor. Soc. Japan*, **86**, 919-934.

Bao, X., F. Zhang, and J. Sun, 2011: Diurnal variations of warm-season precipitation east of the Tibetan Plateau over China. *Mon. Wea. Rev.*, **139**, 2790–2810.

Barker, D. M., W. Huang, Y-R. Guo, A. J. Bourgeois, and Q. N. Xiao, 2004: A three-dimensional variational data assimilation system for MM5: Implementation and initial results. *Mon. Wea. Rev.*, **132**, 897–914.

Carbone, R. E., W. A. Cooper, and W.-C. Lee, 1995: Forcing of flow reversal along the windward slopes of Hawaii. *Mon. Wea. Rev.*, **123**, 3466–3480.

Chan, J. C. L., W. Ai, and J. Xu, 2002: Mechanisms responsible for the maintenance of the 1998 South China Sea summer monsoon. *J. Meteor. Soc. Japan*, **80,** 1103–1113.

Chen, G. T.-J., 2004: Research on the phenomena of Meiyu during the past quarter century: An overview. *East Asian Monsoon*, C. P. Chang, Ed., Series for Meteorology of East Asia, Vol. 2, World Scientific, 357–403.

——, C.-C. Wang, and S.-W. Chang, 2008: A diagnostic case study of Mei-yu frontogenesis and development of wavelike frontal disturbances in the subtropical environment. *Mon. Wea. Rev.*, **136**, 41–61.

Chen, G., and C.-H. Sui, 2010: Characteristics and origin of quasi-biweekly oscillation over the western North Pacific during boreal summer, *J. Geophys. Res.*, **115**, D14113.

Chen, G., W. Sha, and T. Iwasaki, 2009: Diurnal variation of precipitation over southeastern China: Spatial distribution and its seasonality, *J. Geophys. Res.*, **114**, D13103.

Chen, S.-H., and Y.-L. Lin, 2005: Effects of moist Froude number and CAPE on a conditionally unstable flow over a mesoscale mountain ridge. *J. Atmos. Sci.*, **62**, 331–350.

Chen, T.-C., and J.-M. Chen, 1995: An observational study of the South China Sea monsoon during the 1979 summer: Onset and life cycle. *Mon. Wea. Rev.*, **123**, 2295–2318.

Chen, Y.-L., 1993: Some synoptic-scale aspects of the surface fronts over southern China during TAMEX. *Mon. Wea. Rev.*, **121**, 50–64.

——, and J. Li, 1995: Characteristics of surface airflow and pressure patterns over the island of Taiwan during TAMEX. *Mon. Wea. Rev.*, **123**, 695–716.

——, and J. Feng, 2001: Numerical simulations of airflow and cloud distributions over the windward side of the island of Hawaii. Part I: The effects of trade wind inversion. *Mon. Wea. Rev.*, **129**, 1117–1134.

Ciesielski, P. E., and R. H. Johnson, 2008: Diurnal cycle of surface flows during 2004 NAME and comparison to model reanalysis. *J. Climate*, **21**, 3890-3913.

——, ——, P. T. Haertel, and J. Wang, 2003: Corrected TOGA COARE sounding humidity data: Impact on diagnosed properties of convection and climate over the warm pool. *J. Climate*, **16**, 2370-2384.

——, W.-M. Chang, S.-C. Huang, R. H. Johnson, B. Jong-Dao Jou, W.-C. Lee, P.-H. Lin, C.-H. Liu, and J. Wang, 2010: Quality controlled upper-air sounding dataset for TiMREX/SoWMEX: Development and corrections. *J. Atmos. Ocean. Tech.*, **27**, 1802-1821.

Dai, A., 2001: Global precipitation and thunderstorm frequencies. Part II: Diurnal variations. *J. Climate*, **14**, 1112–1128.

——, and C. Deser, 1999: Diurnal and semidiurnal variations in global surface wind and divergence fields. *J. Geophys. Res.* **104**, 31109–31125.

Davis, C. A., and W.-C. Lee, 2012: Mesoscale analysis of heavy rainfall episodes from SoWMEX/TiMREX. *J. Atmos. Sci.*, **69**, 521–537.

Derber, J. C., D. F. Parrish, and S. J. Lord, 1991: The new global operational analysis system at the National Meteorological Center. *Wea. Forecasting*, **6**, 538–547.

Ding, Y. H., and C. L. Chan, 2005: The East Asian summer monsoon: An overview. *Meteor. Atmos. Phys.*, **89**, 117–142.

Dirren, S., R. D. Torn, and G. J. Hakim, 2007: A data assimilation case study using a limited-area ensemble Kalman filter. *Mon. Wea. Rev.*, **135**, 1455–1473.

Epifanio, C. C., and R. Rotunno, 2005: The dynamics of orographic wake formation in flows with upstream blocking. *J. Atmos. Sci.*, **62**, 3127–3150.

Gille, S. T., S. G. L. Smith, and S. M. Lee, 2003: Measuring the sea breeze from QuikSCAT scatterometry, *Geophys. Res. Lett.*, **30**, 1114.

Gray, W. M., and R. W. Jacobson, 1977: Diurnal variation of deep cumulus convection. *Mon. Wea. Rev.*, **105**, 1171–1188.

He, H., J. W. McGinnis, Z. Song, and M. Yanai, 1987: Onset of the Asian summer monsoon in 1979 and the effect of the Tibetan Plateau. *Mon. Wea. Rev.*, **115**, 1966–1995.

——, 2012: Orographic effects on precipitating clouds, *Rev. Geophys.*, **50**, RG1001.

Huang, W. R., J. C. L. Chan, and S.-Y. Wang, 2010: A planetary-scale land-sea breeze circulation in East Asia and the western North Pacific. *Quart. J. Roy. Meteor. Soc.*, **136**, 1543–1553.

Huang, X.-Y., and Coauthors, 2009: Four-dimensional variational data assimilation for WRF: Formulation and preliminary results. *Mon. Wea. Rev.*, **137**, 299–314.

Huffman, G. J., and Coauthors, 2007: The TRMM multisatellite precipitation analysis (TMPA): Quasi-global, multiyear, combined-sensor precipitation estimates at fine scales. *J. Hydrometeor.*, **8,** 38–55.

Hung, C.-w., and H.-H. Hsu, 2008: The first transition of the Asian summer monsoon, intraseasonal oscillation, and Taiwan Mei-yu. *J. Climate*, **21**, 1552–1568.

Ide, K., P. Courtier, M. Ghil, and A. C. Lorenc, 1997: Unified notation for data assimilation: Operational, sequential and variational. *J. Meteor. Soc. Japan*, **75,** 181–189.

Johnson, R. H., 1992: Heat and moisture sources and sinks of Asian monsoon precipitating systems. *J. Meteor. Soc. Japan*, **70**, 353-372.

——, 2011: Diurnal cycle of monsoon convection. *The Global Monsoon System: Research and Forecasts, 2nd Edition*, C.-P. Chang, et al. Eds., World Scientific, 257-276.

——, and J. F. Bresch, 1991: Diagnosed characteristics of *Mei-Yu* precipitation systems over Taiwan during the May-June 1987 TAMEX. *Mon. Wea. Rev.*, **119**, 2540-2557.

——, and P. E. Ciesielski, 2000: Rainfall and radiative heating rate estimates from TOGA-COARE atmospheric budgets. *J. Atmos. Sci.*, **57**, 1497-1514.

——, and ——, 2002: Characteristics of the 1998 summer monsoon onset over the northern South China Sea. *J. Meteor. Soc. of Japan*, **80**, 561-578.

——, ——, and K. A. Hart, 1996: Tropical inversions near the 0°C level. *J. Atmos. Sci.*, **53**, 1838-1855.

——, T. M. Rickenbach, S. A. Rutledge, P. E. Ciesielski, and W. H. Schubert, 1999: Trimodal characteristics of tropical convection, *J. Climate*, **12**, 2397-2418.

——, S. A. Aves, P. E. Ciesielski, and T. D. Keenan, 2005: Organization of oceanic convection during the onset of the 1998 East Asian Summer monsoon. *Mon. Wea. Rev.*, **133**, 131-148.

——, P. E. Ciesielski, B. D. McNoldy, P. J. Rogers, and R. K. Taft, 2007: Multiscale variability of the flow during the North American Monsoon Experiment. *J. Climate*, **20**, 1628-1648.

——, ——, T. S. L'Ecuyer, and A. J. Newman, 2010: Diurnal cycle of convection during the 2004 North American Monsoon Experiment. *J. Climate*, **23**, 1060-1078.

Jou, B. J.-D., W.-C. Lee, and R. H. Johnson: An overview of SoWMEX/TiMREX. *The Global Monsoon System: Research and Forecasts, 2nd Edition*, C.-P. Chang, et al. Eds., World Scientific, 303-318.

Kalnay, E., and Coauthors, 1996: The NCEP/NCAR 40-Year Reanalysis Project. *Bull. Amer. Meteor. Soc.*, **77**, 437–471.

Kerns, J. B. W., Y.-L. Chen, and M.-Y. Chang, 2010: The diurnal cycle of winds, rain, and clouds over Taiwan during the Mei-Yu, summer, and autumn rainfall regimes. *Mon. Wea. Rev.*, **138**, 497–516.

Kiladis, G. N., M. C. Wheeler, P. T. Haertel, K. H. Straub, and P. E. Roundy, 2009: Convectively coupled equatorial waves. *Rev. Geophys*., **47**, RG2003.

Kishtawal, C. M., and T. N. Krishnamurti, 2001: Diurnal variation of summer rainfall over Taiwan and its detection using TRMM Observations. *J. Appl. Meteor.*, **40**, 331–344.

Kleist, D. T., D. F. Parrish, J. C. Derber, R. Treadon, W.-S. Wu, and S. Lord, 2009: Introduction of the GSI into the NCEP global data assimilation system. *Wea. Forecasting*, **24**, 1691–1705.

Krishnamurti, T. N., and P. Ardanuy, 1980: The 10–20-day westward propagating mode and breaks in the monsoons. *Tellus*, **32,** 15–26.

——, and C. M. Kishtawal, 2000: A pronounced continental-scale diurnal mode of the Asian summer monsoon. *Mon. Wea. Rev.*, **128**, 462–473.

Kummerow, C., and Coauthors, 2000: The status of the Tropical Rainfall Measuring Mission (TRMM) after two years in orbit. *J. Appl. Meteor.*, **39,** 1965–1982.

Lai, H.-W., C. A. Davis, and B. Jong-Dao Jou, 2011: A subtropical oceanic mesoscale convective vortex observed during SoWMEX/TiMREX. *Mon. Wea. Rev.*, **139**, 2367–2385.

Lau, K-M., G. J. Yang, and S. H. Shen, 1988: Seasonal and intraseasonal climatology of summer monsoon rainfall over East Asia. *Mon. Wea. Rev.,* **116**, 18–37.

Li, J., and Y.-L. Chen, 1998: Barrier jets during TAMEX. *Mon. Wea. Rev.*, **126**, 959–971.

Loehrer, S. M., T. A. Edmands, and J. A. Moore, 1996: TOGA COARE upper-air sounding data archive: Development and quality control procedures. *Bull. Amer. Meteor. Soc.*, **77**, 2651– 2671.

Madden, R. A., and P. R. Julian, 1971: Detection of a 40–50 day oscillation in the zonal wind in the tropical Pacific. *J. Atmos. Sci.*, **28**, 702–708.

Majumdar, S. J., K. J. Sellwood, D. Hodyss, Z. Toth, and Y. Song, 2010: Characteristics of target areas selected by the ensemble transform Kalman filter for medium-range forecasts of high-impact winter weather. *Mon. Wea. Rev.*, **138**, 2803–2824.

Mao, J., and J. C. L. Chan, 2005: Intraseasonal variability of the South China Sea summer monsoon. *J. Climate*, **18**, 2388–2402.

Mapes, B. E., and R. A. Houze, 1993: Cloud clusters and superclusters over the oceanic warm pool. *Mon. Wea. Rev.*, **121**, 1398–1416.

——, and ——, 1995: Diabatic divergence profiles in western Pacific mesoscale convective systems. *J. Atmos. Sci.,* **52,** 1807–1828.

Meng, Z., and F. Zhang, 2008: Tests of an ensemble Kalman filter for mesoscale and regional-scale data assimilation. Part IV: Comparison with 3DVAR in a month-long experiment. *Mon. Wea. Rev.*, **136**, 3671–3682.

Mesinger, F., and Coauthors, 2006: North American regional reanalysis. *Bull. Amer. Meteor. Soc.*, **87**, 343–360.

Miglietta, M. Marcello, and R. Rotunno, 2009: Numerical simulations of conditionally unstable flows over a mountain ridge. *J. Atmos. Sci.*, **66**, 1865–1885.

Miguez-Macho, G., and J. Paegle, 2000: Sensitivity of a global forecast model to initializations with reanalysis datasets. *Mon. Wea. Rev.*, **128**, 3879–3889.

Mo, K. C., M. Chelliah, M. L. Carrera, R. W. Higgins, and W. Ebisuzaki, 2005: Atmospheric moisture transport over the United States and Mexico as evaluated in the NCEP Regional Reanalysis. *J. Hydrometeor*, **6**, 710–728.

——, E. Rogers, W. Ebisuzaki, R. W. Higgins, J. Woollen, and M. L. Carrera, 2007: Influence of the North American Monsoon Experiment (NAME) 2004 enhanced soundings on NCEP operational analyses. *J. Climate*, **20**, 1821–1842.

Nesbitt, S. W., and E. J. Zipser, 2003: The diurnal cycle of rainfall and convective intensity according to three years of TRMM measurements. *J. Climate*, **16**, 1456–1475.

Nuss, W. A., and D. W. Titley, 1994: Use of multiquadric interpolation for meteorological objective analysis. *Mon. Wea. Rev.*, **122**, 1611–1631.

O'Brien, J. J., 1970: Alternative solutions to the classical vertical velocity problem. *J. Appl. Meteor.*, **9**, 197–203.

Oort, A. H., and T. H. Vonder Haar, 1976: On the observed annual cycle in the ocean-atmosphere heat balance over the northern hemisphere. *J. Phys. Oceanogr.*, **6**, 781–800.

Orville, H. D., 1964: On mountain upslope winds. *J. Atmos. Sci.*, **21**, 622–633.

Overland, J. E., and N. A. Bond, 1995: Observations and scale analysis of coastal wind jets. *Mon. Wea. Rev.*, **123**, 2934–2941.

Parrish, D. F., and J. C. Derber, 1992: The National Meteorological Center's spectral statistical interpolation analysis system. *Mon. Wea. Rev.*, **120,** 1747–1763.

Pierrehumbert, R. T., and B. Wyman, 1985: Upstream effects of mesoscale mountains. *J. Atmos. Sci.*, **42**, 977–1003.

Rabier F., H. Järvinen, E. Klinker, J.-F. Mahfouf, and A. Simmons, 2000: The ECMWF operational implementation of four-dimensional variational assimilation. I: Experimental results with simplified physics. *Quart. J. Roy. Meteor. Soc.*, **126**, 1143–1170.

Rodwell, M. J. and Hoskins, B. J., 1996: Monsoons and the dynamics of deserts. *Quart. J. Roy. Meteor. Soc.*, **122**, 1385–1404.

Rotunno, R., 1983: On the linear theory of the land and sea breeze. *J. Atmos. Sci.*, **40**, 1999–2009.

Smolarkiewicz, P. K., R. M. Rasmussen, and T. L. Clark, 1988: On the dynamics of Hawaiian cloud bands: Island forcing. *J. Atmos. Sci.*, **45**, 1872–1905.

Stephens, G. L., and Coauthors, 2002: The CloudSat mission and the A-Train. *Bull. Amer. Meteor. Soc.*, **83**, 1771–1790.

Thompson, R. M., Jr., S. W. Payne, E. E. Recker, and R. J. Reed, 1979: Structure and properties of synoptic-scale wave disturbances in the intertropical convergence zone of the eastern Atlantic. *J. Atmos. Sci.*, **36,** 53–72.

Tong H. W., J. C. L. Chan, and W. Zhou., 2009: The role of MJO and mid-latitude fronts in the South China Sea summer monsoon onset. *Climate Dynamics* **33**, 827–841.

Torn, R. D., 2010: Performance of a mesoscale ensemble Kalman filter (EnKF) during the NOAA High-Resolution Hurricane Test. *Mon. Wea. Rev.*, **138**, 4375–4392.

——, and G. J. Hakim, 2009: Ensemble data assimilation applied to RAINEX observations of Hurricane Katrina (2005). *Mon. Wea. Rev.*, **137**, 2817–2829.

Trenberth, K. E., D. P. Stepaniak, and J. M. Caron, 2000: The global monsoon as seen through the divergent atmospheric circulation. *J. Climate*, **13**, 3969–3993.

——, and J. M. Caron, 2001: Estimates of meridional atmosphere and ocean heat transports. *J. Climate*, **14**, 3433–3443.

Trier, S. B., D. B. Parsons, and T. J. Matejka, 1990: Observations of a subtropical cold front in a region of complex terrain. *Mon. Wea. Rev.*, **118**, 2449–2470.

Uppala, S. M., and Coauthors, 2005: The ERA-40 reanalysis. *Quart. J. Roy. Meteor. Soc.*, **131,** 2961–3012.

Wallace, J. M., 1975: Diurnal variations in precipitation and thunderstorm frequency over the conterminous United States. *Mon. Wea. Rev.*, **103**, 406–419.

Wang, B., and X. Xu, 1997: Northern hemisphere summer monsoon singularities and climatological intraseasonal oscillation. *J. Climate*, **10**, 1071–1085.

——, and Q. Ding, 2008: Global monsoon: Dominant mode of annual variation in the tropics. *Dyn. Atmos. Ocean.*, **44**, 165–183.

Wang, C.-C., G. T.-J. Chen, and R. E. Carbone, 2004: A climatology of warm-season cloud patterns over East Asia based on GMS infrared brightness temperature observations. *Mon. Wea. Rev.*, **132**, 1606–1629.

Wang, J., H. L. Cole, D. J. Carlson, E. R. Miller, K. Beierle, A. Paukkunen, and T. K. Laine, 2002: Corrections of humidity measurement errors from the Vaisala RS80 radiosonde—Application to TOGA COARE data. *J. Atmos. Oceanic Technol.*, **19**, 981–1002.

Wang, X., D. M. Barker, C. Snyder, and T. M. Hamill, 2008a: A hybrid ETKF–3DVAR data assimilation scheme for the WRF model. Part I: Observing system simulation experiment. *Mon. Wea. Rev.*, **136**, 5116–5131.

——, ——, ——, and ——, 2008b: A hybrid ETKF–3DVAR data assimilation scheme for the WRF model. Part II: Real observation experiments. *Mon. Wea. Rev.*, **136**, 5132–5147.

Webster, P. J., and J. R. Holton, 1982: Cross-equatorial response to middle-latitude forcing in a zonally varying basic state. *J. Atmos. Sci.*, **39**, 722–733.

Whitaker, J. S., G. P. Compo, and J.-N. Thépaut, 2009: A comparison of variational and ensemble-based data assimilation systems for reanalysis of sparse observations. *Mon. Wea. Rev.*, **137**, 1991–1999.

Wu, L., J. Liang, and C.-C. Wu, 2011: Monsoon influence on Typhoon Morakot (2009). Part I: Observational analysis. *J. Atmos. Sci.*, **68**, 2208–2221.

Yanai, M., S. Esbensen, and J. H. Chu, 1973: Determination of bulk properties of tropical cloud clusters from large-scale heat and moisture budgets. *J. Atmos. Sci.*, **30**, 611–627.

——, C. Li, and Z. Song, 1992: Seasonal heating of the Tibetan Plateau and its effects on the evolution of the Asian summer monsoon. *J. Meteor. Soc. Japan*, 70, 319–351.

Yeh, H.-C., and Y.-L. Chen, 2002: The role of offshore convergence on coastal rainfall during TAMEX IOP 3. *Mon. Wea. Rev.*, **130**, 2709–2730.

——, and ——, 2003: Numerical simulations of the barrier jet over northwestern Taiwan during the Mei-Yu season. *Mon. Wea. Rev.*, **131**, 1396–1407.

Yu, R., T. Zhou, A. Xiong, Y. Zhu, and J. Li., 2007: Diurnal variations of summer precipitation over contiguous China. *Geophysical Research Letters*, **34**, L01704.

Zhang, F., M. Zhang, and J. A. Hansen, 2009: Coupling ensemble Kalman filter with four-dimensional variational data assimilation. *Adv. Atmos. Sci.*, **26**, 1–8.

Zhang, M., F. Zhang, X.-Y. Huang, and X. Zhang, 2011: Intercomparison of an ensemble Kalman filter with three- and four-dimensional variational data assimilation methods in a limited-area model over the month of June 2003. *Mon. Wea. Rev.*, **139**, 566–572.

LIST OF ACRONYMS

1020-MM – westward-propagating 10–20-day monsoon mode

3060-MM – northward-propagating 30–60-day monsoon mode

3DVAR – three-dimensional variational DA

4DVAR – four-dimensional variational DA

ACARS – Aircraft Communication Addressing and Reporting System

ACTIVE1 – convectively active period around Taiwan from 1–6 June 2008 during TiMREX

ACTIVE2 – as in ACTIVE1 except from 13–17 June 2008

AMDAR – Aircraft Meteorological Data Reporting

AMMA – African Monsoon Multidisciplinary Analysis (2006)

CISO – climatological intraseasonal oscillation

CMR – Central Mountain Range (Taiwan)

COSMIC – Constellation Observing System for Meteorology Ionosphere and Climate

DA – data assimilation

DIST – convectively active period around Taiwan from 1–6 May 2008 during TiMREX (same time period as ACTIVE1)

EOP – TiMREX Enhanced Observing Period

ESA – TiMREX Enhanced Sounding Array

GFS – Global Forecasting System from NCEP

GPS – Global Positioning System

INTERP – gridded dataset generated by interpolation of observation datasets, which is used for comparison with REANAL

LSB – land–sea breeze

MADIS – Meteorological Assimilation Data Ingest System

MCS – mesoscale convective system

MJO – Madden–Julian oscillation

MV – mountain–valley (or anabatic–katabatic) (circulation)

NCEP – National Centers for Environmental Prediction

PV – potential vorticity

PW – precipitable water

QPESUMS – Quantitative Precipitation Estimation and Segregation Using Multiple Sensors

QuikSCAT – Quick Scatterometer

REANAL – the TiMREX regional reanalysis

SCS – South China Sea

SOP – TiMREX Special Observing Period

SoWMEX – the Southwest Monsoon Experiment (2008)

TAMEX – Taiwan Area Mesoscale Experiment (1987)

TiMREX – the Terrain-influenced Monsoon Rainfall Experiment (2008)

TOGA COARE – Tropical Ocean Global Atmosphere Coupled Ocean–Atmosphere Response Experiment

TRMM – Tropical Rainfall Measuring Mission

UNDIST – convectively inactive period around Taiwan from 22–29 May 2008 during TiMREX

WRFDA – the DA system provided by Weather Research and Forecasting